Dissertation

submitted to the

Combined Faculties of the Natural Sciences and Mathematics

of the Ruperto-Carola-University of Heidelberg, Germany

for the degree of

Doctor of Natural Sciences

Put forward by

Fabienne Cathérine Haupert

born in: Karlsruhe, Germany

Oral examination: February 2, 2012

A Moiré-Deflectometer as Gravimeter for Antihydrogen

Referees: Prof. Dr. Markus K. Oberthaler

Dr. Michael Doser

Zusammenfassung

AE$\overline{\text{g}}$IS (**A**ntimatter **E**xperiment: **G**ravity, **I**nterferometry, **S**pectroscopy) – eines der Experimente am CERN – zielt darauf ab, fundamentale physikalische Eigenschaften von Antimaterie zu untersuchen, um den Wissensstand über die Unvereinbarkeit der Gravitation mit anderen Kräften voranzubringen. Hierfür wird das Experiment in seiner ersten Phase die Gravitationsbeschleunigung von Antiwasserstoff mit einer Präzision von 1% messen, um damit Daten für ein besseres Verständnis von Antimaterie zu liefern. Als Gravimeter für diese Messung wird ein Moiré-Deflektometer benutzt, das in Heidelberg entworfen und gebaut wird. Um dieses Deflektometer auf seine erreichbare Sensitivität hin zu testen und zu charakterisieren, wird eine Atomstrahlquelle metastabiler Argonatome mit einem hohen Fluss und ein Faraday Cup zur Detektion dieser Atome gebaut. Ein zusätzliches optisches Mach-Zehnder Interferometer kontrolliert die Stabilität der Apparatur. Die Hauptkomponenten des Deflektometers, die Beugungsgitter, werden aus sechs Zoll Siliziumgitter hergestellt. Erste Modelle der Gitter und die gesamte Apparatur sind mit der erforderlichen Sorgfalt entworfen und gebaut worden, um die experimentellen Bedingungen des Aufbaus am CERN zu berücksichtigen. Eine erste Gravitationsmessung des Testaufbaus in Heidelberg liefert $g = (9.5 \pm 1.9) \frac{\text{m}}{\text{s}^2}$ und eröffnet eine Vielzahl an möglichen Verbesserungen.

Abstract

AE$\overline{\text{g}}$IS (**A**ntimatter **E**xperiment: **G**ravity, **I**nterferometry, **S**pectroscopy) – one of the experiments carried out at CERN – aims to examine fundamental physical properties of antimatter, in order to promote knowledge about the incompatibility of gravitation with other forces. As part of achieving this knowledge, the experiment will measure in its first phase the gravitational acceleration g of antihydrogen with a precision of 1% and hence, provide data for a deeper understanding of antimatter in general.
A Moiré-deflectometer is applied as gravimeter for this measurement. Its design and construction are carried out in Heidelberg. In order to test and characterise this deflectometer to its best achieveable sensitivity, a high-flux source of metastable argon atoms as well as a Faraday cup to detect these atoms are built. An additional optical Mach-Zehnder interferometer controls the stability of the apparatus. The major components of the deflectometer, the deflection gratings, are manufactured out of six-inch

silicon wafers. Their prototypes together with the entire apparatus are designed and built with due care to account for the experimental conditions given by the apparatus at CERN. A first gravitational measurement with the test setup at Heidelberg yields $g = (9.5 \pm 1.9)\,\frac{\mathrm{m}}{\mathrm{s}^2}$ and opens up a huge number of potential improvements.

Contents

CONTENTS

CONTENTS

Preface and Outline

The first prediction of antimatter was simply a side note in Dirac's 1931 publication titled 'Quantised singularities in the electromagnetic field' [1]. In this publication, Dirac's prior intent was to prove that the existence of magnetic monopoles leads to quantised electric charges. In this context, he reconciled Schrödinger's description of an electron with special relativity, and for the solution of the resulting equation, he needed to assume the existence of a particle with the same mass as the electron and oppositely charged to it. Today, this antiparticle is known as positron. It was observed experimentally for the first time by Carl Anderson in 1933 [2].

The first observation of the antiparticle to the proton, the antiproton, followed in 1955 at the Berkley laboratories [3].[1] Since then, fundamental research on antimatter has continued. At the end of the last century, the first neutral antiatom – the antihydrogen – was produced at relativistic speeds. In 1995, a group a CERN was the first to suceed in this production [5], and in 1998, the Fermilab group published their production of about 100 antihydrogen atoms [6]. It took until 2002 for antihydrogen to be created at low energies. This has been accomplished by two groups working at the CERN antiproton decelerator (AD), namely the ATHENA [7] and shortly afterwards the ATRAP collaboration [8]. Very recently, the first trapped antihydrogen was reported [9]. After ATHENA broke up, some of its former members founded a new collaboration called AE$\overline{\text{g}}$IS (**A**ntimatter **E**xperiment: **G**ravity, **I**nterferometry, **S**ectroscopy) [10].

As its name suggests, AE$\overline{\text{g}}$IS aims for fundamental research on antimatter by gravitational, interferometric and spectroscopic experiments. As its first defined scientific goal, AE$\overline{\text{g}}$IS intends to measure the gravitational acceleration of antihydrogen with a precision of 1%. Hence, it will represent the first direct gravitational measurement of

---

[1]An overview of the research on antiprotons can be found in [4].

antimatter, which gives the project great scientific importance.

However, an appropriate method for the gravitational measurement of antihydrogen needs to be found first. For this purpose, the following paragraph provides an overview of some of today's accelerometers that can measure the absolute or relative gravitation.

By the end of the last century, various methods were known for measuring the gravitational acceleration g. One particular example of such a so-called *gravimeter* works with sensitive spring balances [11]. This device can only measure a relative gravitational acceleration. Another type of gravimeter makes use of pendulums [12, 13]. Today, one of the most common method is based simply on free-falling objects [14, 15, 16, 17]. While pendulum-gravimeters can measure both the relative and absolute gravitation, gravimeters with free-falling objects predominantly determine the absolute value of g. The variety of possible free-falling objects for these gravimeters ranges from single cold atoms [18, 19, 20] to large massive cubes [14, 15, 16, 17].

With regard to the precisions that can be achieved with today's gravimeters, the cold-atom type is particularly interesting. Using atom interferometry, one can even measure absolute gravitation to a precision of $\frac{\triangle g}{g} = 1 \cdot 10^{-10}$ after two days of integration time [18]. Nevertheless, since the setup of these gravimeters typically includes vacuum chambers and fairly complex laser systems for optical trapping of the atoms, they are not convenient for many applications such as, for example geophysical field measurements.

For the AE$\overline{\text{g}}$IS-experiment, none of the described methods for a gravitational measurement is applicable. Either the annihilation process, which occurs when antihydrogen interacts with matter, or other more technical-related difficulties appear. For instance, the implementation of a gravimeter similar to the ones based on atom interferometry is not possible for several reasons. Firstly, the laserlight that is necessary for setting up the *Magneto-Optical-Trap* (MOT) [21] delivers too much energy into the cryogenic environment. Furthermore, the magnetic field configurations preclude the measurement of the time of flight of the particles. Consequently, a different method has to be found.

An appropriate method by using a classical Moiré-deflectometer as gravimeter is based on the experiments of Oberthalter et al. [22]. In these experiments, the functionality of a Moiré-deflectometer as an accelerometer that is sensitive to rotations as well as

to gravitation has been shown with metastable atoms. The setup of Oberthaler et al. requires major adjustments to match the experimental conditions of AE$\overline{g}$IS. In the present thesis, these adjustments are examined and improvements are initiated, yielding an absolute gravitational measurement of argon atoms with a first prototype of such a modified Moiré-deflectometer.

Outline of this Thesis

The present thesis consists of four major parts. The first one (chapter 1) provides the motivation of the project in Heidelberg. For this purpose, we briefly outline some key points to describe how a unification of general relativity with quantum field theory can be connected to a gravitational measurement of antimatter. Subsequently, different antihydrogen production methods are outlined and the one of the AE$\overline{g}$IS-experiment is summarised. Thus, we provide in this first chapter the base for the project of this thesis – a Moiré-deflectometer that is designed and tested for antihydrogen experiments.

The second part (chapter 2) covers the theoretical background of a Moiré-deflectometer. In order to do this, we give an overview of its different application regimes. Here, we distinguish between a device that is based on wave-propagation and wave-interference and one where classical ray optics or Newtonian Mechanics are sufficient as theoretical descriptions. Subsequently, we discuss the most characteristic property of the classical deflectometer: its minimal resolvable acceleraction $g_{\min}$. At this stage, we need to distinguish for the first time between the two setups: the final one at CERN, that examines the gravitation of antihydrogen, and the one in Heidelberg, which measures the gravitation of argon and which we mainly use to test the design. Besides the achievable 1% precision of the setup at CERN, we find a $g_{\min}$ for the argon testing-setup that can resolve even the effect of the tidal force.

The sensitivity analysis of the deflectometer given in the third part (chapter 3) provides critical values for external magnetic and electric fields that substantially disturb the gravitational measurement. For the two examined setups, with argon and with antihydrogen, these critical values are particularly interesting for shielding purposes.

The analysis concludes with an examination of how to solve this shielding issue for the magnetic field by adding a large offset field in a direction that is perpendicular to the one in which gravity is acting. We refer to this method as *bias-reduced-gradient-susceptibility* (BRGS).

For a description of the first prototype of the modified Moiré-deflectometer, we present the experimental construction and the first measurements in the fourth part of this thesis(chapter 4 and chapter 5). To do this, we start with the design of the transmission gratings. This includes the atom's transmission gratings as well as the gratings for the additional optical Mach-Zehnder interferometers, which are necessery to control the stability of the setup. After presenting the details on the realisations of the gratings out of silicon wafers, we further summarise the results of a vibration and stability analysis of a prototype of the setup. Finally, chapter 5 provides a detailed description of the testing setup in Heidelberg. This facilitates a detailed discussion of the results of our first gravitational measurement with argon.

Chapter 1

The AE$\overline{\text{g}}$IS-Experiment at CERN

1.1   Introduction

Since the last century, when physicists have started to look for a unification of the dynamical space-time geometry of general relativity and the fixed background approach of quantum field theory, the concept of *antigravity* $\overline{g}$ has become a controversial issue. Determining the gravitational acceleration of antimatter is regarded as a promising approach for a deeper insight into the theoretical description of gravitation.

This first chapter briefly summarises the background of a potential unification of the two directions in physics – general relativity and quantum field theory – and how this can be connected to gravitational experiments. In addition to this, we provide a particular demonstrative description of the concept of antigravity, the gedanken experiment of Morrison. Both sections strongly motivate the experimental test of gravity with antimatter. For this purpose, it is preferable to produce electrically neutral antimatter. After summarising state-of-the-art production methods for antihydrogen, we give a short introduction into the method of the AE$\overline{\text{g}}$IS-experiment at CERN. This provides the initiation for the Moiré-deflectometer presented in this thesis.

1.2   Theoretical Background for Antigravity

In order to understand the theoretical aspects of a gravitational measurements of antimatter and how this can be connected to the incompatibility of general relativity with electromagnetism, we first consider the apparent differences of these two theories: It is known for general relativity that it has only a single charge (mass m) and its force

general relativity	classical/quantum electromagnetism
force mediated by tensor spin-2 exchange particle charge = mass m always attractive force	force mediated by vector spin-1 exchange particle charge = + or − attractive or repelling force

Table 1.1: Some of the main differences between general relativity and electromagnetism.

(mediated by a tensor particle of spin 2) is always attractive. In contrast to this, electromagnetism has two charges (+ and −) and its force (mediated by a vector field, a spin-1-particle) can yield an attractive force for opposite charges and a repelling force for alike charges. An overview of these differences is given in table 1.1.

What is known about the spin of exchange bosons from nuclear forces, is that the ones with an even integer spin always mediate attractive forces and the ones with an odd integer spin can yield attractive as well as repelling forces [23, 24, 25, 26] depending on whether the interaction occurs between opposite or alike charges, respectively.

For a general description of gravitation, we consider two masses m_1 and m_2 that have gravitational charges[1]. Thus, we remember Newton's law of gravitation, which provides the interaction potential

$$V_{\text{Newton}} = -G\frac{m_1 m_2}{r}, \tag{1.1}$$

where the gravitational constant is denoted by G and the distance between the two charges by r. For an even more general description of gravitation, this potential needs to be modified. Its exchange boson of spin 2, which is also known as the *graviton*[2], might have partners of spin 0 or 1. This possibility is included in the more general potential [23] given by

$$V = -Gm_1 m_2 \frac{1 \mp ae^{-r/v} + be^{-r/s}}{r}, \tag{1.2}$$

where a and b $(a, b \geq 0)$ are the products of the vector and the scalar charges of the two particles, and v and s their respective ranges. Hence, a and b can be considered

---

[1]For the gravitational interaction there are two types of charges: particle and antiparticle.

[2]This elementary particle is introduced as exchange boson for quantum field theory. Its existence has never been proven experimentally and is also not expected to be detectable at all [27].

as the 'coupling strength' relative to G. Note that the sign $\mp$ in front of the vector component denotes the differentiation between the two types of charges. This accounts for the fact that the vector component yields attractive forces for opposite charges and repelling forces for alike ones. Particularly interesting is this potential, as it emphasizes the necessity of measuring interactions between matter and antimatter. To be specific, it reveals that examinations of the matter-matter interaction are sensitive on $|a-b|$. As for matter-antimatter interactions, the sign of a changes, the experiments that measure their interactions are sensitive on $|a+b|$ [10, 23] . Nieto et al. [23] showed that models can be thought of, where not $|a-b| = 0$ but $|a+b|$ does get changed. Hence, a measurement between particles and antiparticles is urgently needed to promote this controversially discussed derivation of Nieto et al..

In contrast to this, a more intelligible approach, which forbids any difference between gravity for matter and the one for antimatter, is the following gedanken experiment of Morrison.

1.3 The Gedanken Experiment of Morrison

As a comprehensible example for the requirement $g \neq \overline{g}$, Morrison et al. [28, 29] depicted a gedanken experiment, to which it is often referred to as *Morrison argument* [23]. Starting with an electron-positron pair e^-e^+ within the earth's gravitational field, we define their starting point by their height x_0. Before letting them annihilate, we move them to a height x_1, with $x_1 > x_0$[1]. Their annihilation process at this height produces two photons that can be deflected by perfect mirrors back to their starting point at x_0. On their way down to x_0, the photons gain energy, as they get blueshifted. Hence, the following pair production of the two meeting photons back at x_0 will produce a pair e^- and e^+ with some kinetic energy. Assuming the validity of the equivalence principle as well as symmetric gravitation, this kinetic energy will match the energy, which has been necessary initially to move the e^-e^+-pair from x_0 to x_1. If there is no symmetric gravitation between e^- and e^+, this energy balance will break down. Thus, in this gedanken experiment, either energy conservation or gravitational

---

[1]In order to keep this experiment as simple as possible, we assume the initial kinetic energies of the two particles to match exactly the energy that is necessary to move them from x_0 up to x_1.

method	process
spontaneous radiative recombination	$\overline{p} + e^+ \rightarrow \overline{H} + h\nu$
laser-stimulated recombination	$\overline{p} + e^+ + h\nu \rightarrow \overline{H} + 2h\nu$
3-body recombination	$\overline{p} + e^+ + e^+ \rightarrow \overline{H}^* + e^+$
resonant charge-exchange colliscions with positronium	$\overline{p} + Ps^* \rightarrow \overline{H}^* + e^-$

Table 1.2: Different methods how antihydrogen could be produced.

symmetry will be violated.

Both of the last two sections are typical examples of the ongoing discussions and controversal suggestions of how to approach the unsolved issue of the complete theoretical description of gravity. Observing the gravitation of antihydrogen is of particular interest, as the first direct gravitational measurement of antimatter at all.

1.4 Antihydrogen Production Methods

Following R. Greaves and C. Surko [30], there several methods known today, by which antihydrogen could be generated. An overview of the underlying processes is given in table 1.2.

The most intuitive production method is the spontaneous radiative recombination, where an antiproton recombines with a positron. To enhance the small recombination rate of this process, a photon could be added. The following laser-stimulated recombination has been experimentally tested only for the recombination of p and e^-[30] but has never been observed for the corresponding antiparticles.

Instead of the additional photon, an additional positron provides even larger enhancements of the recombination rate. As the rate of this three-body recombination is proportional to $T^{-4.5}$, lower energies can strongly increase the recombination rate. This three-body recombination process can also be optimised by replacing the two input positrons with Rydberg-positronium Ps*[1] , which is electrically neutral. This yields on the one hand a large cross-section of the process but also, on the other hand, a possibility to control the state of the created Rydberg-antihydrogen via the excitation

---

[1]Positronium Ps is an exotic atom consisting of an electron and a positron.

of the Ps. This method will be used in the AE$\overline{\text{g}}$IS-experiment, which will be described in the following section.

1.5 The AE$\overline{\text{g}}$IS-Experiment

The AE$\overline{\text{g}}$IS-collaboration has been developed out of former members of the ATHENA-collaboration that produced cold antihydrogen for the first time 2002 [7]. Hence, their knowledge can be applied on new experiments with antihydrogen that are now planned for the AE$\overline{\text{g}}$IS-project.

Figure 1.1 shows the scheme of the antihydrogen production of the AE$\overline{\text{g}}$IS-experiment.
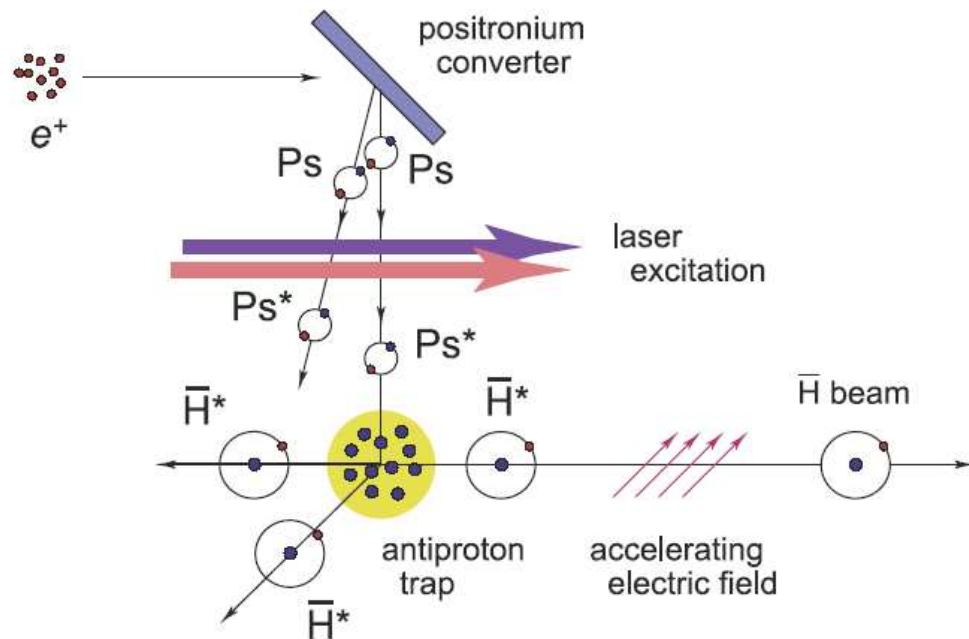
Figure 1.1: Scheme of the antihydrogen production of the AE$\overline{\text{g}}$IS-experiment at CERN. This figure is taken out of [31].

One input for the antihydrogen production via the used resonant charge exchange method are the antiprotons trapped in a penning trap (the *antiproton trap*) in a cryogenic environment. This provides us with an output of very slow antihydrogen, as their final velocity is mainly determined by the temperature of the massive particles

of the production process. Besides this, it is the excitation of the positronium[1] (*laser excitation*) to a Rydberg-state that makes this experiment unique: First of all, the $\overline{H}$-production rate is strongly enhanced as the process' cross-section σ_{CE} scales with the 4$^{\text{th}}$ power of the positronium's principle quantum n_{Ps}. This enhancement is shown in figure 1.2(a), where simulation results of AE$\overline{\text{g}}$IS-members [10] are plotted. Furthermore, the Rydberg-positronium with n_{Ps} also leads to a well-defined distribution of final states $n_{\overline{H}}$ of the antihydrogen as can be expected from the simulation results in figure 1.2(b).

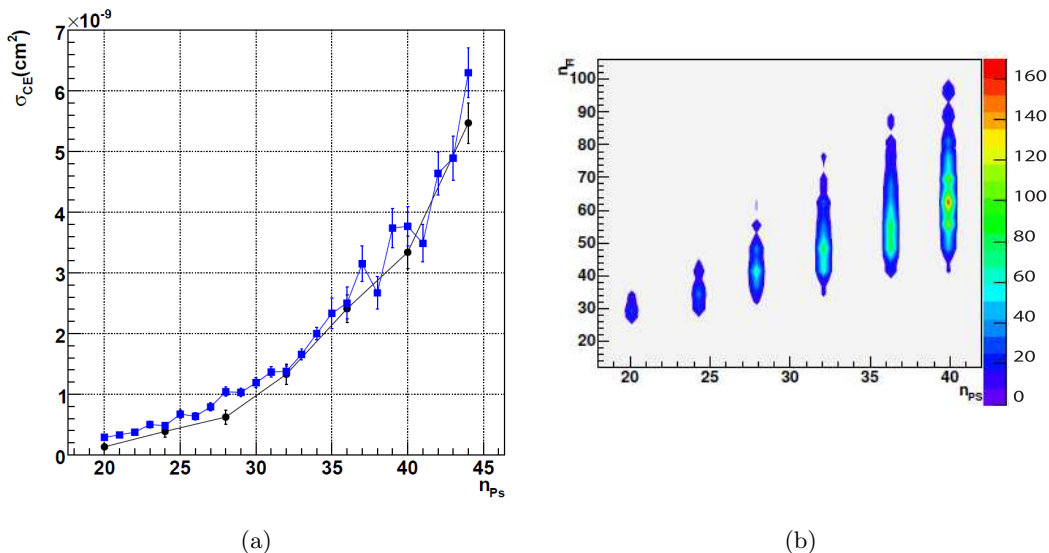Nevertheless, one of the major advantages of working with Rydberg-antihydrogen is

(a)   (b)

Figure 1.2: Predictions of simulations for the antihydrogen production of the AE$\overline{\text{g}}$IS-experiment. They show (a) the increase to the cross-section σ_{CE} by using higher energy states n_{Ps} of Ps. The dots refer to a fixed configuration of quantum numbers and the squares include a randomly chosen one and (b) the distribution of the antihydrogen's principal quantum number $n_{\overline{H}}$ on the one of the positronium n_{Ps}. Both figures are taken out of [10].

the induced sensitivity on electric fields of such a highly excited state. This can be used together with the low velocity distribution of the produced antihydrogen ($(25...80)\,\frac{\text{m}}{\text{s}}$) as the ideal initial situation for accelerating the Rydberg-states out of the $\overline{H}$-production region via inhomogenous electric fields. Such a so-called *Stark-acceleration* can reach

---

[1]The positronium is retrieved from a porous insulating material (*positronium converter*) that is bombarded with positrons e^+.

several $100\,\frac{\text{m}}{\text{s}}$.

Thus, out of the production region, a pulsed, divergent beam of Rydberg-antihydrogen can be extracted. For an appropriate apparatus to measure the gravitational acceleration of this antimatter-beam, a classical Moiré-deflectometer [22] has been suggested. The following chapters examine and characterise such a deflectometer with regard to the AE$\overline{\text{g}}$IS-setup.

Chapter 2

Theoretical Background of a Moiré-Setup

2.1 Introduction

Today's most common concept for measuring the earth's acceleration g uses a freely falling test mass, which is shaped as a corner cube [14, 15, 16, 17]. In these experiments a Michelson-interferometer for laser light is set up vertically, such that one of the interferometer's arms ends with a freely falling reflective test mass. A sketch of this setup is given in figure 2.1. The absolute value of the length change of the vertical arm is measured by counting the interference fringes at the detector. Besides the achievable high precision of the g-measurement with such a setup, it is in particular the availability as a portable apparatus, that makes this measurement concept popular [16, 17, 32]. Thus, for instance, it became a very useful tool for geophysical field measurements. Other promising concepts as the ones based on atom interferometry experiments with cold atoms [18, 19, 20] still lack this
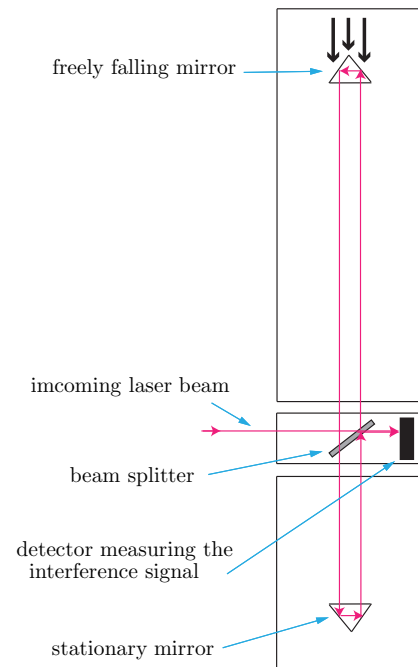

Figure 2.1: Conceptional setup of a corner-cube-experiment

freely falling mirror

imcoming laser beam

beam splitter

detector measuring the interference signal

stationary mirror

great advantage of portability.

For the usage in the AE$\overline{\text{g}}$IS-experiment, a measurement concept has to be found that can tackle the experimental conditions at CERN. As a corner cube experiment for antihydrogen is not feasible, AE$\overline{\text{g}}$IS needs to use a different gravimeter. The one chosen for the first gravitational measurements is known as *Moiré-deflectometer*.

For the theoretical background of such a Moiré-deflectometer, it is essential to distinguish between the different regimes, in which the apparaturs can be used. To characterise these regimes, we need to distinguish between setups, where wave-propagation and -interference effects are observable and the ones, for which classical ray optics and Newtonian Mechanics suffices to describe the observable effects.

We start with the mathematical description of these two regimes using lightwaves. This way, we provide a basic understanding of the setup and also the theory for some testing purposes, which will be presented in chapter 4. While one regime is governed by the propagation and interferometry of the incoming lightwaves (optical Talbot-interferometer), simple classical ray optics describes entirely the other one (optical Moiré-deflectometer).

This differentiation is then extended to matterwaves. In this context, the same regimes are interesting: the one governed by interferometric features of matterwaves (atomic Talbot-interferometer) and the one, where already Newtonian Mechanics entails the major theoretical background (atomic Moiré-deflectometer).

These considerations are finalised with a calculation of the minimal resolvable acceleration $g_{\min}$ of the setup at CERN and the one in Heidelberg. In this context, the experimental tunable parameters are examined. For the setup in Heidelberg, we can even aim to measure the effect of the moon on the earth's gravitation. The background of this effect is also outlined in a short presection right before the calculation and discussion of $g_{\min}$.

2.2   The Moiré-Effect

In order to observe the so-called *Moiré-effect*, we need to superimpose two spatial periodicities. A new periodicity, that is not imprinted in the superimposed structures, will appear, if these periodicities are characterized by a 'slight difference' from each other. Such a difference can be a variation of their periods as well as a translation or

tilt between them. Figure 2.2 (a)-(c) shows these three cases for a periodic line pattern. To be specific, we consider the case of the 'beating' of two wavelengths λ_1 and λ_2.[1]
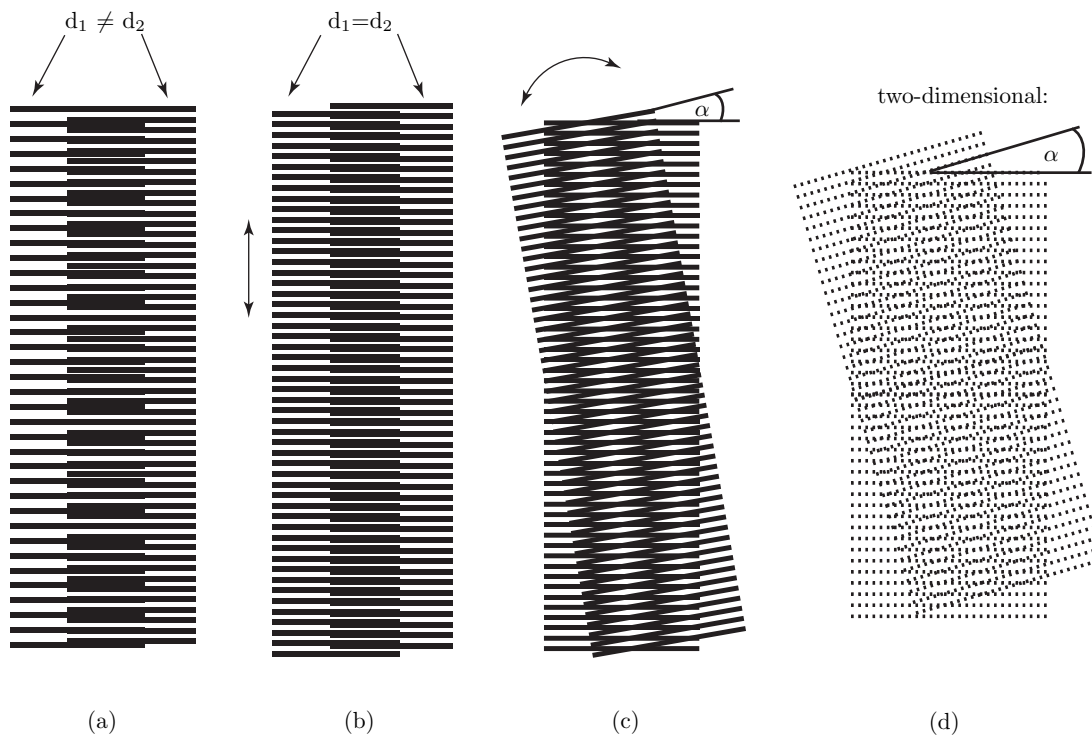

Figure 2.2: The Moiré-effect in 4 different forms of appearance: It can be caused by (a) slightly different periods, (b) a spatial shift or (c) rotation between two equal patterns; (d) it is not limited to one dimension.

The wavelength λ_3, that is created by superimposing λ_1 and λ_2, can then be calculated via

$$\frac{1}{\lambda_3} = \frac{1}{\lambda_2} - \frac{1}{\lambda_1} \Rightarrow \lambda_3 = \frac{\lambda_2\lambda_1}{\lambda_2 - \lambda_1}. \tag{2.1}$$

Analog to the beating of the two wavelengths, we find the periodicity d_3 of the structure, that is generated by two superimposed periodicities d_1 and d_2. Thus, with the angle α between the original structures d_1 and d_2 this newly generated periodicity reads

$$d_3 = \frac{d_1 d_2}{\sqrt{d_1^2 + d_2^2 - 2d_1 d_2 \cos(\alpha)}}, \tag{2.2}$$

---

[1]The 'beating' of two periodicities is rather known from superimposing two frequencies ν_1 and ν_2, where $\nu_1 \neq \nu_2$. The 'beating-frequency' ν_3 is then given by $\nu_3 = \nu_2 - \nu_1$. Their spatial representation $\lambda_i = \frac{c}{\nu_i}$ leads to equation 2.1.

which can then be observed as Moiré-effect. This effect is not limited to one dimension as illustrated in figure 2.2(d).

Besides the often undesired occurence of the Moiré-effect in photography, for example, this effect can also be a very useful tool. Thus, it has become a common method for precision measurements and engineering devices [33, 34, 35, 36, 37]. How it will be used within the AE$\overline{\text{g}}$IS-experiment is described in the following sections.

2.3 The Most General Moiré-Setup

In the following sections we present some of the possible applications of the Moiré-effect. All of them have a common basic setup that is sketched in figure 2.3. Three thin material transmission gratings $G1, G2$ and $G3$ are fabricated with the corresponding period d_i and opening width a_i of the ith grating. They are mounted at distance L_i along the z-axis and their slits are aligned parallel to the y-axis.

For a mathematical description of the different applications, we distinguish between light- and matterwaves that are sent through such a setup along the z-axis. As these waves can show diffraction effects behind tranmission gratings, we need to distinguish further between between two major ***regimes***:

1. Diffraction effects of the gratings are significant, i.e. L_i and d_i are chosen such that any displacements due to the diffraction of the wave from the material gratings are observable. In this regime, we refer to the setup as ***Talbot-interferometer***.

2. L_i and d_i are set such that diffraction effects of the wave are negligible. In this regime, we refer to the setup as ***Moiré-deflectometer***.

If not stated as L_i, d_i and a_i, we assume in the following $L_1 = L_2 = L$, $d_1 = d_2 = d$ and $a_1 = a_2 = a$.

2.4 Moiré-Setups for Lightwaves

2.4.1 Optical Talbot-Interferometer

In the regime, where diffraction effects are significant, the mode of operation of an interferometer for lightwaves is dominated by the *Talbot-effect*. We consider the diffraction
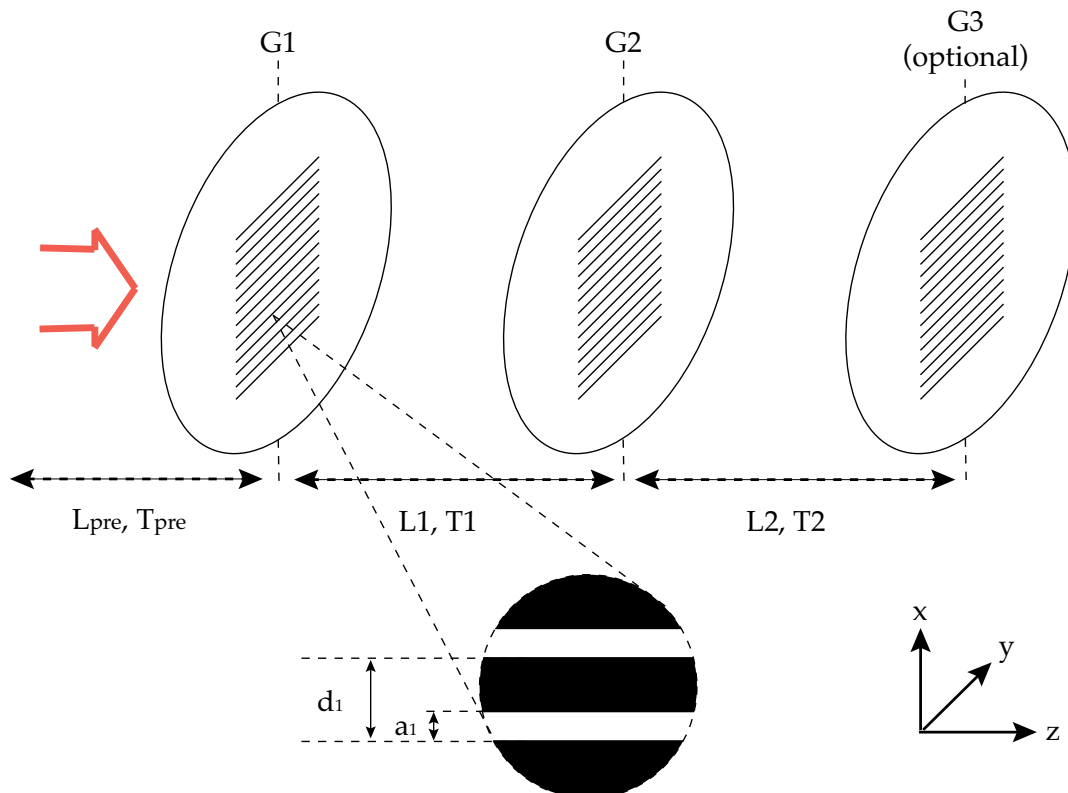
Figure 2.3: General Moiré-setup: a light- or matterwave (indicated as red arrow) travels through 2-3 thin material gratings with an opening width a_i and a period d_i. The distance L_i between two consecutive gratings determines the time of flight T_i that the particles need for a given longitudinal velocity v_z. Note that the necessity for the third grating depends on the application of the setup.

process of a lightwave from a diffraction object as a transmission grating for example. The Talbot-effect is then observable as a full re-image of the transmission function of the diffraction object at a particular distance, the *Talbot-distance z_T*[1]. To understand the occurrence of this re-imaging, it is adjuvant to analyse the propagation of waves in space after they are diffracted from a particular structure.

The following study is based on the derivations in in [38] and [39] and provides the derivation of the re-imaging effect by considering the propagation of a lightwave in Fourier space.[2]

---

[1]This distance is also often taken as orientation of the limit between 'near-' and 'far-field diffraction'.

[2]At this point, the derivation of the Talbot effect for light is described in detail as it is also chosen as test of the quality and functionality of the first produced material gratings, section 4.4. In addition

2. THEORETICAL BACKGROUND OF A MOIRÉ-SETUP

Firstly, the propagation in space of a lightwave $\psi(x, y, z, t)$ can be generally described via a scalar wave equation which in cartesian coordinates is given by

$$\Delta\psi = \frac{\partial^2\psi}{\partial x^2} + \frac{\partial^2\psi}{\partial y^2} + \frac{\partial^2\psi}{\partial z^2} = \frac{1}{c^2}\frac{\partial^2\psi}{\partial t^2}. \tag{2.3}$$

Assuming the lightwave to be monochromatic and coherent, i. e. $\psi(x, y, z, t) = e^{i\omega t}\psi(x, y, z, 0)$ simplifies equation 2.3 to the well-known *Helmholtz equation*

$$\frac{\partial^2\psi}{\partial x^2} + \frac{\partial^2\psi}{\partial y^2} + \frac{\partial^2\psi}{\partial z^2} = -k^2\psi, \tag{2.4}$$

where the wavenumber $k = |\mathbf{k}|$ is given by the light's angular frequency $\omega = c \cdot k$. Choosing the positive z-axis as the direction of propagation provides the ansatz

$$\psi(x, y, z) = f(x, y, z)e^{-ikz}, \tag{2.5}$$

which is governed by the amplitude function $f(x, y, z)$ that varies only slowly in the z-direction. This ansatz together with its associated differential equation 2.4 leads to

$$\left(\frac{\partial^2 f(x, y, z)}{\partial x^2} + \frac{\partial^2 f(x, y, z)}{\partial y^2} + \frac{\partial^2 f(x, y, z)}{\partial z^2} \right.$$
$$\left. + 2ik\frac{\partial f(x, y, z)}{\partial z} - k^2 f(x, y, z)\right)e^{-ikz} = -k^2 f(x, y, z)e^{-ikz}$$

and can be approximated with

$$\frac{\partial^2 f(x, y, z)}{\partial x^2} + \frac{\partial^2 f(x, y, z)}{\partial y^2} + 2ik\frac{\partial f(x, y, z)}{\partial z} = 0 \tag{2.6}$$

due to the slow variation of $f(x, y, z)$ in z-direction. This so-called *paraxial wave equation*, together with a given inital distribution $f(x, y, z_0)$, provides the amplitude distribution $f(x, y, z)$ at any distance z.

In order to determine the propagation of the amplitude distribution in space, we transform equation 2.6 into Fourier space to find its solution. With the Fourier pair $f(x) \xleftrightarrow{FT} F(u)$ and $f(y) \xleftrightarrow{FT} F(v)$, the two- dimensional Fourier transform of equation

---

to this, the way the Talbot-effect is derived demonstrates a neat alternative way to the solution of the Fresnel-Kirchhoff-Integral of Brezger et al. [40] presented in section 2.5.1.

2.6 reads[1]

$$(2\pi i u)^2 F(u,v,z) + (2\pi i v)^2 F(u,v,z) + 2ik\frac{\partial F(u,v,z)}{\partial z} = 0 \qquad (2.7)$$

$$\Rightarrow \frac{\partial F(u,v,z)}{\partial z} = \frac{2\pi^2 i}{k}(u^2+v^2)F(u,v,z). \qquad (2.8)$$

Integrating the latter over z finally yields the amplitude distribution in Fourier space

$$F(u,v,z) = F(u,v,0)e^{-\frac{2i\pi^2}{k}(u^2+v^2)z}. \qquad (2.9)$$

In order to apply this result to a light wave that has passed an amplitude grating, we first need to transform the grating's transmission function $t(x, z = 0)$ into Fourier space. For this purpose, we limit the following derivations to one dimension without loss of generality. With $\circledast$ denoting a convolution and the number of slits $(N-1)$, the Fourier pair[2]

$$f_{\text{grat}}(x) = \left[\sum_{l=-N/2}^{N/2} \boldsymbol{\delta}\left(\left(x + \frac{a_i}{2}\right) - ld_i\right) \right] \circledast \prod\left(\frac{x + \frac{a_i}{2}}{a_i}\right) \qquad (2.10\text{a})$$

$$\xleftrightarrow{FT} F_{\text{grat}}(u) = e^{2i\pi a_i u} \underbrace{\frac{\sin(\pi(N+1)d_i u)}{\sin(\pi d_i u)}}_{FT\text{of finite train of }\delta\text{-functions}} \frac{\sin(a_i u)}{u} \qquad (2.10\text{b})$$

describes the transmission function of a one-dimensional amplitude grating with a period d_i and rectangular openings of width a_i (see figure 2.3).

The Fourier representation of equation 2.10b can now be used as initial distribution $F(u,v,0)$ in equation 2.9 and a peculiar feature can be observed considering the amplitude distribution behind a grating: Whenever the additional phase factor $e^{-\frac{2i\pi^2 u^2}{k}z}$ of the propagation becomes unity, the observable amplitude distribution equals exactly the one directly behind the grating. Such a so-called *re-phasing* or *re-imaging* can be observed for the first time for

$$\frac{2i\pi^2}{k}\frac{1}{d_i^2}z_T = 2\pi \qquad (2.11)$$

$$\Rightarrow z_T = \frac{2d_i^2}{\lambda}, \qquad (2.12)$$

---

[1]This Fourier transform can be determined straight forward via the general properties of the Fourier pair $f(x) \xleftrightarrow{FT} F(u)$ given in Appendix A.2.

[2]A mathematical derivation based on basic properties of Fourier transformations can be found in Appendix A.

with $k = \frac{2\pi}{\lambda}$. This particular distance z_T behind the grating is known as the *Talbot distance*, named after William Henry Fox Talbot $(1800 - 1877)$ [41], who observed this effect of re-imaging of a grating's transmission function for the first time. Note that the re-images are observable at any integer multiples of z_T.

In the region between grating and Talbot distance, the so-called *fractional Talbot effect* is observerable at fractional multiples of the Talbot distance, i.e. at

$$z = \frac{n}{m}z_T, \quad \text{with } \frac{n}{m} \leq 1, \text{ and } n, m \in \mathbb{N}. \tag{2.13}$$

The derivation of the amplitude transmission function, as it is done above via Fourier transfomation, becomes very complicated in this region.

Alternatively, P. Cloetens et al.[42] solve the Fresnel diffraction integral for this near-field diffraction regime. For this purpose, they take advantage of the periodicity of the initial amplitude distribution and receive the general expression

$$f(x, z) = \frac{1}{\sqrt{2inm}} \sum_{l=0,1,\ldots 1(n-1)} c_T(n, m, l) t\left(x + \frac{ld_i}{n}, z = 0 \right), \tag{2.14}$$

where the transmission function of the grating is given by $t(x) = f(x, z = 0)$ and the *fractional Talbot coefficients* can be evaluated by

$$c_T(n, m, l) = \sum_{r=0,1,\ldots(m-1)} e^{\frac{i\pi(l+nr)^2}{2nm}}. \tag{2.15}$$

For $n = m = 1$ the expected integer Talbot effect with $f(x, z_T = 2d_i^2/\lambda) = t(x)$ follows. Other particularly interesting distances are for example

$$z = \frac{z_T}{2} \qquad \Rightarrow f\left(x, \frac{z_T}{2} \right) = t\left(x + \frac{d_i}{2} \right) \tag{2.16a}$$

$$z = \frac{z_T}{4} \qquad \Rightarrow f\left(x, \frac{z_T}{4} \right) = \frac{1}{\sqrt{2i}}\left(t(x) + it(x + \frac{d_i}{2}) \right) \tag{2.16b}$$

$$z = \frac{3z_T}{4} \qquad \Rightarrow f\left(x, \frac{3z_T}{4} \right) = \frac{1}{\sqrt{2i}}\left(it(x) + t(x + \frac{d_i}{2}) \right). \tag{2.16c}$$

Thus, the amplitude distributions behind the grating consist of a superposition of replicas of the gratings transmission function $t(x)$ which may be weighted or also shifted vertically. Particularly interesting is the distribution at half the Talbot distance, where a copy of the transmission function can be observed. Note that this copy is no complete re-image yet, as it is shifted in x-direction by half the grating period.

Furthermore, equations 2.16 also indicate the changing period of the amplitude distribution at distances in-between integer multiples of $\frac{z_T}{2}$. This change of the spatial frequency of the amplitude in x-direction suggests a possible diminishment or magnification of the images of the grating's transmission function.

Under the ideal conditions of a coherent and collimated beam, that yield a clear interference pattern in the regime close to the grating (also known as *Talbot-carpet*), we can realise an optical Talbot-interferometer. Superimposing this interference pattern with another addiditional spatial modulation yields the Moiré-effect. For this additional spatial modulation, it is convenient to use a second material grating, which is then scanned parallel to the first one along the x-axis. This provides us a useful analysing tool, with which we can examine the amplitude distributions of equations 2.16 . We will use this technique to test transmission gratings on possible defects (see section 4.4).

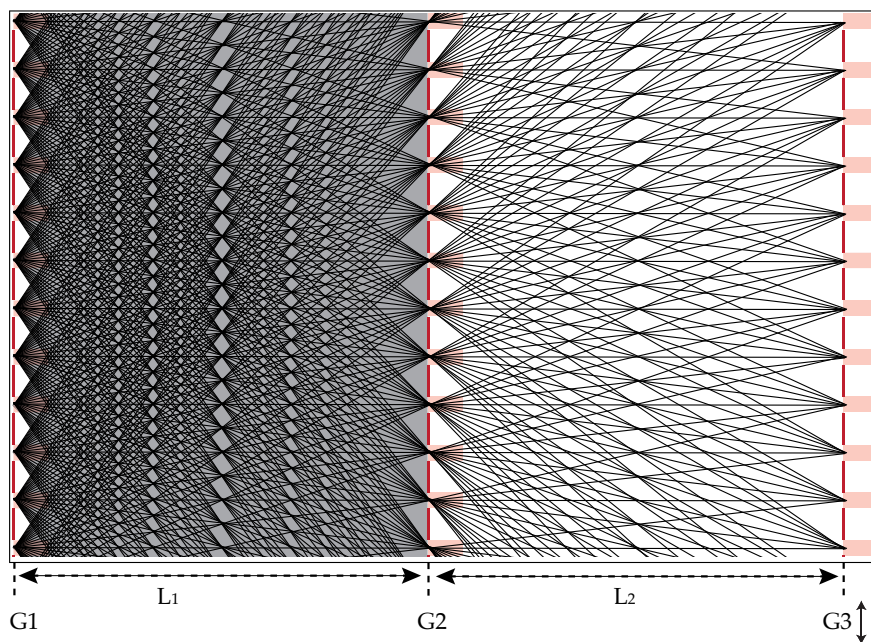### 2.4.2 Optical Moiré-Deflectometer

Figure 2.4: Shadow effect of classical optical rays travelling through a Moiré-setup. The gratings' openings are expected to be point-like here.

So far, the wavelength λ and grating period d_i have been chosen such that interference effects of the diffracted wave play a crucial role for the output of the Moiré-setup.

Varying these parameters can lead to a regime with very large Talbot distance $z_T = \frac{2d_i^2}{\lambda}$ and where diffraction effects become negligible. This can be reached by either increasing d_i, the size of the grating's period, or by approaching the limit of $\lambda \to 0$. Either way, we will find a corresponding mathematical description that is simply governed by classical ray optics.

For a qualitative understanding of this regime, figure 2.4 provides a sketch of the possible paths of optical rays in a Moiré-setup that consists of three identical gratings. The grey background denotes the rays that pass the first grating $G1$ but are blocked by the second one $G2$. Hence, the first grating's transmission function is washed out shortly behind $G1$ and we need to find a way to uncover it again. Considering the optical rays that pass the setup of the two consecutive gratings $G1$ and $G2$ (solid black lines) shows clearly the reappearance of the gratings' spatial modulation with period d_i at distance L_2. Thus, it is actually the additional blocking of $G2$ that uncovers the shadow picture at L_2.

In order to examine this self-focusing effect of $G1$ and $G2$, it is convenient to use a third grating $G3$. This last grating probes the created shadow pattern at L_2 by moving along the x-direction. Hence, it serves as analysing tool as did the second grating in the previously described Talbot-interferometer.

Besides this general shadow-image of the gratings, we can even observe harmonics of them at distances $L_2' = \frac{m}{n}L_2$, with the integer numbers m and n.

Note that in this optical-ray-description, the results are independent of the coherence and collimation of the incoming light. This makes this Moiré-deflectometer very robust to experimental imperfections.

2.5   Moiré-Setup for Matterwaves

Setting up an interferometer for atomic beams reveals an important difference between lightwave- and matterwave-diffraction experiments: While the wavelength λ of laser light is well-defined with typically $\frac{\Delta\lambda}{\lambda} \approx 10^{-9}$, the deBroglie wavelength λ_{dB} of an atomic beam is generally given by a broad distribution. This can be narrowed by collimating the atomic beam.

Most of today's atom interferometer work with collimated atomic beams. Hence, monochromatic matterwaves can be assumed, which, in analogy to the diffraction of

light, enables the observation of the Fresnel-diffraction-regime and the Talbot-effect [43, 44]. Besides this, the Fraunhofer-diffraction-regime (far-field-diffraction), that can be observed with these beams [45, 46, 47], is particularly interesting. For the latter regime, the different diffraction orders are not allowed to overlap, such that the first grating serves as beam splitter. Such a Mach-Zehnder-setup – also known as *Seperated-Beam-Envelope-interferometer* (SBE) [48] – allows to manipulate the path of only one diffraction order, while leaving the other one unaffected. The interference of the two orders at the end of the interferometer then offers a broad range of fundamental studies. However, such a SBE-interferometer has a couple of disadvantages: Besides a high sensitivity on the gratings' misalignment, the incoming wave has to be well prepared in direction and collimation to ensure a proper spatial separation of the diffraction orders. Furthermore, for most collimation techniques, the flow of atoms provides a severe limit to the resolution of the interferometer [48]. This can be solved by a less collimated beam and gratings with a larger aperture. How such a beam can be used in atom interferometry is shown in the following section.

2.5.1 Atomic Talbot-Interferometer

Independently from the degree of collimation of the atom beam, we can observe in analogy to light, a re-imaging-effect – the atomic Talbot-effect – for matterwaves in the near-field diffraction regime, i. e. at distances $z \sim z_T$. The matterwave distribution at specific distances behind the transmission grating can be either found using the properties of the Fourier-transform as done for light in section 2.4.1 or by solving the Fresnel-Kirchhoff-Integral. The latter method has been pursued by Brezger et al.[40] to evaluate explicitly the output of a divergent atomic beam traveling through a Talbot-interferometer. The following considerations follow their publication.

As opposed to the previously described atomic Mach-Zehnder-interferometer, a general atomic Talbot-interferometer does not need a collimated beam. The lack of coherence can be handeled by an incoherent summation over the atoms that are transmitted by the first grating $G1$.[1] With a three-grating setup, this still yields a re-imaging effect of the grating's transmission function, but there is a strong dependence of the pattern on

---

[1]The incoherent summation describes an addition of Talbot fringe patterns that miss any phase synchronisations – the Lau-effect. Therefore, these kind of interferometers are also often called *Talbot-Lau-interferometers*.

the distance between the gratings. The geometry of the setup has to fulfill the so-called *period matching condition*. It reads [40]

$$\frac{1}{r_1}\frac{d_2}{d_1} + \frac{1}{r_2}\frac{d_2}{d_3} = 1, \tag{2.17}$$

with $r_1 = \left(\frac{L_1+L_2}{L_2}\right)\frac{d_2}{d_1}$ and $r_2 = \left(\frac{L_1+L_2}{L_1}\right)\frac{d_2}{d_3}$. Hence, the choice of geometric parameters is strictly limited for this type of interferometer.

Particularly interesting for a potential application in the AE$\overline{\text{g}}$IS-experiment are the considerations of Brezger et al. concerning possible interactions between the gratings' surfaces and the transmitted wave: In the Eikonal approximation, i.e. with a linear propagation within the grating's potential, the transmission function $t_i(x)$ changes to [40]

$$t_{i,\text{int}}(x, z) = t_i(x) \cdot \underbrace{e^{-\frac{i}{\hbar}\int V(x,z(t))dt}}_{\text{additional phase grating}}, \tag{2.18}$$

where $\int V(x, z(t))\, dt$ denotes the additional potential integrated over the interval, for which the interaction holds on. The additional phase grating neither affects the functionality of $G1$ nor that of $G3$: at $G1$ incoherent particles have been assumed anyway and $G3$ only acts as mask for a subsequent flux-measurement. Hence, the additional phase grating of equation 2.18 only matters at $G2$.

Nevertheless, this effect should not be neglected. The integration in equation 2.18 indicates an additional dependence on the particles' longitudinal velocity component v_z. Numerical results of Brezger et al. show that this additional dispersive grating property can break up the periodic re-imaging effect: Dependent on the atomic species, the re-images are still observable at z_T and $\frac{z_T}{2}$ but appeared blured in-between and may even disappear in these regions. Consequently, changing the geometric parameters in the AE$\overline{\text{g}}$IS-experiment to values, for which the setup is rather acting as Talbot-interferometer, requires particular care of the period matching condition.

2.5.2 Atomic Moiré-Deflectometer: Newtonian Mechanics Producing the Shadow-Effect

As for lightwaves, one can change the geometry of an atomic Talbot-interferometer such that diffraction effects become negligible. For this purpose, the diffraction effects of λ_{dB} from the grating with period d_i have to be smaller than a grating period at the
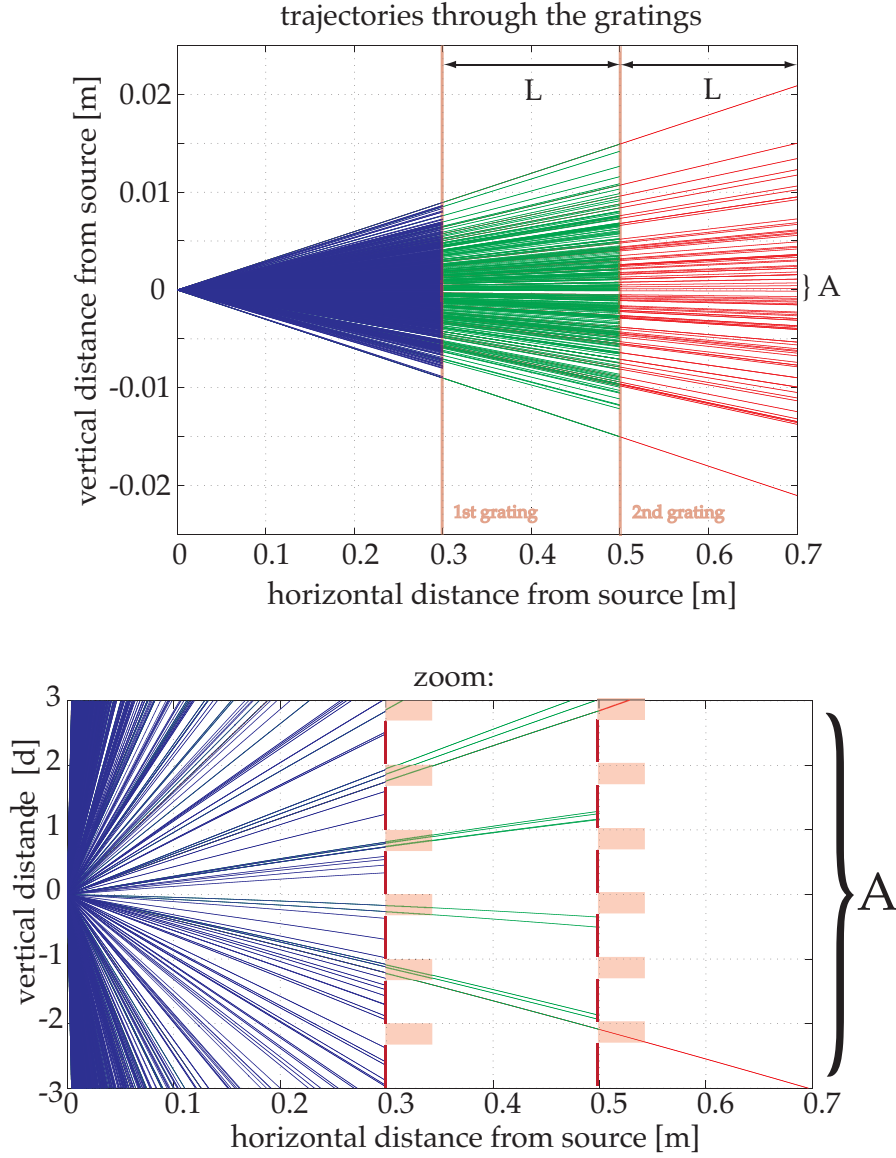
trajectories through the gratings

zoom:

Figure 2.5: The top figure shows examplary the classical trajectories of 1000 argon atoms (coming from a point-like source 30 cm in front of the first grating with an initial transversal temperature of 100 mK and a longitudinal velocity of 430 m/sec) traveling through the Moiré-deflectometer with a grating distance of 20 cm. The bottom picture provides a zoom-in into the central region A. The red shaded regions denote the regions of particle transmission of the gratings.

distances L_i of interest. Thus, $z_T = \frac{2d_i^2}{\lambda_{dB}}$ is very large in this regime, which can then be

characterised by

$$d_i \gg \sqrt{\lambda_{\mathrm{dB}} L_i}. \tag{2.19}$$

The setup of such an atomic Moiré-deflectometer [22] makes use of the atomic analogon of the optical shadow-effect described in section 2.4.2.

In order to determine the atoms' trajectories through a deflectometer analytically, it is sufficient to apply classical Newtonian Mechanics via

$$\mathbf{F}(t) = m\frac{d\mathbf{v}}{dt}, \tag{2.20}$$

where $\mathbf{F}(t)$ is the net force of the atomic motion at time t, m is the mass and $\mathbf{v} = (v_x, v_y, v_z)$ is the velocity of the moving particle, respectively. Solving the differential equations that follow from equation 2.20 leads to the vertical component $x(t)$ of the trajectory of a freely moving particle in the gravitational field given by

$$x(t) = x_0 + v_{x0}t - \frac{1}{2}gt^2, \tag{2.21}$$

with the gravitational acceleration g, the particle's initial position x_0 and its corresponding velocity v_{x0}. Note the orientation of the coordinate system as it is drawn in figure 2.3: The x-axis is pointing vertically upwards.

For a 'field-free' deflectometer region without any disturbing magnetic or electric fields[1] and under the condition to pass two transmission gratings, equation 2.21 yields a shadow pattern at the end of the deflectometer that re-images the gratings' transmission functions.

Analytically, these re-images can be found by considering the condition to pass one of the gratings more into detail. Passing the gratings is illustrated in figure 2.5, which shows a zoom into the center of one of the gratings. The transmission function $t_i(x), i = 1, 2$, of one of these amplitude gratings can be expressed as a convolution (denoted by $\circledast$) between a train of $\boldsymbol{\delta}$-functions and the so-called 'top-hat-function' $\prod(x)$,

$$t_i(x) = \sum_{k=-N_{\mathrm{slits},i}/2}^{N_{\mathrm{slits},i}/2-1} \boldsymbol{\delta}\left(\left(x + \frac{a_i}{2}\right) - kd_i\right) \circledast \prod\left(\frac{x + \frac{a_i}{2}}{a_i}\right), \tag{2.22}$$

---

[1]A detailed study of disturbing magnetic and electric fields can be found in chapter 3.

with the grating's total number of slits $N_{\text{slits},i}$, its period d_i and opening width a_i.[1] Consequently, these grating-properties determine the conditions on the vertical coordinate x_{Gi} of a particle to pass the ith grating. To be specific, the conditions for the first two gratings are given by (see figures 2.3 and 2.5):

1. A particle passes the 1st grating if

$$x_{G1} \overset{!}{=} x(T_{\text{pre}}), \text{ with } x_{G1} \in t_1(x) \tag{2.23a}$$

$$\Rightarrow x_0 = x_{G1} - v_{x0}T_{\text{pre}} + \frac{1}{2}gT_{\text{pre}}^2 \tag{2.23b}$$

2. A particle passes the 2nd grating if

$$x_{G2} \overset{!}{=} x(T_{\text{pre}} + T_1), \text{ with } x_{G2} \in t_2(x) \tag{2.24a}$$

$$\Rightarrow x_0 = x_{G2} - v_{x0}(T_{\text{pre}} + T_1) + \frac{1}{2}g(T_{\text{pre}} + T_1)^2 \tag{2.24b}$$

As both conditions have to be fulfilled for a particle to contribute to the shadow-image at the end of the deflectometer, equation 2.23b and 2.24b yield a condition on the initial vertical velocity given by[2]

$$v_{x0} = -\frac{1}{T_1}x_{G1} + \frac{1}{T_1}x_{G2} + gT_{\text{pre}} + \frac{1}{2}gT_1. \tag{2.25}$$

To sum up, for a particle to reach the detection region of the deflectometer its initial position and velocity needs to fulfill equation 2.23b and 2.24b and its velocity is conditioned by 2.25. The vertical position at the detection region reads then

$$x(T_{\text{pre}} + T_1 + T_2) = x_0 + v_{x0}(T_{\text{pre}} + T_1 + T_2) - \frac{1}{2}g(T_{\text{pre}} + T_1 + T_2)^2 \tag{2.26}$$

$$= -\frac{T_2}{T_1}x_{G1} + \left(1 + \frac{T_2}{T_1}\right)x_{G2} - \underbrace{\frac{1}{2}gT_1T_2}_{1^{st}\leftrightarrow 2^{nd}\text{grating}} - \underbrace{\frac{1}{2}gT_2^2}_{\text{behind } 2^{nd}\text{grating}} . \tag{2.27}$$

This analytic expression reveals some remarkable features as the re-imaging effect of the gratings' transmission functions: The first two terms represent a kind of beating

---

[1]Further details on the mathematical expression of the transmission function are given in Appendix A.

[2]Note that due to this limitation on the initial transversal velocities, such a two-grating-setup is also sometimes referred to as 'collimation'.

of the two transmission functions, with $x_{G1} \in t_1(x)$ and $x_{G2} \in t_2(x)$. Hence, the exact spatial periodicity of the resulting pattern depends on the ratio of the distances L_1 and L_2 that determine $\frac{T_2}{T_1}$. Furthermore, it is important to note that the final position in equation 2.27 is completely independent of T_{pre}. This emphasizes the independence on the degree of collimation of the incoming atomic beam. Besides this, the effect of gravity – a vertical shift of the whole pattern – can be seperated into two parts as indicated by the terms with underbraces: one originating from the gravity present inbetween the two gratings and one resulting exclusively from gravity that is present behind the second grating.

Particularly interesting is the case of a setup with equal distances L_i, i. e. with $T_1 = T_2 = T$. Equation 2.27 becomes then

$$x(T_{\text{pre}} + 2T) = - \underbrace{x_{G1}}_{1^{\text{st}}\text{grating}} + 2 \cdot \underbrace{x_{G2}}_{2^{\text{nd}}\text{grating}} - gT^2. \qquad (2.28)$$

For identical gratings, the addition of the first two terms in equation 2.28 leads to a clear re-image of the grating's transmission function at the end of the deflectometer. Furthermore, the effect of gravitation as simple offset shift becomes particularly useful for sensitivity analysis of any type of accelerating forces. Before presenting such analysis, we provide more details about the potential application of a Moiré-deflectometer as accelerometer.

2.6   The Characteristic Moiré-Pattern of a Deflectometer

In order to use an atomic Moiré-deflectormeter as accelerometer, the following section gives a deeper insight in the characteristic pattern that is expected as the output of this device. Generally, the output of a three-grating-setup is given by a fringe pattern, that results from the re-image of the first two gratings. A vertical scan of the third grating over this pattern provides us the signal to be analysed.

For a setup with $L_1 = L_2 = L$, i. e. $T_1 = T_2 = T$, we expect the pattern to be a clear image of the grating's transmission function (see equation 2.27). However, as we work with transmission gratings with an opening width $a_1 = a_2 = a$ (see figure 2.3), we need to take a closer look on this image. For this purpose, figure 2.6(a) shows some of the possible paths through the deflectometer. For a deflectometer with identical gratings,

(a) Moiré-setup with finite openings a

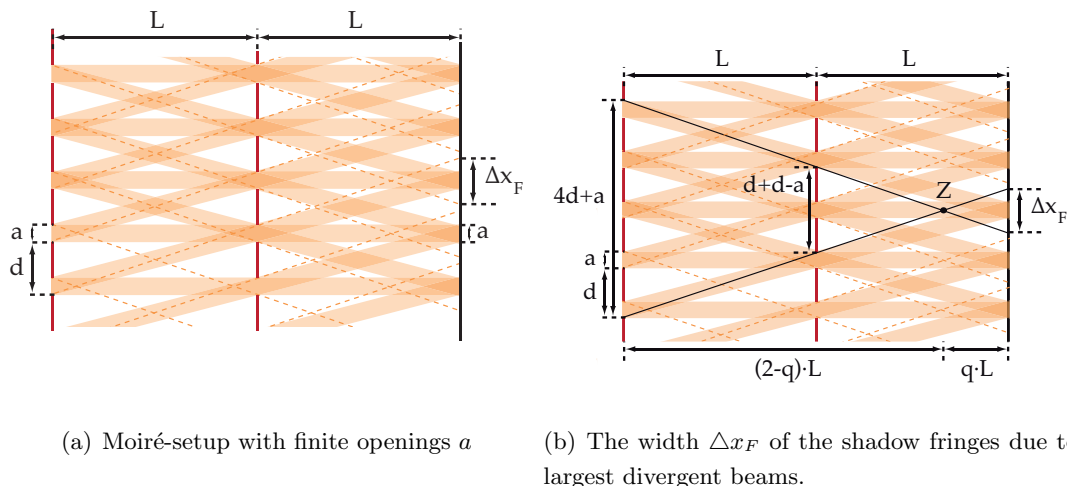(b) The width $\triangle x_F$ of the shadow fringes due to largest divergent beams.

Figure 2.6: Sketches of the shadow-effect for gratings for a two-grating Moiré-setup with $L_1 = L_2 = L$. The identical gratings are defined by their periods d and their openings a. Opposed to figure 2.4 these openings are not taken to be point-like. In figure 2.6(b) q denotes a fractional number with $0 < q < 1$.

i.e. $d_1 = d_2 = d$ and $a_1 = a_2 = a$, this figure illustrates interesting features of the image[1]:

- Due to the geometry of the setup, only the particles that contribute to one of the fringes are transmitted through the setup, regardless from which opening they originate. Note that in the figures of 2.6, we included only the contributions from the next neighbouring slits. This can be easily extended to all slits and does not change the width $\triangle x_F$ of the fringe. The validity of this statement for all paths over the entire grating area becomes clear by comparing this situation to the shadow-effect drawn in figure 2.4.

- In order to describe the shape of one fringe of the pattern, we need to consider the contributions of the paths with the largest possible divergence. These paths are denoted by the dotted lines. Using the example in figure 2.6(b), that is accentuated by the black solid lines, we find with the intercept theorem two

---

[1]Due to its modified shape as train of trapeze, we also refer to this re-image right before the third grating as fringe pattern.

2. THEORETICAL BACKGROUND OF A MOIRÉ-SETUP

geometric conditions[1]:

$$1. \quad \frac{\triangle x_F}{d + d - a} = \frac{q \cdot L}{(1 - q) \cdot L} \tag{2.29a}$$

$$2. \quad \frac{\triangle x_F}{4d + a} = \frac{q \cdot L}{(1 + 1 - q) \cdot L}. \tag{2.29b}$$

They yield

$$q = \frac{\triangle x_F}{2d - a + \triangle x_F} \qquad \text{and} \tag{2.30a}$$

$$\triangle x_F = 3a. \tag{2.30b}$$

This width $\triangle x_F$ provides us a measure of the 'smearing' out of the pattern.

To sum up, for a classical Moiré-deflectometer as in our experiments, we can expect – even for large divergent beams – a fringe pattern right before the third grating, that consist out of a train of smeared-out top-hat-functions. The degree of 'smearing-out' is determined by the grating's opening width a.

We confirmed these expectations by Monte-Carlo simulations of the experiment in Heidelberg. Figure 2.7 shows their results for an input of $5 \cdot 10^9$ atoms[2].

Furthermore, figure 2.7 shows with the upper plot the pattern right before the third grating without any external forces, whereas the lower plot shows the same simulation with additional gravitational force. Following equation 2.28, a vertical shift $\triangle x_g$ is expected for the entire pattern. For $L = 1\,\text{m}$, $d = 40\,\mu\text{m}$ and a longitudinal velocitiy of $v_z = 430\,\frac{\text{m}}{\text{sec}}$, this shift writes

$$\triangle x_g = 53\,\mu\text{m} = 1.3 \cdot d, \tag{2.31}$$

which is clearly visible in the results of our simulations.

---

[1]This particular example has been chosen mainly for illustration reasons: It is the case, where the largest divergence due to the slidwidth a is visible and still resolvable in a drawing. The universal validity for the entire grating again results from the applicable shadow-effect of figure 2.4

[2]For these simulations (as for all simulations, if not stated differently), we assumed normally distributed initial values for x_0 and v_{x0}, corresponding to the currently implemented source (width= $2.2\,\text{cm}$) and to room temperature, respectively.
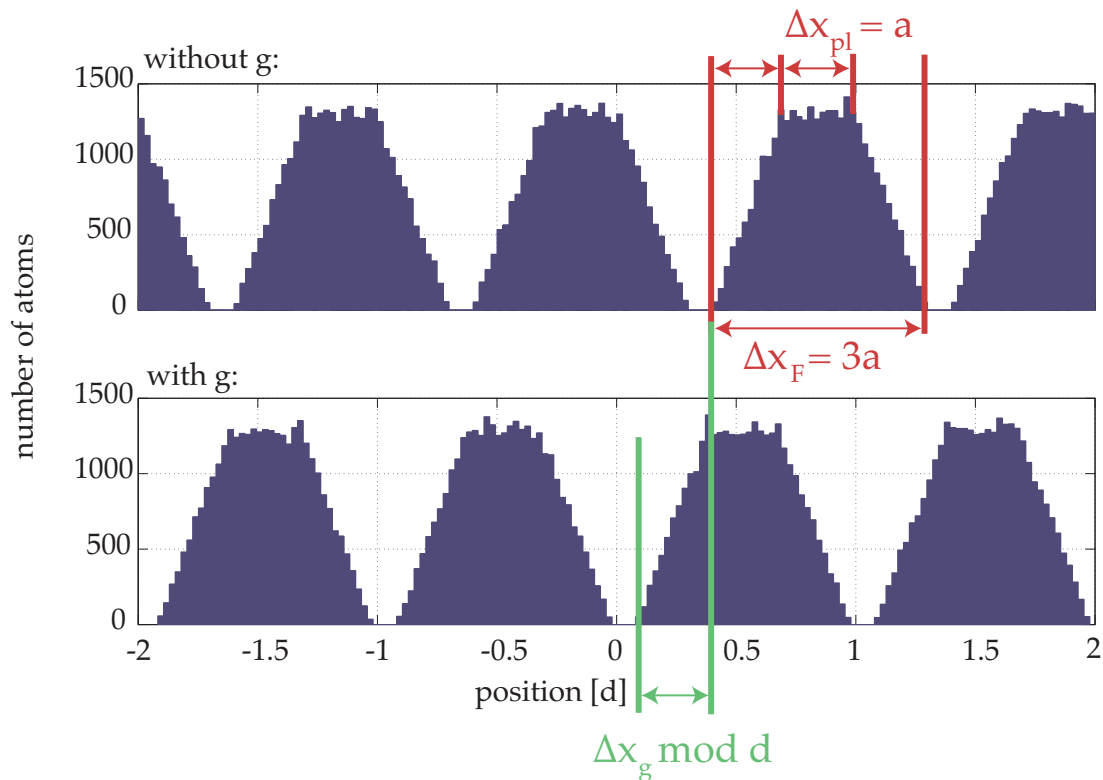
Figure 2.7: Characteristic Moiré-pattern of the deflectometer for the experiment in Heidelberg. These results of Monte-Carlo simulations show a zoom into the central periods of the pattern right before the third grating. The upper (bottom) plot corresponds to the pattern without (with) the gravitational forces.

2.7 The Moiré-Deflectometer as Gravimeter

In order to apply a Moiré-deflectometer as gravimeter for the AE$\overline{\text{g}}$IS-exeriment, some important quantities need to be defined for the apparatus first. Thus, the following subsections introduce the setups sensitivity S that yields the minimal resolvable gravitational acceleration $g_{\min}$. As this strongly depends on the corresponding experimental conditions, we have to distinghish between the conditions in Heidelberg, working with matterwaves of a high-flux source of metastable argon, and the ones at CERN, working with a low-flux source of antihydrogen. These different conditions lead to different possible applications: Being an absolute gravimeter with a very limited $g_{\min}$ for antihydrogen, the deflectometer for the argon source turns out to even reach a $g_{\min}$ with which we are able to measure the influence of the moon on the earth's gravitational accelera-

tion. How this influence can arise and a rough estimation of its order of magnitude is precedingly given in the following.

2.7.1 Moiré-Deflectometer for Tidal Forces

Following Newton's gravitational law, the magnitude of the earth's gravitational acceleration on a point-like mass can be evaluated via [49]

$$g(r_{\mathrm{E}}) = G \frac{m_{\mathrm{E}}}{r_{\mathrm{E}}^2}, \tag{2.32}$$

with the mass of the earth m_{E}, its radius r_{E} and the gravitational constant G. In fact, g has a lot more dependencies than the ones predicted by Newton. For instance, some of them are of geophysical origin (e.g. the structure of the earth crust), others originate from the rotation of celestial bodies [18].

It is known that g also depends on the moon-earth rotation, which can be explained by a more sophisticated model than the one that yields to equation 2.32 and is based on point-like masses. For this model, we choose spatially extended masses as indicated
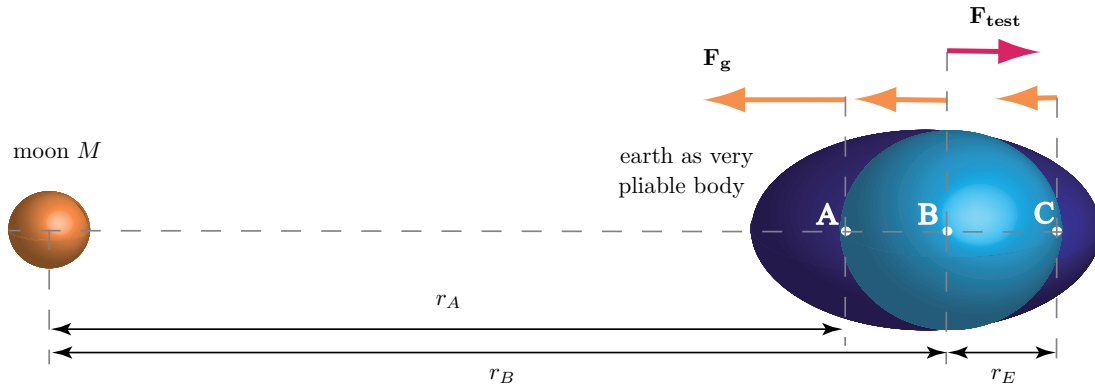

Figure 2.8: Sketch of the force balance between the attraction of the moon and the earth and the resulting net forces that change the shape of a pliable body as the earth.

in figure 2.8. In particular, we assume the earth E not only to be spatially extended but also very pliable. For a better understanding of the situation on the earth at the points A and C, we introduce now a so-called 'test-force' $\mathbf{F}_{\mathrm{test}}$ [50]. The strength of this force is equal to the gravitational one of the moon but it acts in opposite direction. In this situation, the test force $\mathbf{F}_{\mathrm{test}}$ can compensate the gravitation for only one of the points A, B or C at the time. Thus, if the test force compensates the gravitation of the

moon at point B, its magnitude will be too weak to compensate the entire gravitation of the moon at A and too strong for the situation at point C. Consequently, A still experiences a weak attraction towards the moon M and C is weakly pulled away from M.

As A, B and C are connected to each other via the pliable earth, the earth becomes quenched as indicated by the dark blue shadow in figure 2.8.

In the described moon-earth-situation the test-force $\mathbf{F}_{\text{test}}$ is simply the centrifugal force that originates from the moon-earth rotation around the common center of mass.[1] Following the given quantitative description and with $r_{\text{E}} \ll r_{\text{B}}$, the net acceleration that the moon excerts to point A can be found as [49]

$$g_{\text{M}} = -\frac{2Gm_{\text{M}}r_{\text{E}}}{r_{\text{B}}^3}. \tag{2.33}$$

with the mass of the moon m_{M} and the distances as indicated in figure 2.8. Comparing this to the total value g of the equation 2.32, we find

$$\left|\frac{g_{\text{M}}}{g}\right| = 2\frac{m_{\text{M}}}{m_{\text{E}}}\left(\frac{r_{\text{E}}}{r_{\text{B}}}\right)^3 \tag{2.34}$$

$$\Rightarrow |g_{\text{M}}| \sim 10^{-7}g. \tag{2.35}$$

Hence, in order to measure any influence of the attractional force of the moon – the so-called *tidal effect* – an experiment has to be able to resolve a minimal acceleration of $g_{\text{min}} = 10^{-7}g$. We will show in the following that this limit is reachable with the Moiré-setup in Heidelberg. Hence, it is the ideal precision test for our setup.

2.7.2 Minimal Resolvable Acceleration of a Moiré-Deflectometer

The gravitational resolution $\mathcal{R}_g$ of the Moiré-deflectometer – i.e. the infinitesimal change of the deflectometer's output resulting from an infinitesimal change of g – is found by considering the spatial shift $\triangle x_g$ that is caused by gravitation. Assuming a setup with $L_1 = L_2 = L$ and $d_1 = d_2 = d$ (see figure 2.3) and with $\triangle x_g = gT^2$ (see equation 2.28), the actual output of the deflectometer consists of a shadow pattern that re-images the grating's transmission function. Hence, the output is as periodic as the

---

[1]Note that at real scales, this point lies within the earth due to the huge mass-imbalance between the moon and the earth.

gratings are and the observable phase shift $\triangle\varphi_{\text{shadow}}$ of the shadow pattern, that is induced by g, can be determined via

$$\frac{\triangle\varphi_{\text{shadow}}}{2\pi} = \frac{\triangle x_g}{d} \tag{2.36}$$

$$\Rightarrow \quad \triangle\varphi_{\text{shadow}} = 2\pi\frac{\triangle x_g}{d} = 2\pi\frac{T^2}{d}g. \tag{2.37}$$

This yields a resolution of the setup [22]

$$\mathcal{R}_g = \frac{\partial\varphi_{\text{shadow}}}{\partial g} = \frac{2\pi}{d}T^2 \tag{2.38}$$

$$= \frac{2\pi}{d}\frac{L^2}{v_z^2}, \tag{2.39}$$

where a single, well-defined longitudinal velocity v_z has been assumed[1].

Further assuming a Poissonian distribution of the events that generate the shadow pattern yields a signal to noise ratio proportional to $\sqrt{N_{\text{data}}}$, where N_{data} denotes the total number of these events. In addition to this, this ratio has to be weighted with the fringe contrast C of the pattern in order to account for its visibility. This visibility strongly depends on experimental conditions as the gratings' opening fractions or the particles' velocity distributions[2], for instance. Thus, the sensitivity $\mathcal{S}$ of the setup, which determines the minimal gravitational acceleration that can be measured per unit time, reads [22]

$$\mathcal{S} = \frac{1}{\mathcal{R}_g C\sqrt{n_{\text{unit}}}}, \tag{2.40}$$

where the average count rate per unit time $n_{\text{unit}} = \frac{N_{\text{data}}}{t}$ and the time interval t for taking N_{data} events has been introduced. Hence, the minimal resolvable acceleration g_{min} of the apparatus can be determined by

$$g_{\text{min}} = \frac{\mathcal{S}}{\sqrt{t}} \tag{2.41}$$

$$= \frac{d}{2\pi C}\frac{v_z^2}{L^2}\frac{1}{\sqrt{N_{\text{data}}}}. \tag{2.42}$$

This already points out the dependence on the number of contributing particles and measurement time. Furthermore, the exact conditions of the source – as its velocity

---

[1]Effects concerning the more realistic case of a whole distribution for v_z can be found in Chapter 5.

[2]A detailed discussion of the visibility dependence on some experimental conditions can be found in Chapter 4 and 5.

distributions, for example – have an additional influence on C. This will be covered in detail in section 5.2. For now, we can compare the setup at CERN with the one in Heidelberg and find for the latter a decrease of $g_{\min}$ of up to five orders of magnitude. The limits of both setups and their dependencies on some experimentally tunable parameters are discussed in the following two paragraphes.

$g_{\min}$ of the Ar*-experiment

In order to determine the smallest acceleration $g_{\min}$ that is measurable in the Ar*-experiment, equation 2.42 provides the major theoretical dependencies. As the actually reachable value strongly depends on the exact experimental setup, the following paragraphs summarise the influence of the parameters that are experimentally tunable to a certain extent.

These dependencies are plotted in figures 2.9 and 2.10. Note that for all of them, the blue lines in the corresponding upper plots are $g_{\min}$-values of data that is retrieved from $1\,\mathrm{s}$ of measurement, whereas the red lines in the lower plots belong to data integrated over $20\,\mathrm{min}$. This particular time integration has been chosen as it is small enough to resolve the periodicity of the tidal effect of about $12\,\mathrm{h}\,25\,\mathrm{min}$ with a satisfying sampling rate and is large enough to achieve the desired $g_{\min} \sim 10^{-7} g$.[1] The range of the periodic variation of the absolute value of g is shaded green in the figures. As soon as the reachable value of $g_{\min}$ is smaller than this bar, the tidal effect of the moon is resolvable with the setup. Note the dashed vertical lines in all figures of this section: They indicate the current values of the experiment. An overview of them is given in table 2.1.

Considering the dependencies in detail, we stress the importance of the performance of the atomic source in figure 2.9. The best tunable source parameters and their impact on N_{data} and therewith on $g_{\min}$ are shown. Concerning the range of feasible source diameters, figure 2.9(a) demonstrates that the range is not large enough to change $g_{\min}$. Nevertheless, this subfigure accentuates the significant decrease of $g_{\min}$ that can

---

[1]Concerning the Nyquist-Shannon sampling theorem, it is in principle possible to integrate for a longer time and still resolve the frequency of the moon's acceleration. However, we need to keep this integration time as short as possible, in order to stay independent from any disturbing forces. Furthermore, the frequency of the moon's acceleration is superimposed by other periodic effects of e. g. other celestial bodies [18]. This might also lead to an adulteration of the integrated signal if the sampling rate of the moon's periodicity is too long.

parameter	current value
source diameter	$13\,\mathrm{mm}$
transversal velocity width	$80\,\frac{\mathrm{m}}{\mathrm{s}}$
longitudinal velocity	$430\,\frac{\mathrm{m}}{\mathrm{s}}$
source flow	$3.8 \cdot 10^{14}\,\frac{\mathrm{atoms}}{\mathrm{s}}$
grating distance	$1\,\mathrm{m}$
contrast	*0.8*

Table 2.1: Current experimental parameters of the setup in Heidelberg, which are experimentally accessible and influence the achievable minimal resolable acceleration $g_{\min}$ of the Moiré-deflectometer. The contrast is written in italics, as the best achievable value is assumed here, which has not been measured yet.

be reached by the 20 min-integration time. The same effect can be observed in figure 2.9(b), which shows the expected linear dependence on the initial transversal velocity v_{x0} of the atoms. Even for atoms with $v_{x0} = 100\,\frac{\mathrm{m}}{\mathrm{s}}$ the tidal effect remains resolvable.

Particularly interesting is the dependence on the flow of the source plotted with a logarithmic scale in figure 2.9(c). Even an increase beyond the current value of $3.8 \cdot 10^{14}\,\frac{\mathrm{atoms}}{\mathrm{s}}$ will not improve the measurement of $g_{\min}$ significantly. Furthermore, the proposed integration time suffices already to resolve the tidal effect with the current atomic flow.

As last source property, figure 2.9(d) shows the effect that the atoms' longitudinal velocity has within their accessible range. At this point, it is important to note that the loss of contrast, that a broad velocity distribution yields, is not yet included. This is be covered in section 5.2. Consequently, the current value of the contrast, whose dependence is plotted in figure 2.10(a), is not determinable at this stage. Nevertheless, the plotted dependence emphasises the necessity to reach a value of about $C \sim 0.5$. Below this value, $g_{\min}$ increases very quickly to ranges, where even the time integration of 20 min cannot resolve the tidal effect any more. Furthermore, beyond $C \sim 0.5$ the measurements improvement slowly stagnates. This is particularly interesting for estimations of disturbing fields as it is done in subsection 3.2.

In Figure 2.10(b) the plotted proportionality to $\frac{1}{L^2}$ points out that the chosen distance of 1 m not only yields a satisfying value for $g_{\min}$ after 20 min of integration, it also demonstrates that – with the current experimental conditions in Heidelberg – only a
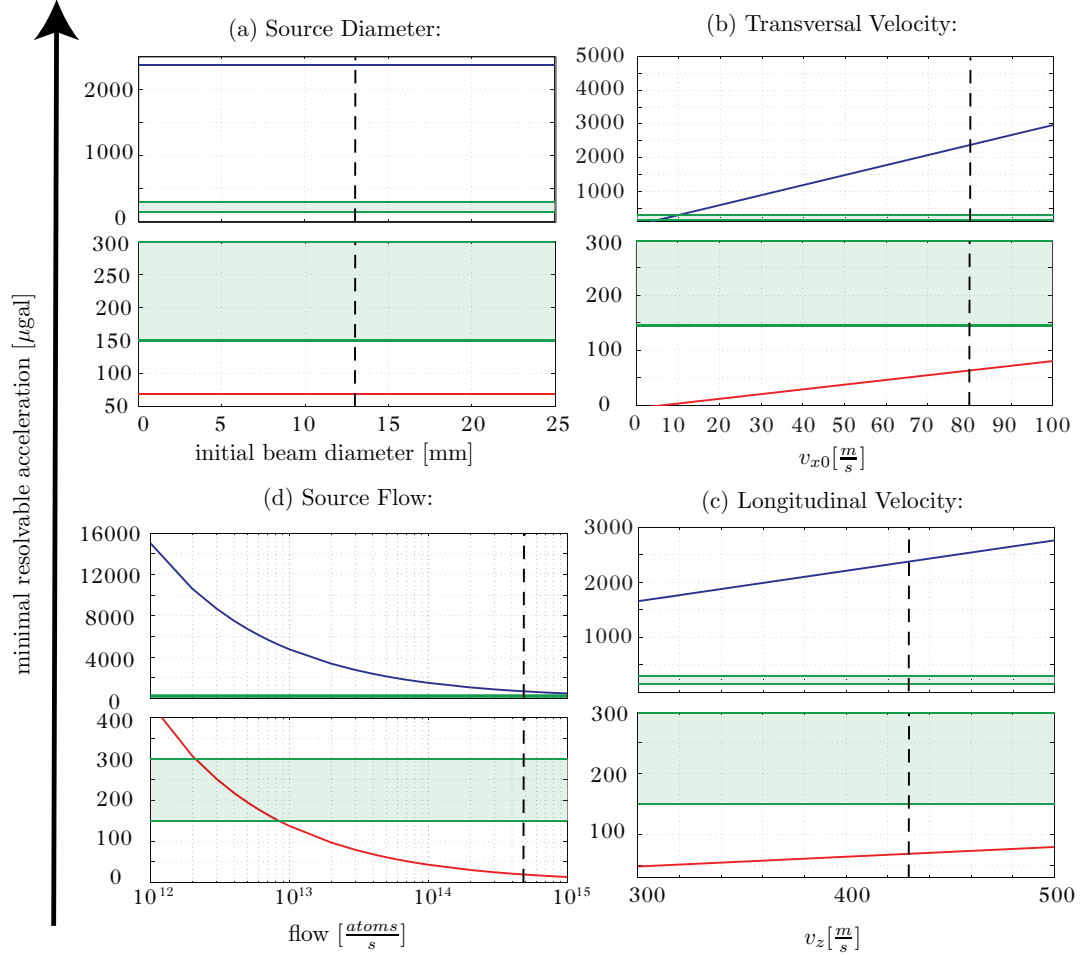
Figure 2.9: The minimal resolvable gravitational acceleration $g_{\min}$ dependent on source parameters for the Ar*-experiment in Heidelberg. The blue (red) lines in the upper (lower) plots are $g_{\min}$-values of data retrieved from $1\,\mathrm{s}$ ($20\,\mathrm{min}$) of measurement. The range of the periodic g-variation, that is induced by the moon's gravitation, is shaded green. In order to resolve this tidal effect, $g_{\min}$ needs to lie under this green bar. The dashed vertical lines indicate the current values of the experiment. An overview of them is given in table 2.1.

very small improvement can be expected when further increasing L.

To sum up, the parameters of the Ar*-experiment are given in table 2.1 and yield
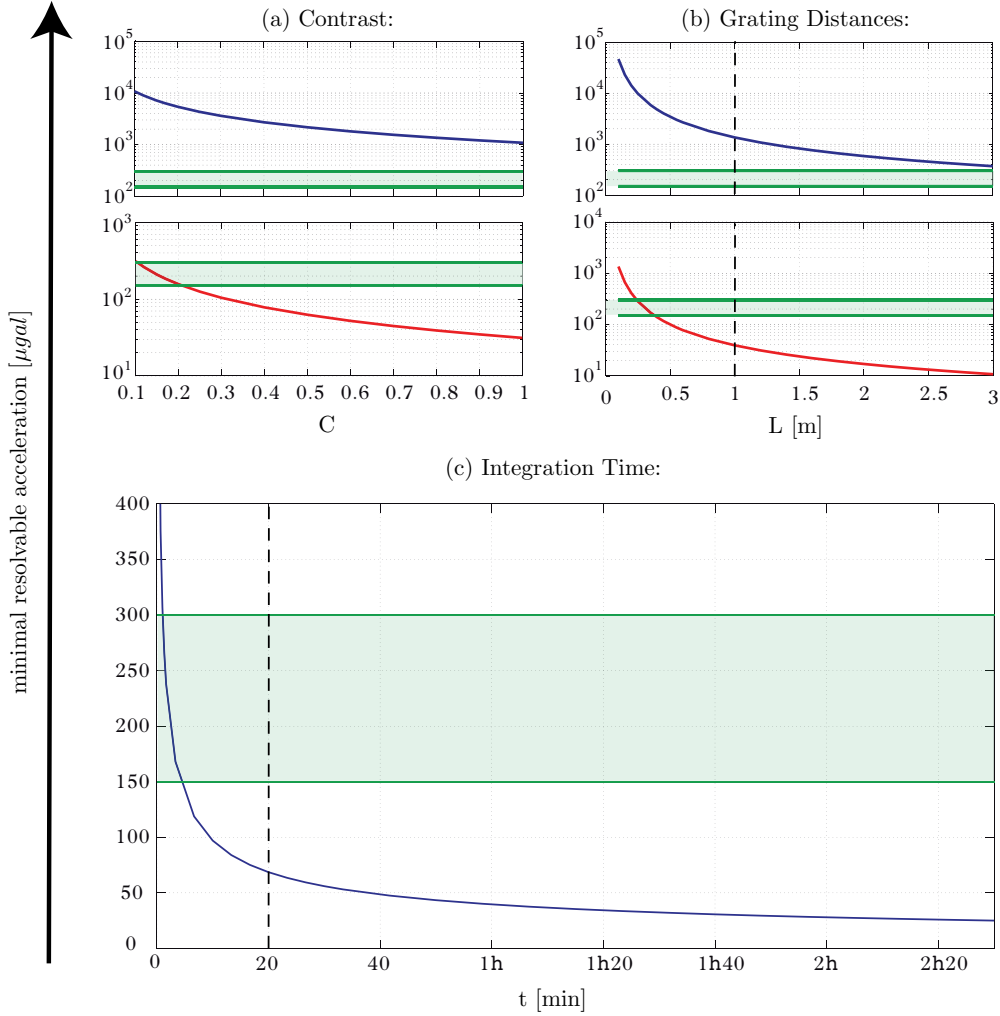
Figure 2.10: The minimal resolvable gravitational acceleration $g_{\min}$ dependent on geometrical and measurement parameters for the Ar*-experiment in Heidelberg. The blue (red) lines in the upper (lower) plots are $g_{\min}$-values of data retrieved from 1 s (20 min) of measurement. The range of the periodic g-variation, that is induced by the moon's gravitation, is shaded green. In order to resolve this tidal effect, $g_{\min}$ needs to lie under this green bar. The dashed vertical lines indicate the current values of the experiment. An overview of them is given in table 2.1.

a minimal resolvable acceleration of $g_{\min} \approx 2.4$ mgal for 1 s and[1]

$$g_{\min} \approx 68\,\mu\text{gal}, \tag{2.43}$$

---

[1]Note for the these considerations the unit for small accelerations $1\,\text{gal} = 0.01\,\frac{\text{m}}{\text{s}^2}$.

for 20 min of integration. This can be decreased even further by integrating longer as it is shown in figure 2.10(c). However, note that 20 min remains a good choice as the gain of longer integration times drops quickly.

Although the reachable value for g_{min} cannot compete with today's most precise gravimeters [18, 20], it is small enough to measure the influence of the moon on the earth's gravitation and opens a promising possibility to test the equivalence principle with the Moiré-deflectometer for a large variety of different sorts of matter or even for antimatter. As the production of antimatter is still a challenging procedure, the value of equation 2.43 has to be reevaluated with the experimental conditions for antimatter experiments. This is done in the following paragraph for the antihydrogen production of the AE$\overline{g}$IS-experiment at CERN.

g_{min} of the $\overline{H}$-experiment

Estimating g_{min} for the $\overline{H}$-experiment at CERN depends on the experimental conditions in the same manner as in the case of the the Ar*-experiment in Heidelberg. But according to the source performance of the $\overline{H}$-production, the reachable $g_{min}(\overline{H})$ is by several orders of magnitude larger than $g_{min}(Ar)$. It turns out that a longer time integration is necessary to approach the desired sensitivity for the gravity measurement with 1% precision. Due to this, the dependencies on the experimental parameters presented in this paragraph are directly given for a data set, that is retrieved after 6 h of integration. This integration time corresponds to the interval per day, during which antiprotons are accessible for the AE$\overline{g}$IS-group.

Concerning the antihydrogen production, figure 2.11 provides the most important dependencies. The dashed lines indicate the predicted values for the corresponding parameters, whereas the solid green lines denote the limit for $g_{min}(\overline{H}) < 1\% \cdot g \approx 0.1 \frac{m}{s^2}$. With its logarithmic scale, figure 2.11(a) demonstrates the particular importance of the initial temperature of the antihydrogen which is expected to be around 100 mK. Besides this, it is the absolute flow as one of the major differences between the two experiments at CERN and in Heidelberg, that has a huge impact on g_{min}. This is shown in figure 2.11(b) with a predicted production rate of 1 Hz. For the integration of one day, both parameters are good enough for the planned gravitation measurement. Nevertheless, there are some parameters contributing to these estimations, which are
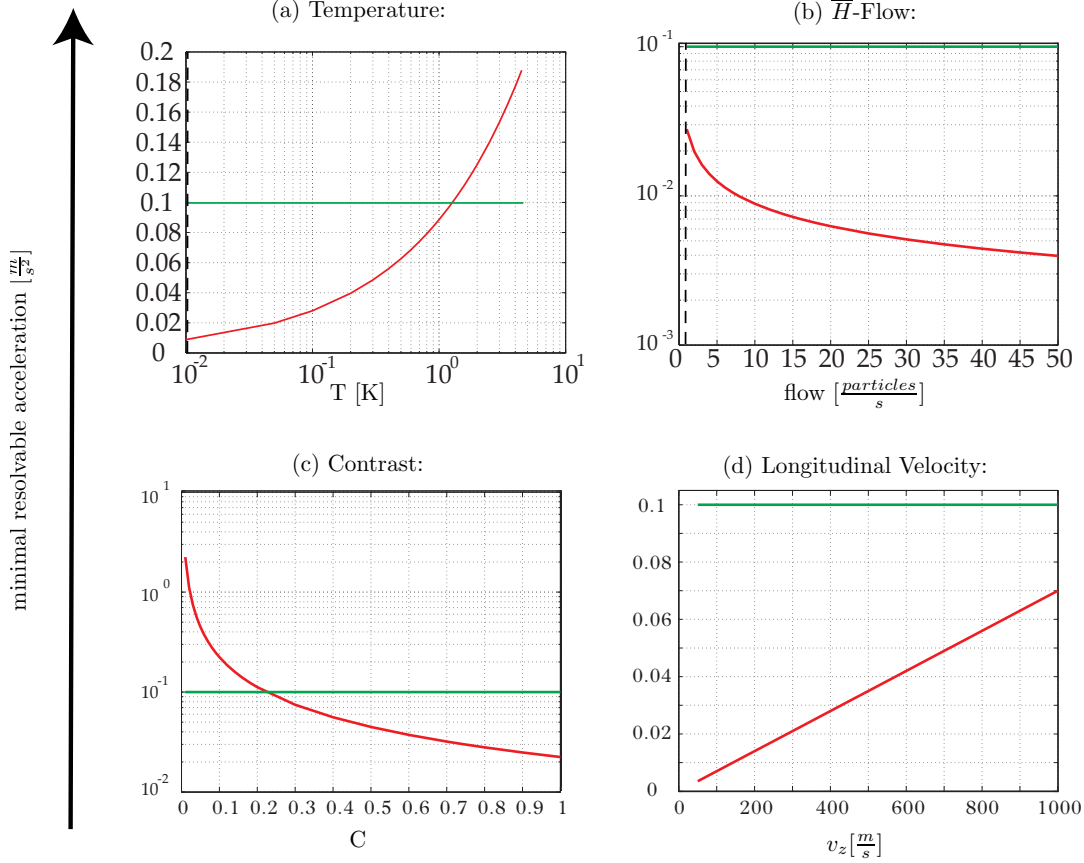
Figure 2.11: The minimal resolvable gravitational acceleration $g_{\min}$ dependent on some experimental parameters for 1 day of integration time of the $\overline{\overline{\text{H}}}$-experiment at CERN ($L = 1\,\text{m}$). The green lines indicate $0.1\,\frac{\text{m}}{\text{s}^2}$, which corresponds to 1% of g. In order to resolve this limit, $g_{\min}$ needs to lie below this limit. The dashed vertical lines indicate the currently predicted values of the experiment. They are $100\,\text{mK}$, $1\,\frac{\text{atom}}{\text{s}}$ and $400\,\frac{\text{m}}{\text{s}}$ for the temperature, the particle flow and the longitudinal velocity, respectively. The contrast is assumed to be 0.8.

either only very rough estimates or even totally unknown so far. One particular example is the contrast C, which has been assumed to be the ideal $C = 0.8$. Figure 2.11(c) provides the dependence on the contrast of the shadow pattern and yields – as in the case of the Ar*-experiment – a value of about $C \approx 0.4 - 0.5$, that should be approached for the aimed precision of the measurement.

Regarding the influence of the longitudinal velocity of the $\overline{\overline{\text{H}}}$-measurement in figure 2.11(d), we have to remember an important difference to the measurement in Heidel-
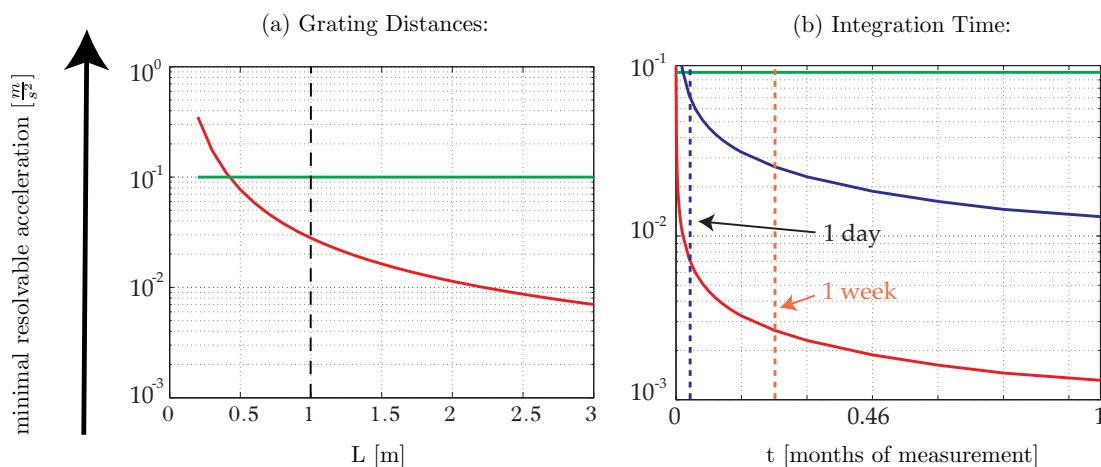
Figure 2.12: The minimal resolvable gravitational acceleration $g_{\min}$ dependent on the grating distance L and the integration time t measured in months of measurement. Other experimental parameters are chosen as in figure 2.11.

berg. The $\overline{\text{H}}$-experiment is based on time of flight (TOF) measurements. For this purpose, the time, the particles need for their flight through the deflectometer, is going to be measured and thus, their vertical deflection due to gravity can be recorded as a function of the time, during which the particles had been exposed to gravity. Nevertheless, figure 2.11(d) demonstrates that with the currently predicted parameters and one day of integration, even the fastest particles can reach the desired $g_{\min}$.

Noticing the logarithmic scale in figure 2.12(a), we see that an increase of the inter-grating distance L will not have a huge effect beyond the currently planned value of $1\,\text{m}$.

The most important, experimentally adjustable parameter remains the integration time. Figure 2.12(b) shows the dependence for the two extreme TOF measurements, i. e. the fastest particles with $v_z = 1000\,\frac{\text{m}}{\text{s}}$ and the slowest with $v_z = 100\,\frac{\text{m}}{\text{s}}$ are drawn with the blue and red curve, respectively. Thus, other particles being some hundreds of meters per second fast will lie in between these two curves. The purple and the orange dotted lines denote an integration of one day and one week, respectively. This shows that – even with some possible corrections of the predicted parameters – a measurement of a couple of months will definitely provide the necessary sensitivity of the Moiré-deflectometer in order to achieve a gravitational measurement of 1% precision.

Chapter 3

Sensitivity Analysis of a Moiré-Deflectometer on External Fields

3.1 Introduction

Although AE$\overline{\text{g}}$IS aims to investigates the electrically neutral antihydrogen, there are still disturbing effects that can be caused by external magnetic or electric fields. These disturbances originate from the *Zeeman-* and the *Stark-effect* in the case of external magnetic and electric fields, respectively. Hence, such external fields make it difficult to ensure that a measurement of the deflectometer exclusively examines the effect of gravitation and not of the interaction with the mentioned fields.
This issue can be solved by using one of the pecularities of gravitation: In contrast to magnetic and electric fields, gravitation cannot be shielded. Therefore, the simpliest solution for an unperturbed gravitational measurement can be realised by shielding any of these disturbing fields. In order to design an appropriate shielding, a sensitivity analysis on these fields is necessary for both experimental setups in Heidelberg and at CERN.

The following chapter provides such a sensitivity analysis. After examining the effect of any kind of accelerating fields existing in the two major regions (between the $1^{\text{st}}/2^{\text{nd}}$ and behind the 2nd grating) of such a deflectometer, we distinguish between magnetic and electric fields and provide the corresponding sensitivity analysis. For this

purpose, we need to further distinguish between the experiments with metastable argon in Heidelberg and the ones with Rydberg-antihydrogen at CERN, as the different internal atomic structure can lead to different atom-field-interactions. This differentiation yields first estimates for the field strengths and configurations that can decrease the contrast of the deflectometer's fringe pattern fundamentally.

In addition to the sensitiviy analysis, we consider the feasability of a method, to which we refer to in the following as *Bias-Reduced-Gradient-Susceptibility* (BRGS). This method uses offset magnetic fields to reduce the dependence on a gradient in a specific direction.

3.2 Additional Forces in a Moiré-Deflectometer

Analog to the derivation in section 2.5.2, we can derive the effect of a general additional external force. Introducing such a force with an acceleration a_{ext} modifies equation 2.27 to

$$x(T_{\text{pre}} + T_1 + T_2) = \underbrace{-\frac{T_2}{T_1} x_{G1} + \left(1 + \frac{T_2}{T_1}\right) x_{G2}}_{\text{without external forces}} \tag{3.1}$$

$$\underbrace{-\frac{1}{2} g \left(T_1 T_2 + T_2^2\right)}_{\Delta x_g} \underbrace{-\frac{1}{2} a_{\text{ext}} \left(T_1 T_2 + T_2^2\right)}_{\Delta x_{\text{ext}}}, \tag{3.2}$$

where the terms Δx_g and Δx_{ext} describe the deflections that are induced by the gravitational and any other accelerating force, respectively. Concerning the two major regions of a deflectometer, this last term can be seperated into

$$|\Delta x_{\text{ext}}| = \underbrace{\frac{1}{2} a_{\text{ext}} T_1 T_2}_{\text{between the 1st and 2nd grating}} + \underbrace{\frac{1}{2} a_{\text{ext}} T_2^2}_{\text{behind the 2nd grating}} . \tag{3.3}$$

With an overall length of the deflectometer of up to $2\,\text{m}$ and longer, an examination of disturbing forces acting along different regions of the apparatus becomes particularly interesting.

First of all, the independence from an external force before the two gratings, i. e. during T_{pre}, shall be stressed at this point.[1]

---

[1] Note that the possible particle loss during T_{pre}, which can occur due to a large divergence of the beam, is neglected here, as it can easily be included by a reduced particle flow of the source.

Furthermore, for a setup with $T_1 = T_2 = T$ equation 3.3 demonstrates that for the effect of an exteral force, we do not need to distinguish, whether this force exists either only between the two gratings or only behind the 2nd one. In both of these major regions, an accelerating external force has the same effect on the Moiré-pattern. Thus, the same degree of shielding is necessary along the entire deflectometer.

For an estimation of the required shielding degree, we look for critical field values by examining the strongest possible effect of a small field. Hence, in the following analysis, we assume this field to be present along the whole deflectometer.

3.3 Magnetic Field

Concerning a disturbing magnetic field, the particle-field interaction can most generally be determined by considering an atomic sample flying through the apparatus as a 'bunch of small magnetic moments' that are not interacting with each other. The force, that such a magnetic moment experiences in a magnetic field can be evaluated via [51]

$$\mathbf{F}_{\text{mag}}(\mathbf{r}) = -\nabla E_{\text{mag}}(\mathbf{r}), \tag{3.4}$$

where the interaction energy $E_{\text{mag}}(\mathbf{r})$ of the atom's magnetic moment $\boldsymbol{\mu}_{\text{atom}}$ with the external field $\mathbf{B}$ is given by

$$E_{\text{mag}}(\mathbf{r}) = -\boldsymbol{\mu}_{\text{atom}} \cdot \mathbf{B}(\mathbf{r}). \tag{3.5}$$

To evaluate $\boldsymbol{\mu}_{\text{atom}}$ we need to consider the internal structure of the particles in detail. Hence, at this point a differentiation between the two cases of the argon-experiment in Heidelberg and the one with antihydrogen at CERN is required.

3.3.1 External B-Field and the Argon Measurement

As ^{40}Ar with a relative abundance of 99.6% is predominant in the atomic samples used for the Moiré-deflectometer tests in Heidelberg, it is absolutely sufficient to examine this isotope. Concerning any interactions with an external magnetic field, this isotope with a ground state electron configuration given by $1s^2 2s^2 2p^6 3s^2 3p^6 = [\text{Ne}]3s^2 3p^6$ has an important pecularity[1]: Due to its so-called even-even nucleus consisting of 18 protons, 22 neutrons, it does not have a nuclear moment $\mathbf{I}$. Consequently, there is no hyperfine

---

[1]More details about argon can be found in Appendix B.2.

3. SENSITIVITY ANALYSIS OF A MOIRÉ-DEFLECTOMETER ON EXTERNAL FIELDS

splitting and the coupling to an external magnetic field is covered entirely by the coupling of the atom's angular moment $\mathbf{J}$.

In order to determine the argon's angular moment $\mathbf{J}$, we need to account for the peculiarity of argon as a novel gas with only closed shells in its ground state[1]. For the lowest electronic excitation of the atom, one of the outer $3p$-electrons needs to be excited to a higher shell. Due to the closed shells, a large excitation energy is necessary to reach the lowest electronic excitation ($\sim 11.5\,\mathrm{eV}$). Hence, the interaction between the excited electron and the electrons of the ionic leftover, to which we will refer in the following as the *atomic core*, is rather weak. Consequently, the common LS-coupling does only occur within the core and we can calculate its angular moment $\mathbf{J}_c$ by

$$\mathbf{J}_c = \sum_i \mathbf{l}_i + \sum_i \mathbf{s}_i = \mathbf{L_c} + \mathbf{S_c} = \begin{cases} \frac{1}{2} \\ \frac{3}{2} \end{cases}, \tag{3.6}$$

where only the core's electron spins $\mathbf{s}_i$ and their angular momenta $\mathbf{l}_i$ contribute. The angular moment $\mathbf{l}_e$ of the excited electron can then couple to $\mathbf{J}_c$ and yield the angular moment of the atom of

$$\mathbf{K} = \mathbf{J}_c + \mathbf{l}_e. \tag{3.7}$$

Finally, this $\mathbf{K}$ couples to the spin $\mathbf{s}_e$ of the excited electron, which leads then to the atom's total angular moment

$$\mathbf{J} = \mathbf{K} + \mathbf{s}_e. \tag{3.8}$$

The described Racah-coupling leads to a level scheme given in figure 3.1. Here, the states are described by the Paschen-notation, where the internal energy levels are defined by $(n_e-3)l_k(J)$, with n_e representing the principle quantum number of the excited electron, $l = |\mathbf{l}_e|$ its angular quantum number, and the index k labels the states with the same quantum numbers as shown in figure 3.1.

For detection purposes, which are described in further details in section 5.3, we prepare the argon atoms in their metastable state $1s_5(J=2)$.[2] To analyse the atom-field-interaction of this state with $J = 2$, we need M_J, the projection of the atoms

---

[1]More details on the *Racah-Coupling* of argon and other novel gases can be found in [52, 53, 54].

[2]Even though our plasma source (see section 5.2.3) produces some of the atoms in the other metastable state, $1s_3(J = 0)$, they can be neglected for the magnetic sensitivity analysis. They have no magnetic moment for the external field to interact with.
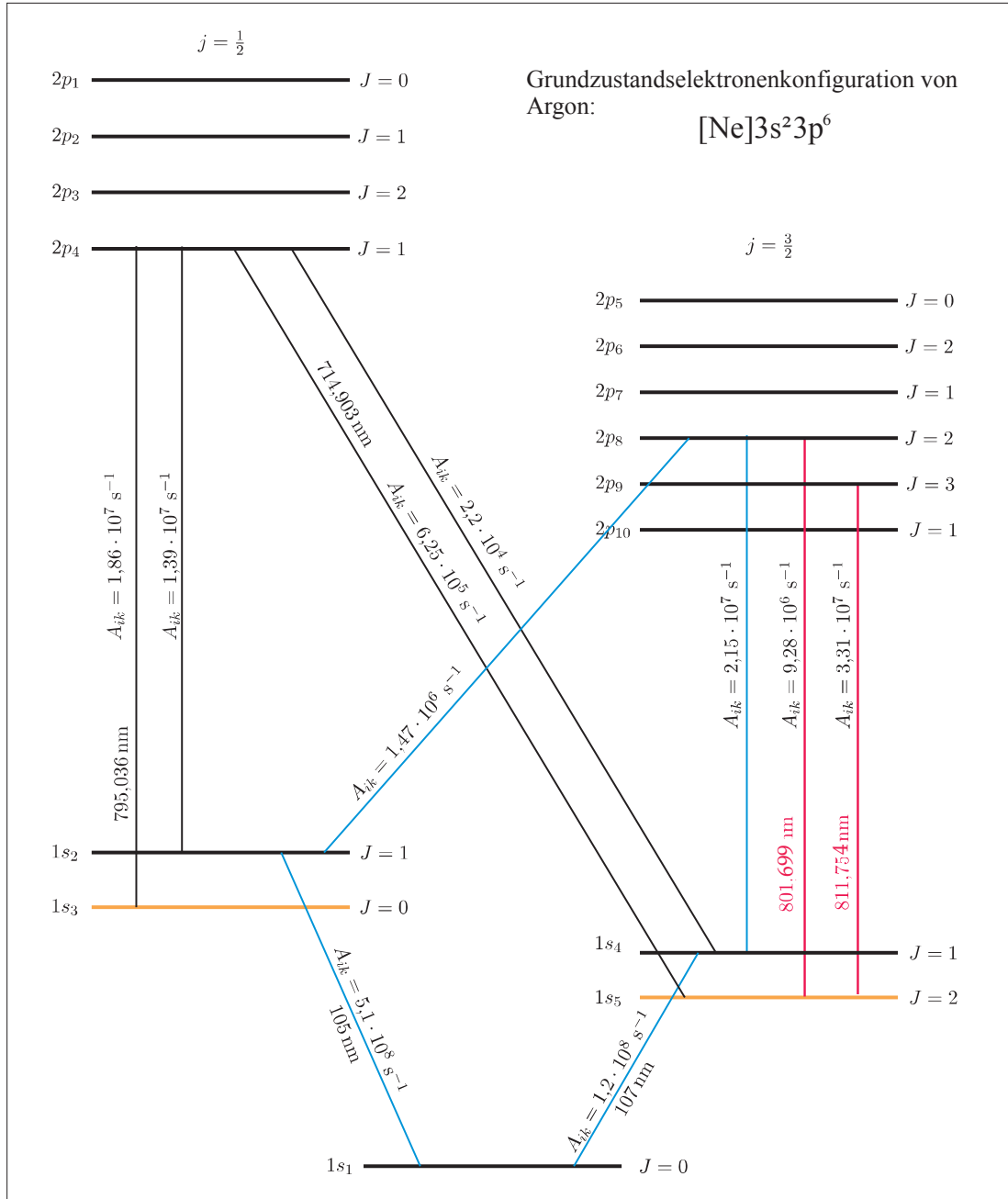
Figure 3.1: The ^{40}Ar level scheme. Note the quantum numbers of the Racah-coupling. This figure is taken from [53].

total angular moment **J** on the magnetic field axis. Assuming a small magnetic field, i. e. the induced Zeeman-energy-shifts needs to remain small compared to the internal

3. SENSITIVITY ANALYSIS OF A MOIRÉ-DEFLECTOMETER ON EXTERNAL FIELDS

energy splittings of the atom, we can treat the atom-field interaction as perturbation of the atom's Hamiltonian.[1] This provides the Zeeman-energy-shift E_{mag} that a magnetic field $B(x)$ induces on an atom[2] with M_J and is given by [54, 55]

$$E_{\text{mag},M_J}(x) = g_J \mu_B M_J B(x), \tag{3.9}$$

where μ_B denotes the Bohr magneton and g_J the Landé g-factor that is given with the other atomic properties of argon in Appendix B.2. Thus, the force that is exerted on an atom due to to the magnetic field reads [54, 55]

$$F_{\text{mag},M_J}(x) = -\frac{dE_{\text{mag},M_J}(x)}{dx} = -g_J \mu_B M_J \frac{dB}{dx} \tag{3.10}$$

and the magnitude of the corresponding acceleration, that this force exerts on a mass m is given by

$$|a_{\text{mag}}| = \left| \frac{g_J \mu_B M_J}{m} \frac{dB}{dx} \right|. \tag{3.11}$$

In order to estimate the strength of a magnetic field gradient $\left| \left(\frac{dB}{dx} \right)_{\text{crit}} \right|$, which disturbs a measurement of the gravitational force $F_{\text{grav}}(x)$, we first need to identify the magnetically most sensitive states. With equation 3.10, they are given by the ones with the largest $|g_J M_J|$. Hence, the most sensitive states are the so-called *stretched states* with $M_J = \pm 2$. They provide a first measure for the critical gradient that can be estimated via

$$F_{\text{mag},M_J=\pm 2}(x) \approx F_{\text{grav}}(x) \tag{3.12}$$

$$\Rightarrow \left| \left(\frac{dB}{dx} \right)_{\text{crit}} \right| \approx 2.3 \, \frac{\text{G}}{\text{cm}}. \tag{3.13}$$

However, measuring $F_{\text{grav}}(x)$ with a Moiré-deflectometer is more sensitive on disturbing field gradients and the critical value of equation 3.13 needs to be adjusted. Regarding, for instance, a deflectometer-setup with $1\,\text{m}$ distance between the gratings, we find a spatial shift of the fringe pattern due to gravity that is larger than one grating period d. In this case, smaller gradients than the one of equation 3.13 will already lead

---

[1] The explicit calculation of this perturbation can be found in every common textbook on Quantum Mechanics, e. g. [54, 55].

[2] The following considerations are restricted on the x-direction, the one gravitation is actually acting. The more general three dimensional case with $\mathbf{B}(\mathbf{r})$ is further examined in section 3.3.3.

to a fundamental loss of the visibility of the Moiré-deflectometer's characteristic fringe pattern. Actually, as soon as atoms with $M_J = \pm 2, \pm 1$ become deflected in the vertical direction, the fringe pattern at the end of the deflectometer is adulterated. Hence, the contrast of the pattern of all particles changes depending on the relative populations of the different magnetic sub-states $M_J = 0, \pm 1, \pm 2$ and the amount of additional deflection due to magnetic fields.

Assuming all sub-states to be equally populated, we can expect a fundamental loss of contrast when the magnetically most sensitive atoms with $M_J = \pm 2$ are deflected by half of the grating period d. This value can be determined with equations 3.3 and 3.11. We find

$$|\Delta x_{\text{ext},M_J=\pm 2}| \overset{!}{=} \frac{1}{2}d \tag{3.14}$$

$$\Rightarrow \left| \left(\frac{dB}{dx} \right)_{\frac{1}{2}d} \right| \approx 880 \, \frac{\text{mG}}{\text{cm}}, \tag{3.15}$$

where we evaluated the absolute magnitude of the gradient and hence, account for the fact, that there is no difference whether the magnetic field points upwards or downwards.

Figure 3.2 shows simulation results for this particular case in detail. These simulations are done for the setup in Heidelberg with $L_1 = L_2 = 1\,\text{m}$ and the atoms' vertical and horizontal velocity components $\overline{v}_x = 80 \, \frac{\text{m}}{\text{s}}$ and $\overline{v}_z = 430 \, \frac{\text{m}}{\text{s}}$, respectively[1]. In the upper five subfigures the fringe patterns of the four central periods right before the third grating are shown. The expected shift of the $(M_J = \pm 2)$-states is visible by comparing the fringe patterns. Note the grey background in each subfigure, which shows the patterns without any magnetic atom-field-interaction. An equal relative population of the magnetic substates yields a total fringe pattern given by the 'Total Pattern'. Besides the expected shift of the stretched states of $\frac{1}{2}d$, this illustration demonstrates in particular, how the huge loss of contrast in the total fringe pattern can occur by an external magnetic field gradient.

Scanning over the total pattern with the third grating produces then a signal that is

---

[1]In the following simulations, the vertical velocity components are assumed to be normally distributed around the given value, which has been chosen due to a former setup [56]. For this sensitivity analysis, the longitudinal component has been used as discrete value. The effect of longitudinal distributions is examined in chapter 5.
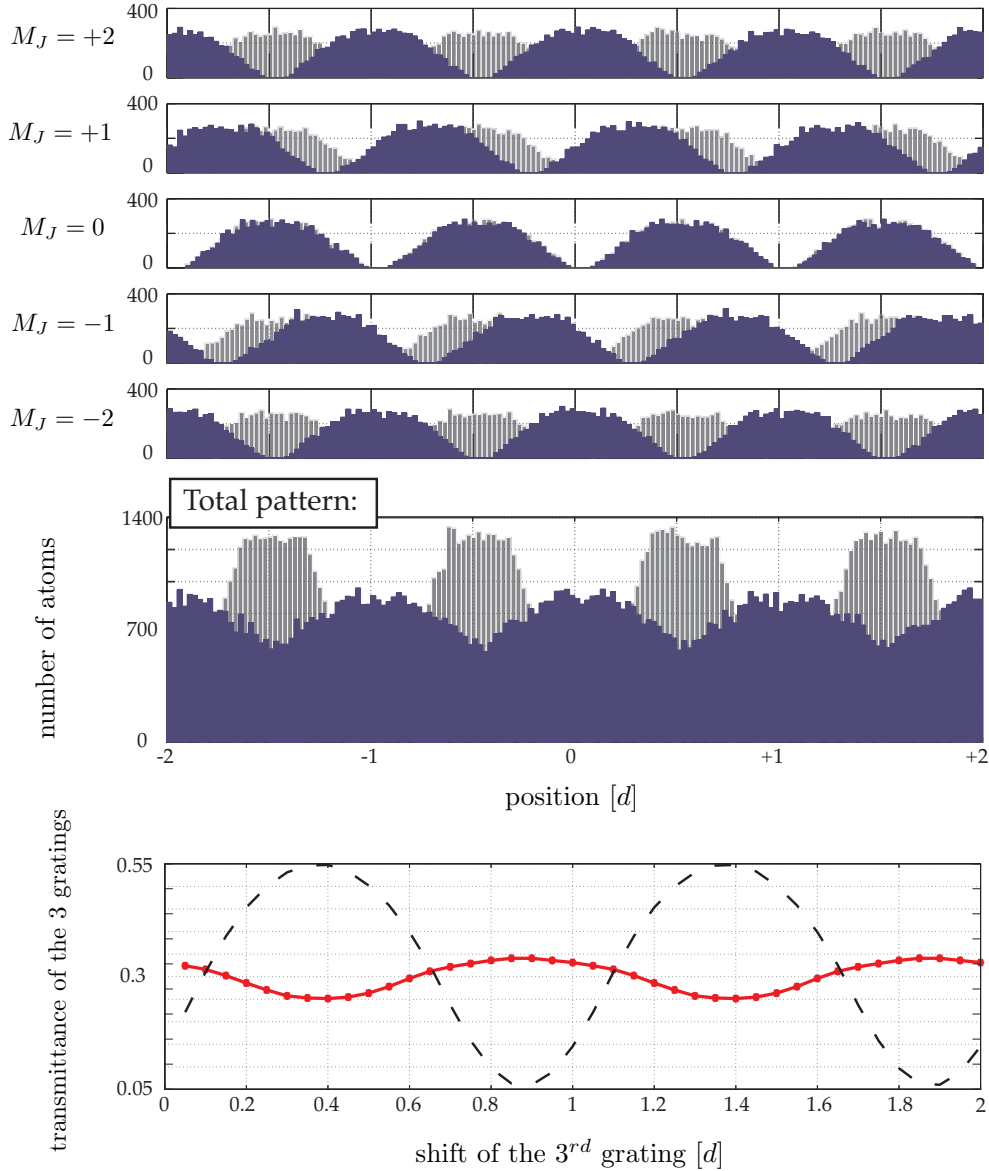
Figure 3.2: The shift of the different magnetic substates M_J with the additional magnetic field gradient $\frac{dB}{dx} \approx 880 \frac{\text{mG}}{\text{cm}}$. These are results of a Monte-Carlo simulation for the experimental setup in Heidelberg and with an input of 10^9 atoms per magnetic substate. The grey background and the dashed lines indicate the result without any magnetic gradient.

plotted at the bottom of figure 3.2. The solid, red line is the signal including the magnetic field gradient. It emphasizes the loss of contrast as compared to the one without gradient drawn with the dashed line. Nevertheless, the contrast in figure 3.2 decreases

only down to 0.2 and does not diminish entirely as might have been expected. This can be explained by considering the creation of the total fringe pattern right before the 3$^{\text{rd}}$ grating: The sum over all magnetic substates provides new maxima, which consist of the maxima of the $(M_J = \pm 2)$-states, but also of the tails of the smeared out top-hat functions of the other substates. Thus, it is the combination of the smearing out of the top-hat functions and the number of substates that leads to the persisting value of the contrast.
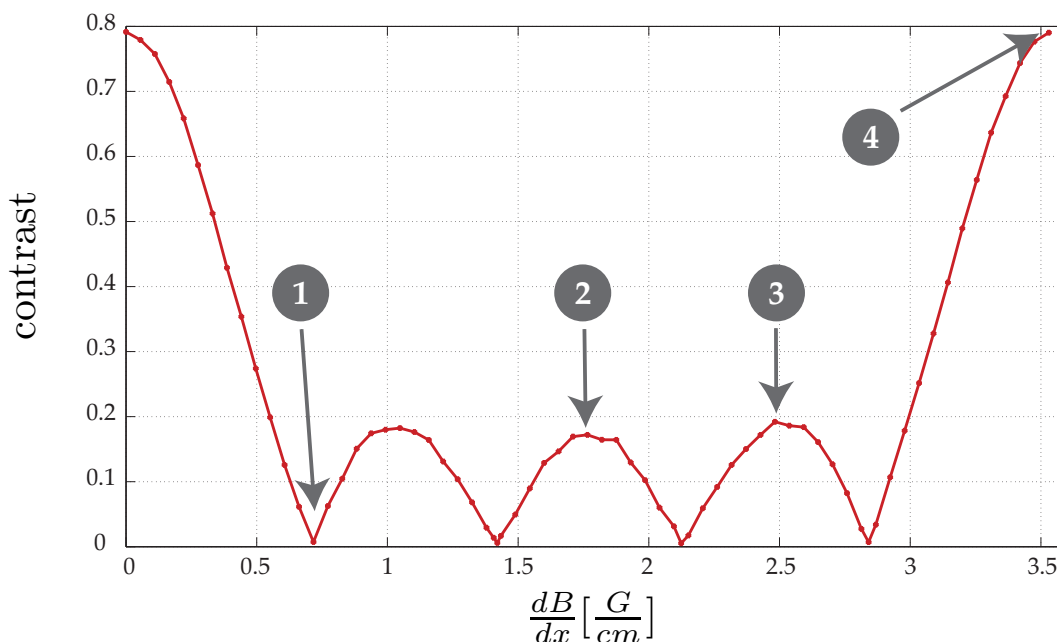
Figure 3.3: The change of contrast dependent on the external magnetic field gradient $\frac{dB}{dx}$. The encircled numbers refer to the detailed plots in figure 3.4 and 3.5.

Figure 3.3 shows the dependence of the contrast on an increasing magnetic field gradient along the entire deflectometer. The contrast of the used three-grating setup has a distinct local minimum < 0.01 at a gradient of $\sim 720\,\frac{\text{mG}}{\text{cm}}$. This minimum is plotted in detail in figure 3.4(a). The summation over all magnetic substates in the total pattern shows that the smeared out top-hat functions of the substates' patterns can indeed cause a total extinction of the periodic pattern. But the gradient, where this occurs, differs slightly from the $\left(\frac{dB}{dx}\right)_{\frac{1}{2}d}$ of equation 3.15.

Increasing the magnetic field gradient as in figure 3.3 leads to a periodic reoccurence of
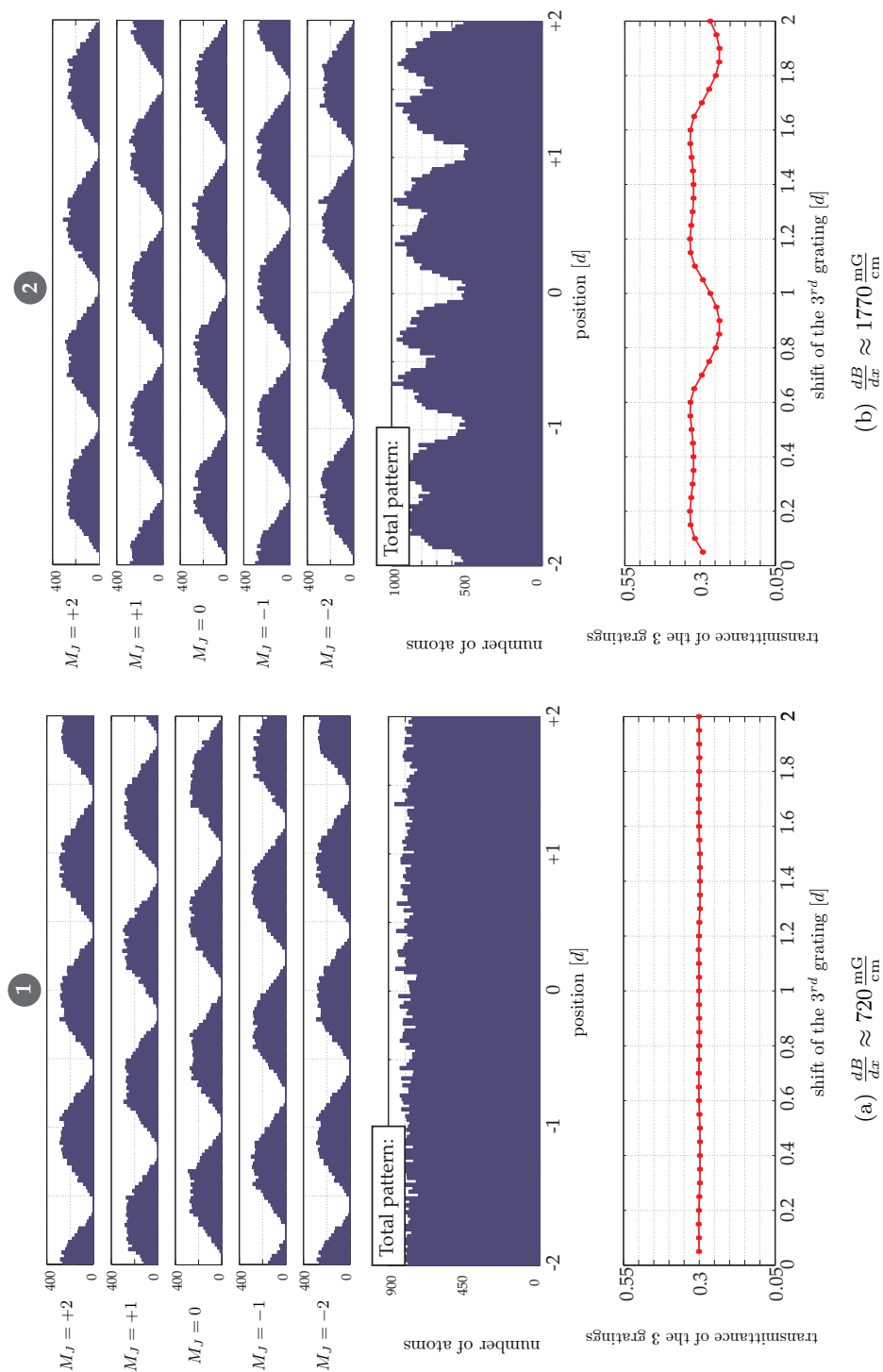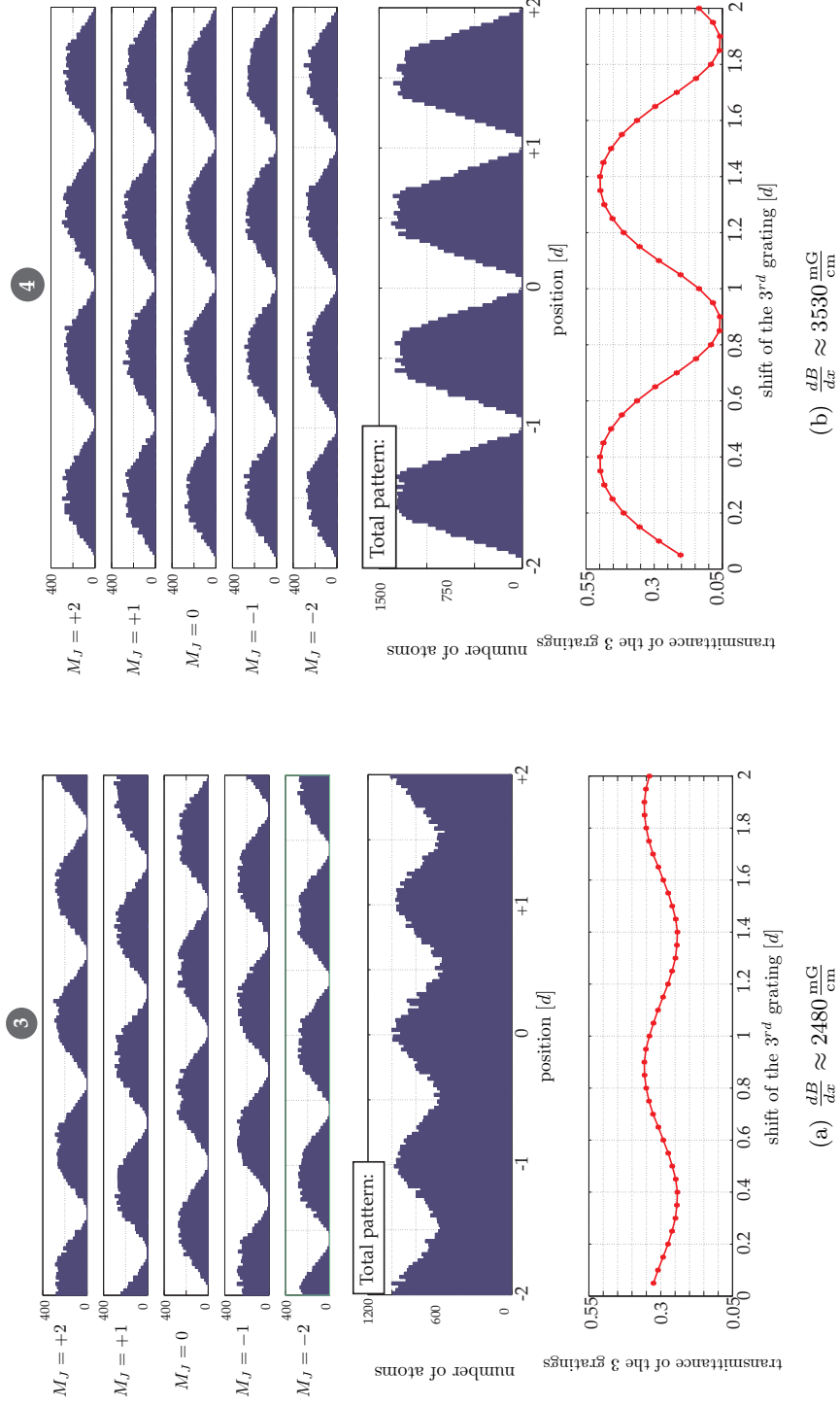
Figure 3.4: Exemplary results of Monte-Carlo simulations of the output of the Moiré-deflectometer with an additional magnetic field gradient along the whole deflectometer. 10^9 atoms have been used for the simulation of each magnetic substate M_J. The total patterns are plotted just before the 3rd grating and the plots below them show the transmission behind the scanned 3rd grating. The encircled numbers refer to the corresponding data in figure 3.3.

Figure 3.5: Exemplary results of Monte-Carlo simulations of the output of the Moiré-deflectometer with an additional magnetic field gradient along the whole deflectometer. 10^9 atoms have been used for the simulation of each magnetic substate M_J. The total patterns are plotted just before the 3rd grating and the plots below them show the transmission behind the scanned 3rd grating. The encircled numbers refer to the corresponding data in figure 3.3.

local minima and maxima. They result from the different shifts of the fringe patterns of the different M_J-states. As a consequence, the total pattern becomes adulterated. Particular examples for this adulteration are shown in subfigures 3.4(b) and 3.5(a) for field gradients of 1770 $\frac{\text{mG}}{\text{cm}}$ and 2480 $\frac{\text{mG}}{\text{cm}}$, respectively.

The extreme case of the gradient 3530 $\frac{\text{mG}}{\text{cm}}$ in subfigure 3.5(b), when the ($M_J = \pm 2$)- and the ($M_J = \pm 1$)-states are shifted by $2d$ and $1d$, respectively, demonstrates the possibility to reach the same contrast as without external gradient. However, we need to avoid this situation: As soon as the field gradient varies, the measurement will still be disturbed in an uncontrollable way.

Particularly important for the experimental setup remains the smallest field gradient that leads to a contrast of below 0.5. As shown in section 2.7.2 (figure 2.10) this is still an acceptable value for the gravitational measurement in Heidelberg. Hence, following the simulation results presented in figure 3.3, we need to avoid a magnetic field gradient of $c_B(\text{Ar}) \approx 330 \frac{\text{mG}}{\text{cm}}$, which provides a good indication for the degree of magnetic shielding that might become necessary.

3.3.2 External B-Field and the Antihydrogen Measurement

Concerning the effect of a magnetic field gradient on the measurements with antihydrogen, we need to consider the internal structure of hydrogen. Contrary to stable argon isotopes, hydrogen has a nuclear moment **I**, the one of its proton. This moment couples to the electron's total angular moment **J** such that generally, the quantum numbers, which govern the behaviour of the atom in an external magnetic field, are given by $F = |\mathbf{F}| = |\mathbf{I} + \mathbf{J}|$, with the total angular moment **F**, and M_F, the projection of **F** on the external field axis.

The magnetic force acting on an atom with hyperfine structure can be found analog to equation 3.10; it reads [51]

$$F_{\text{mag},M_F}(x) = -g_F \mu_B M_F \frac{dB}{dx}, \tag{3.16}$$

where the Landé g-factor g_F is given by

$$g_F = \frac{F(F+1) + J(J+1) - I(I+1)}{2F(F+1)} g_J. \tag{3.17}$$

As for argon, equations 3.16 and 3.17 identify the 'streched states' as the important ones for our sensitivity analysis[1].

The atom's hyperfine splitting requires a careful study of the particular case of highly excited Rydberg atoms, as the antihydrogen in the AE$\overline{\text{g}}$IS-experiment will be produced in such a highly excited state. For this study, we remember that for hydrogen, the energy splittings between adjacent energy levels decrease very quickly with an increasing principle quantum number n [57]. Thus, the higher the excited state, the closer are adjacent energy levels. The same holds for the spacing of the corresponding manifolds of hyperfine states. Their energy splitting ΔE_{HFS} can be determined via [58]

$$\Delta E_{\text{HFS}}(n, L, J, I, F) = \frac{1}{2} \frac{hcR_\infty \alpha^2 Z^3}{n^3 L J^2} \frac{m_e}{m_p} g_I \left(F(F+1) - I(I+1) - J(J+1)\right) \quad (3.18)$$

with the Rydberg constant R_∞, the fine structure constant α, the atomic number $Z = 1$ for hydrogen and the nuclear g-factor g_I, which is reduced by the mass ratio $\frac{m_e}{m_p}$ of the mass of the electron m_e and the proton m_p. For instance, for Rydberg hydrogen atoms with $n = 25, L = 24, J = 24.5, I = 0.5$, this energy splitting is just $\sim 73\,\text{Hz} \cdot h$.

Due to this small splitting, we need to make sure, that the magnetic field, that we apply, does not induce an energy shift that is bigger than the hyperfine splitting. Thus, we estimate the induced Zeeman-energy, that the most sensitive atoms aquire during a small drift of only $1\,\text{cm}$ through a magnetic gradient, that is strong enough to shift their Moiré-pattern by half a grating period. With the analogon for the hyperfine structure of equation 3.11, this gradient is given by $0.14\,\frac{\text{mG}}{\text{cm}}$. Hence, the atoms gain during this short drift a Zeeman-energy of

$$\triangle E_{\text{mag},M_F}(x) = \mu_B g_F M_F \frac{dB}{dx} \triangle x \approx 5\,\text{kHz} \cdot h. \quad (3.19)$$

Compared to the hyperfine splitting of $\sim 73\,\text{Hz} \cdot h$, we cannot assume F and M_F to remain good quantum numbers along the atom's entire flight through the deflectometer. In order to determine the difference between the two regimes of F and M_F or J and M_J as the good quantum numbers we summarised the interaction for the stretched states in

---

[1]Note that in the following consideratons, we used as the most sensitive atoms always the ones with $v_z = 100\,\frac{\text{m}}{\text{s}}$ as the disturbing field will have the strongest effect on the slowest atoms.

3. SENSITIVITY ANALYSIS OF A MOIRÉ-DEFLECTOMETER ON EXTERNAL FIELDS

$n = 25$	fine structure	hyperfine structure
quantum numbers	L, S, J, M_J	J, I, F, M_F
stretched states	$L = 24, s = 0.5, J = 24.5,$	$J = 24.5, I = 0.5, F = 25$
	$M_J = 24.5$	$M_F = 25$
interaction with $B(x)$	$E_{\mathrm{mag},M_J}(x) = g_J \mu_B M_J B(x)$	$E_{\mathrm{mag},M_F}(x) = g_F \mu_B M_F B(x)$
$g_{...}$	$g_J \approx 1.00$	$g_F \approx 0.98$
$M_{...}$	$M_J = 24.5$	$M_F = 25$

Table 3.1: Fine and hyperfine structure of the stretched states of hydrogen with $n = 25$ in magnetic field $B(x)$

table 3.1[1]. This shows, that due to the high principle quantum number n, that yields a very large J as compared to the I of the hydrogen's core, there is hardly any difference between $|g_F M_F|$ and $|g_J M_J|$. Hence, for our estimation that is based on the magnetic field interaction with the stretched states, it is not relevant which description to choose.

Using the fine structure with J and M_J as good quantum numbers, we see in figure 3.6 the dependence of the contrast on an increasing field gradient, where the two stretched states with $M_J = \pm 24.5$ are included only. As expected, the patterns are shifted with respect to each other by half a grating period at a gradient of $\sim 0.14 \frac{\mathrm{mG}}{\mathrm{cm}}$ (see figure 3.6(a)). The first maximum of the contrast of these states can be found at a gradient of $0.28 \frac{\mathrm{mG}}{\mathrm{cm}}$, which corresponds to a shift of one grating period between the two stretched states with $M_J = \pm 24.5$ and is shown in figure 3.6(b).
Although the behaviour is similar to that of argon given in figure 3.6, there is an important difference: instead of considering five magnetic substates as for argon, only the two most sensitive ones have been examined here, which is sufficient for an estimation of the critical field gradient. Nevertheless, due to this limitation, no substructure can be observed as in between $\sim 0.5 \frac{\mathrm{G}}{\mathrm{cm}}$ and $\sim 3 \frac{\mathrm{G}}{\mathrm{cm}}$ of figure 3.3.

For the experimental construction, it remains to note that in order to uphold a contrast of better than ~ 0.5 (as figure 2.11(c) showed to be sufficient) disturbing

---

[1]The fine structure of hydrogen, that is determined by the common LS-coupling [51, 54, 55], yields as stretched states for our case the ones with $n = 25, L = 24, J = 24.5, M_J = 24.5$.
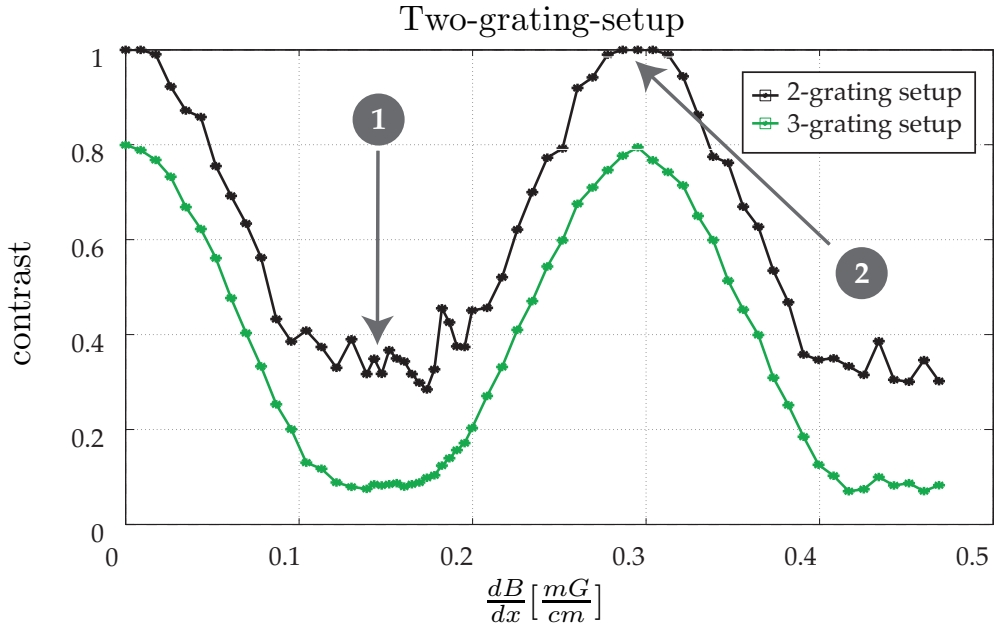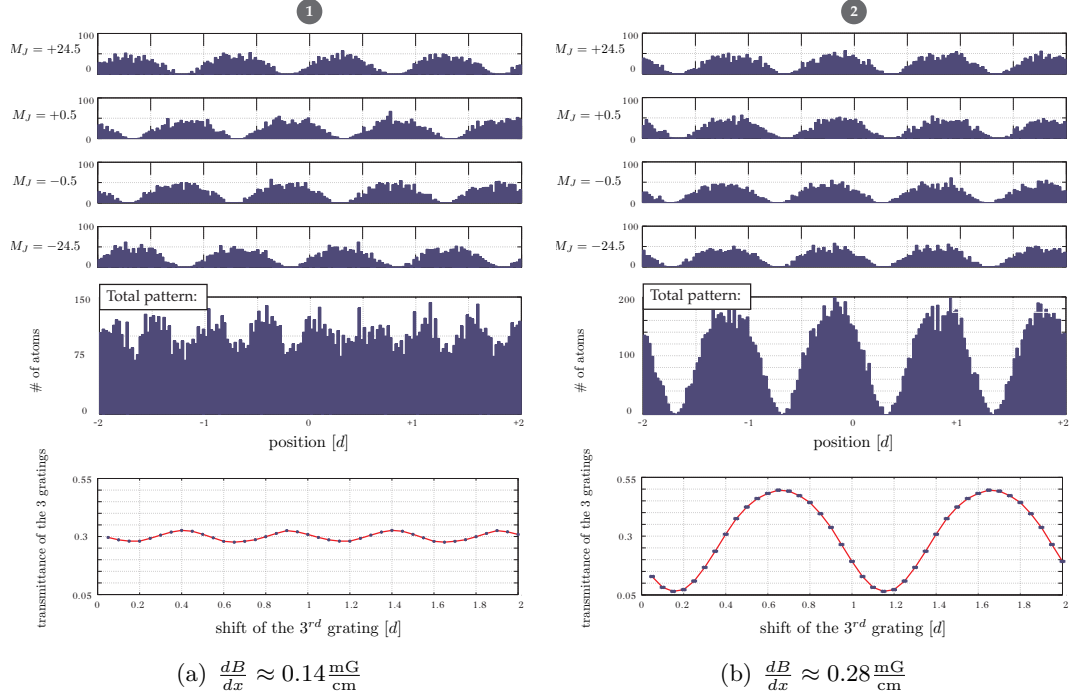
(a) $\frac{dB}{dx} \approx 0.14 \frac{\mathrm{mG}}{\mathrm{cm}}$

(b) $\frac{dB}{dx} \approx 0.28 \frac{\mathrm{mG}}{\mathrm{cm}}$

Figure 3.6: Increasing the magnetic field gradient in the antihydrogen experiment. Regarding the output of the two-grating Moiré-setup in figure 3.6 we see an effect that is not caused by the external field. Due to the small number of antihydrogen contributing to the signal, the statistical fluctuations, which yield a noisy signal close to the minima of the contrast, are much higher than in the argon-experiment. Scanning the 3rd grating for detection purposes smooths this effect but also yields a contrast that will not exceed 0.8 any more (see section 4.2 for further details on this limitation).

magnetic field gradients of the order of $c_B(\overline{H}) \approx 0.08\,\frac{\text{mG}}{\text{cm}}$ need to be controlled at the AE$\overline{\text{g}}$IS-experiment. However, it should be stressed at this point that we have neglected the limited lifetime of Rydberg atoms, which can be expected for $n = 25$ to be $\sim (50...100)\,\mu\text{s}$ [59]. Including this fact in a more sophisticated sensitivity analysis will increase this critical field gradient and provide easier shieldable values. Due to the large number of magnetic traps (with B-fields of $\sim 1\,\text{T}$) in the direct or close surounding of the AE$\overline{\text{g}}$IS-setup and the large integration time necessary for the aimed 1% of accuracy of the g-measurement, an appropriate magnetic shielding seems to be unavoidable.

3.3.3 Solutions: Constant Offset Field

One option to get rid of a disturbing magnetic field gradient along the deflectometer is to decrease any kind of external magnetic field via an appropriate magnetic shielding. For this purpose, a common solution is the usage of a so-called μ-metal-shield around the setup. Such a surrounding out of μ-metal – a material with very high magnetic permeability at low field strengths – is a very efficient for screening magnetic field lines. As such a surrounding is mostly only realisable by costum-made solutions, this way of magnetic shielding turns out to be very expensive. Besides this, μ-metal is very sensitive on mechanical damages like buckles and other deformations due to unwanted mechanical strains. Consequently, both the shielding's engineering and its implementation into the experimental setup is very elaborate and rises the expenses a lot.

There are also other approaches to cope with a disturbing magnetic field gradient. For one of them – to which we refer to as *Bias-Reduced-Gradient-Susceptibility* (BRGS) – we need to add a constant magnetic field in one of the directions y or z that are perpendicular to the one, in which gravity is acting. To understand the functionality of this method, we consider the very general case of a three-dimensional temporarily constant B-field with

$$\mathbf{B}(\mathbf{r}) = (B_x(\mathbf{r}), B_y(\mathbf{r}), B_z(\mathbf{r})) \tag{3.20}$$

at any position $\mathbf{r}$. As given in equation 3.10 and 3.16, it is the gradient in the vertical direction that disturbs the gravity measurment. With $|\mathbf{B}(\mathbf{r})| = \sqrt{B_x(\mathbf{r})^2 + B_y(\mathbf{r})^2 + B_z(\mathbf{r})^2}$

this gradient reads in general

$$\frac{\partial |\mathbf{B}(\mathbf{r})|}{\partial x} = \frac{B_x(\mathbf{r})\frac{\partial B_x(\mathbf{r})}{\partial x} + B_y(\mathbf{r})\frac{\partial B_y(\mathbf{r})}{\partial x} + B_z(\mathbf{r})\frac{\partial B_z(\mathbf{r})}{\partial x}}{\underbrace{\sqrt{B_x(\mathbf{r})^2 + B_y(\mathbf{r})^2 + B_z(\mathbf{r})^2}}_{=|\mathbf{B}(\mathbf{r})|}}. \tag{3.21}$$

If we can now assume that the vertical variations of the two field components $B_y(\mathbf{r})$ and $B_z(\mathbf{r})$ are neglectable, i. e. $\frac{\partial B_y(\mathbf{r})}{\partial x} \approx 0$ and $\frac{\partial B_z(\mathbf{r})}{\partial x} \approx 0$, we will be able to use one of the offsets $B_y(\mathbf{r})$ or $B_z(\mathbf{r})$ in the denominator as tuneable parameters. Hence, we aim to reduce the total value of $\frac{\partial |\mathbf{B}(\mathbf{r})|}{\partial x}$ to a value, where its disturbing effect on the measurements can be neglected, just by increasing one of the offset fields in the other directions. Depending on the necessary field-values for the particular setups, such a tuning that influences only an offset field component can be quite challenging to realise experimentally, as it is important to keep any vertical variations, i. e. $\frac{\partial B_y(\mathbf{r})}{\partial x}$ and $\frac{\partial B_z(\mathbf{r})}{\partial x}$ neglectable at the same time.

With our sensitivity analysis of sections 3.3.1 and 3.3.2 we found critical vertical field gradients $c_B = \frac{\partial |\mathbf{B}(\mathbf{r})|}{\partial x}$ for the experiment with argon, $c_B(\text{Ar}) \approx 330 \, \frac{\text{mG}}{\text{cm}}$, and for the one with antihydrogen, $c_B(\overline{\text{H}}) \approx 0.08 \, \frac{\text{mG}}{\text{cm}}$.

For an outline of the experimental realisation of BRGS, we concentrate on the experimental feasability of it for the particular geometry of the Moiré-deflectometer. As the geometry of the deflectometer setup suggests, we attempt to realise the necessary additional magnetic field for BRGS via a solenoid, which is aligned co-axially with the z-axis of the deflectometer. The induced additional constant offset field in the z-direction provides two major advantages: As opposed to $B_y(\mathbf{r})$, it can be kept constant during the flight of the atoms through the deflectometer reasonable easily by a very long solenoid. Furthermore, a solenoid's implementation into the experimental setup seems feasible surrounding the currently 2.5 m long vaccuum chamber.

In order to estimate the necessary construction of such a solenoid we need to determine the participating field strengths by calculating the magnetic field within a solenoid of appropriate size. For this purpose, we follow the derivation of N. Derby and S. Olbert [60]. In cylindrical coordinates they use the Biot-Savart law and integrate along the z-axis. With a coordinate system as sketched figure 3.7, they received for any point

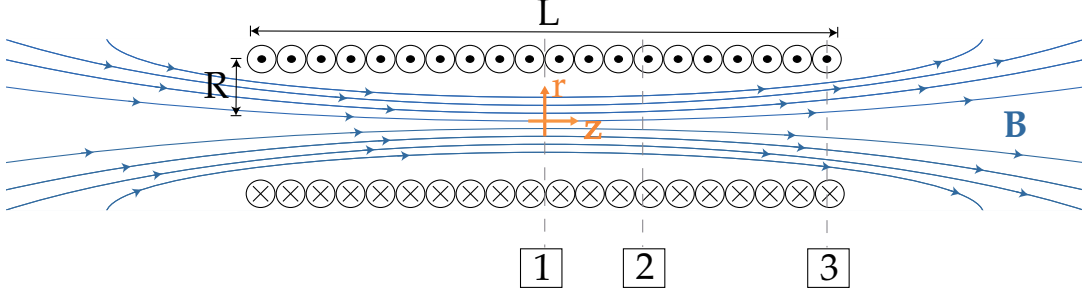## 3. SENSITIVITY ANALYSIS OF A MOIRÉ-DEFLECTOMETER ON EXTERNAL FIELDS

Figure 3.7: Sketch of a finite long solenoid for the calculation of the magnetic field lines. The situations 1, 2 and 3 are plotted in further detail in figure 3.9.

given by (r, z) a magnetic field component in radial direction

$$B_r(r, z) = B_0 \int_0^{\frac{\pi}{2}} (\cos^2 \psi - \sin^2 \psi) \cdot$$

$$\left(\frac{\alpha_+}{\sqrt{\cos^2 \psi + k_+^2 \sin^2 \psi}} - \frac{\alpha_-}{\sqrt{\cos^2 \psi + k_-^2 \sin^2 \psi}} \right) d\psi \qquad (3.22a)$$

and for the one in axial direction, they found

$$B_z(r, z) = \frac{B_0 R}{r + R} \int_0^{\frac{\pi}{2}} \frac{\cos^2 \psi + \gamma \sin^2 \psi}{\cos^2 \psi + \gamma^2 \sin^2 \psi} \cdot$$

$$\left(\frac{\beta_+}{\sqrt{\cos^2 \psi + k_+^2 \sin^2 \psi}} - \frac{\beta_-}{\sqrt{\cos^2 \psi + k_-^2 \sin^2 \psi}} \right) d\psi, \qquad (3.22b)$$

with

$$B_0 = \frac{\mu_0}{\pi} nI, \qquad\qquad \gamma = \frac{R - r}{R + r},$$

$$z_\pm = z \pm \frac{L}{2}, \qquad\qquad k_\pm = \sqrt{\frac{z_\pm^2 + (R - r)^2}{z_\pm^2 + (R + r)^2}},$$

$$\alpha_\pm = \frac{R}{\sqrt{z_\pm^2 + (R + r)^2}}, \qquad\qquad \beta_\pm = \frac{z_\pm}{\sqrt{z_\pm^2 + (R + r)^2}},$$

where the magnetic permeability μ_0 and the details of the solenoid are included by its length L, its radius R, and its winding via n turns per unit length with current I. The integrals in equation 3.22a and 3.22b are special forms of the generalized complete elliptic integral [60]

$$C(k_c, p, c, s) = \int_0^{\frac{\pi}{2}} \frac{c \cos^2 \varphi + s \sin^2 \varphi}{(\cos^2 \varphi + p \sin^2 \varphi) \sqrt{\cos^2 \varphi + k_c^2 \sin^2 \varphi}} d\varphi, \qquad (3.23)$$

which simplifies the evaluations of the magnetic field components. They become [60]

$$B_r(r,z) = B_0(\alpha_+ C(k_+, 1, 1, -1) - \alpha_- C(k_-, 1, 1, -1)) \tag{3.24a}$$

$$B_z(r,z) = \frac{B_0 R}{r + R}(\beta_+ C(k_+, \gamma^2, 1, \gamma) - \beta_- C(k_-, \gamma^2, 1, \gamma)). \tag{3.24b}$$

Using these expressions, the magnetic field components can be evaluated at any point within a solenoid. Figure 3.8 shows exemplary the axial dependence of the off-axis field components, i.e. they are not evaluated at the symmetry axis of the solenoid, the z-axis, but at a distance $r = \frac{R}{2}$. This calculation refers to a solenoid of $L = 3\,\mathrm{m}$, $R = 30\,\mathrm{cm}$, $n = 200\,\mathrm{m}^{-1}$ and $I = 100\,\mathrm{A}$.

For our application of the solenoid, we need to consider c_B, which is given in the
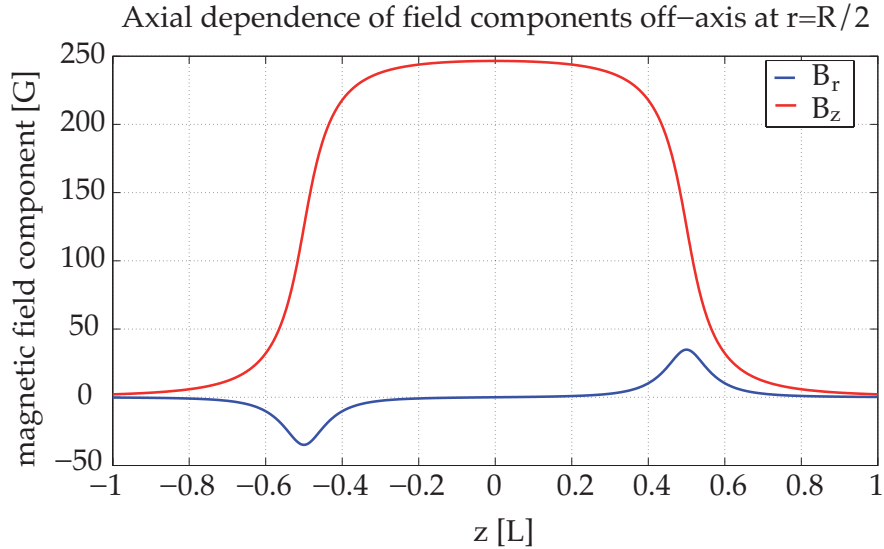
Figure 3.8: Axial dependence of the off-axis magnetic field components B_r and B_z at $r = \frac{R}{2}$.

solenoid's cylindrical coordinates by

$$\frac{\partial \left| \mathbf{B}(\mathbf{r}) \right|}{\partial r} = \frac{B_r(\mathbf{r})\frac{\partial B_r(\mathbf{r})}{\partial r} + B_z(\mathbf{r})\frac{\partial B_z(\mathbf{r})}{\partial r}}{\underbrace{\sqrt{B_r(\mathbf{r})^2 + B_z(\mathbf{r})^2}}_{= |\mathbf{B}(\mathbf{r})|}}. \tag{3.25}$$

In order to keep this value low but only determined by the field components of the solenoid, a large offset in z-direction is preferable. Thus, figure 3.8 suggests to use a very long solenoid, where B_z is high and does not change considerably along the

deflectometer.

Besides this, it is essential to know the radial dependencies of the two field components along the deflectometer. These dependencies are plotted in figure 3.9 for the exemplary z-positions denoted in figure 3.7. The corresponding radial dependence of c_B at the bottom each subfigure is plotted together with the critical values c_B for the argon- and the antihydrogen-experiment with the dashed and the dotted line, respectively. This illustration demonstrates the importance to position the deflectometer in the axially central region of the solenoid, as c_B increases from figure 3.9(a) to 3.9(b). Coming too close to the solenoid's edges as shown in figure 3.9(c), the influence of the radial field components become that strong, that c_B of this particular solenoid even lies above the critical gradient value of the argon experiment.

Nevertheless, figure 3.9 shows, that it is possible to construct a solenoid for the BRGS-method for the argon experiment, one only needs to be careful to construct it sufficiently long.

At the same time, figure 3.9 also points out that this method is a lot more difficult for the experiment with antihydrogen. However, there is indeed a possibility to use BRGS at the experiment at CERN: Instead of excluding the magnetic fields of the magnetic traps of the AE$\overline{g}$IS-setup by compensation coils right before the deflectometer region, one might think of using these field lines and leading them with an appropriate surrounding shielding right through the whole deflectometer. This way, a large offset in longitudinal direction with a small gradient in the vertical one can be achieved, too.[1]

3.4 Electric Field

Besides a vertical magnetic field gradient, other disturbing effects may also originate from electric fields. These fields induce the so-called *Stark-effect*, which describes electrically induced internal energy shifts, that are either proportional to the electric field amplitude E in case of the *linear Stark-effect*, or proportional to the square of this

---

[1]For the sake of completeness it is improtant to note that the considerations that yield figures 3.9 are based on the case of a magnetic field that is symmetric around the z-axis. Hence, figure 3.9 only shows the field configuration within the solenoid. As soon as the external disturbing field – which presumabely does not obbey this particular symmetry – becomes too large and this symmetry breaks down, we need to go back to equation 3.21 in cartesian coordinates and find appropriate simplifications by comparing the actual field strength that contribute.
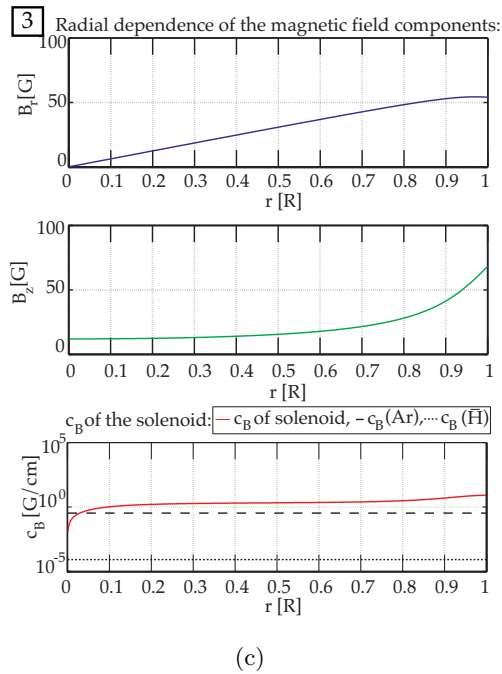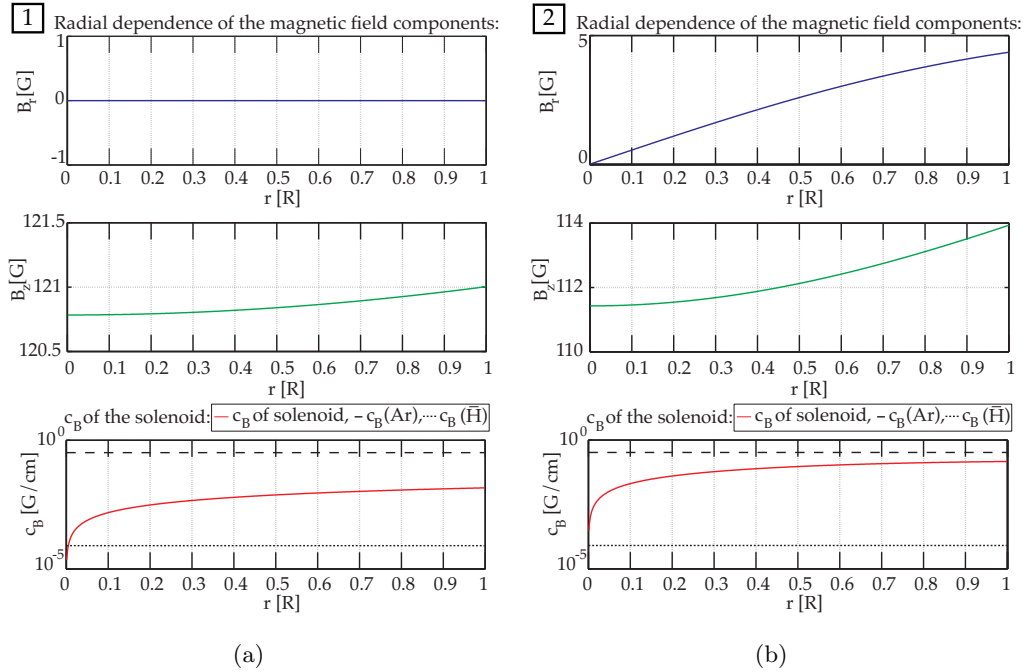
Figure 3.9: Radial dependencies of the radial and axial magnetic field component B_r and B_z for the exemplary situations 1, 2 and 3 as denoted in figure 3.7.

3. SENSITIVITY ANALYSIS OF A MOIRÉ-DEFLECTOMETER ON EXTERNAL FIELDS

amplitude, which is known as the *quadratic Stark-effect*.

In general, a Stark-shift is caused by the interaction between an electric dipole $\boldsymbol{\mu}_{\mathrm{el}}$ and an external electric field $\boldsymbol{E}$ with its field amplitude $E = |\boldsymbol{E}|$. This interaction yields an internal energy shift of the atom, that can be calculated via perturbation theory, if the shift is small compared to the internal energy splittings of the atom. The perturbation part of the atomic Hamiltonian writes

$$\mathcal{H}_{el} = -\boldsymbol{\mu}_{\mathrm{el}} \cdot \boldsymbol{E} \tag{3.26}$$

and the energy shift $\Delta\varepsilon^{(1)}$ of the first order perturbation term becomes [61]

$$\Delta\varepsilon^{(1)} = \langle 0| \, \boldsymbol{\mu}_{\mathrm{el}} \cdot \boldsymbol{E} \, |0\rangle = 0 \tag{3.27}$$

As $\mathcal{H}_{el}$ is of odd parity, $\Delta\varepsilon^{(1)}$ varnishes for unperturbed states $|0\rangle$, that have a definite parity. For these states, no permanent dipole moment and no linear dependence of the energy shift is observable. Thus, the interaction with the electric field is governed by the second order perturbation, whose energy shift is given by [51, 55]

$$\Delta\varepsilon^{(2)} = -\sum_{c\neq 0} \frac{\langle 0| \, \boldsymbol{\mu}_{\mathrm{el}} \cdot \boldsymbol{E} \, |c\rangle \, \langle c| \, \boldsymbol{\mu}_{\mathrm{el}} \cdot \boldsymbol{E} \, |0\rangle}{\varepsilon_c - \varepsilon_0}, \tag{3.28}$$

where $|c\rangle$ denotes the state, to which the unperturbed one $|0\rangle$ is coupled by the external field. This coupling between the two states of different energy is an interesting difference to the first order perturbation $\Delta\varepsilon^{(1)}$, that can only couple states of the same energy. The amount of electrically induced energy shift $\Delta\varepsilon^{(2)}$ strongly depends on the energy gap between the coupled states given by the difference of their eigenenergies $\varepsilon_c - \varepsilon_0$. Another interesting difference to the first order perturbation term is the E^2-dependence of $\Delta\varepsilon^{(2)}$ that is eponymous for the quadratic Stark-effect.

The distinction between the two types of Stark-effects gains importance when considering the two atomic species to be examined with the Moiré-deflectometer. This will be done in the following subsections.

3.4.1 External E-Field and the Argon Measurement

As it is the case for most atoms, the internal energies of argon with the same principal quantum number n do not have degenerate angular momentum states. Hence, the first order perturbation term $\Delta\varepsilon^{(1)}$ varnishes and the resulting states do not exhibit a

permanent electric dipole moment (on time average). Therefore, the external electric field first needs to induce a dipole moment to interact with. This induced dipole moment can be evaluated by

$$\boldsymbol{\mu}_{\mathrm{el}} = \boldsymbol{\alpha}_{\mathrm{el}} \cdot \boldsymbol{E}, \tag{3.29}$$

where the atom's electric polarisability $\boldsymbol{\alpha}_{\mathrm{el}}$ is assumed be diagonalised.[1] Its components depend on the internal atomic electron configuration and the good quantum numbers, which are either governed by the fine-or hyperfine-structure of the atom. As the $^{40}\mathrm{Ar}$ has no nuclear spin, it only exhibits fine-structure-splitting and the valid good quantum numbers for the interaction with an external field are J and M_J.

The polarisability tensor $\boldsymbol{\alpha}_{\mathrm{el}}$ has been measured for the $^3P_2$ metastable state of argon by Pollack et al. [62]. They found[2]

$$\alpha_{\mathrm{el,x}}(M_J = 0) = (52.4 \pm 4.8) \cdot 10^{-24}\,\mathrm{cm}^3 \tag{3.30a}$$

$$\alpha_{\mathrm{el,x}}(M_J = \pm 1) = (50.4 \pm 3.5) \cdot 10^{-24}\,\mathrm{cm}^3 \tag{3.30b}$$

$$\alpha_{\mathrm{el,x}}(M_J = \pm 2) = (44.5 \pm 3.1) \cdot 10^{-24}\,\mathrm{cm}^3. \tag{3.30c}$$

Note that as opposed to the magnetically induced Zeeman-shift, the magnitude of electrically induced Stark-shift does not depend on the sign of M_J. Another interesting aspect are the absolute magnitudes of the components of equation 3.30. They can be understood by considering the argon's internal structure:

- Due to the excitation of the argon atom to its metastable state (as can be seen in figure 3.1) which yields an incomplete shell in the atomic core, one might expect a strong anisotropy of the interactomic charge distribution and hence, even a permanent electric dipole moment of the atom. But since the contribution of the core to the polarisability of the atom is very small, there is hardly any anisotropy induced by it. This is confirmed by the results of Pollack et al.: The components of the polarisability are almost symmetric in all three spatial directions [62].

---

[1]For an analytic calculation of $\boldsymbol{\alpha}_{\mathrm{el}}$ that depends on the atom's internal structure, equation 3.28 needs to be evaluated explicitely.

[2]When comparing their results, note the differently orientated coordinate system in the experiment of Pollack et al. [62].

3. SENSITIVITY ANALYSIS OF A MOIRÉ-DEFLECTOMETER ON EXTERNAL FIELDS

- The main influence of the atom's interatomic structure to the electrical property is given by the valence electron. As the valence electron for the considered $^3P_2$-state is in a S-state, the $\alpha_{\mathrm{el,x}}(M_J)$s do not differ a lot for different M_J-states [62].

Using this polarizability, we can calculate the induced dipole moment of equation 3.29 and calculate the energy shift that originates from the interaction of this dipole with the external field. This is given by

$$\Delta\varepsilon_{\mathrm{Ar}}^{(2)} = -\frac{1}{2}\boldsymbol{\mu}_{\mathrm{el}} \cdot \boldsymbol{E} \tag{3.31}$$

and yields an electric force $\boldsymbol{F}_{el}$ on the atom. Restricting our analysis to only vertically dependent fields, we can determine the corresponding force $F_{el,x}$ as

$$|F_{el,x}| = \alpha_{\mathrm{el,x}}(M_J)E\frac{dE}{dx}, \tag{3.32}$$

where $\alpha_{\mathrm{el,x}}(M_J)$ denotes the $\alpha_{\mathrm{el,xx}}$-component of the polarisability tensor.

For an estimation of the smallest electric field configuration, that can disturb the gravitational measurement of a Moiré-deflectometer, we precede analogous to our examinations of the magnetic field in section 3.3. For this purpose, both the most and the least sensitive states need to be identified first.[1] With equation 3.32 we identify the most sensitive ones as the ones with $M_J = 0$ and the least sensitive ones turn out to be the ones with $M_J = \pm 2$. Hence, for a Moiré-setup with $T_1 = T_2 = T$, we use equations 3.3 and 3.32 to determine the electric field, where the Moiré-patterns of the two interesting states $M_J = 0$ and $M_J = \pm 2$ are shifted by half a grating period with respect to each other. Thus, we find

$$|\Delta x_{\mathrm{el}}| \overset{!}{=} \frac{1}{2}d \tag{3.33}$$

$$\Rightarrow |\Delta x_{\mathrm{el}}| = \left|\frac{\alpha_{\mathrm{el,x}}(M_J = 0) - \alpha_{\mathrm{el,x}}(M_J = \pm 2)}{m}E\frac{dE}{dx}T^2\right| \tag{3.34}$$

$$\left|\left(E\frac{dE}{dx}\right)_{\frac{1}{2}d}\right| \approx 280\,\frac{\mathrm{V}^2}{\mathrm{m}^3}, \tag{3.35}$$

---

[1]Note that, as opposed to the magnetic field analysis, all of the atomic states get deflected by the quadratic Stark-effect.

where we used the identity of $\alpha_{\mathrm{el,x}}[\mathrm{cm}^3] = \frac{10^{-6}}{4\pi\varepsilon_0}\alpha_{\mathrm{el,x}}\left[\frac{\mathrm{Cm}^2}{\mathrm{V}}\right]$ and note the dependence on both, the offset field amplitude E and its vertical gradient $\frac{dE}{dx}$.

Equation 3.35 provides a first rough estimate for the order of magnitude of the critical external field. More details are given in figure 3.10, which shows the results of our Monte-Carlo simulations of the argon experiment. An external electric field has been varied for the predicted critical order of magnitude and the contrast's dependence of the three-grating setup on this electric field is plotted in the top subfigure. It clearly demonstrates that a critical loss of contrast, which corresponds to $C \sim 0.5$ can be observed at $\sim 170 \frac{\mathrm{V}^2}{\mathrm{m}^3}$. A deeper insight to this loss of contrast and how the different substates contribute to it, is given by the two inlays. They show the Moiré-pattern right before the third grating for the different substates and the total pattern.

3.4.2 External E-Field and the Antihydrogen Measurement

For the electric field sensitivity analysis of the antihydrogen experiment, a more sophisticated approach is neccessary than the one we used so far. The first issue arises for the theoretical description of a Rydberg atom in an external electric field. Due to their excitation and the anisotropic field, we need to change to parabolic coordinates, in order to find separable solutions of the Hamiltonian. In this new coordinate system, the known spherical quantum numbers n, L and M are replaced by n_1, n_2 and m [63]. Thus, with the electronic quantum number $k = n_1 - n_2 = (-n+1),...(n-1)$, the relationship to the known main principal quatnum number n is given by [63]

$$n = n_1 + n_2 + |m| + 1. \tag{3.36}$$

For instance, in the electric field, the 'stretched states' of a hydrogen Rydberg atom with $n = 25$ are the ones with $n_1 = 24, n_2 = 0$ ($n_1 = 0$, $n_2 = -24$) and $k = 24$ ($k = -24$).

Using these new quantum numbers, we can evaluate the Stark-shifts $\Delta\varepsilon_{\mathrm{Ry}}^{(1,2)}$ for Rydberg states via first and second order perturbation theory. In atomic units, they write [63]

$$\Delta\varepsilon_{\mathrm{Ry}}^{(1,2)} = -\frac{1}{2n^2} + \frac{3}{2}nkE - \frac{n^4}{16}\left(17n^2 - 3k^2 - 9m^2 + 19\right)E^2, \tag{3.37}$$

Note at this point that, in contrast to an argon atom, the field configuration for the energy of the Stark shift is already dependent on E and its gradient $\frac{dE}{dx}$. Evaluating

the electrically induced force on the atoms out of equation 3.37, we find in atomic units

$$F_{el,x}\left(E\frac{dE}{dx}\right) = \frac{3}{2}kn\frac{dE}{dx} - \frac{1}{8}n^4(17n^2 - 3k^2 - 9m^2 + 19)E\frac{dE}{dx}, \qquad (3.38)$$

where we assumed the electric field to act exclusively in the vertical direction.

So far, the strong dependence of this force on the still unknown quantum numbers and the additionally dependence on both, $\frac{dE}{dx}$ as well as $E\frac{dE}{dx}$, seem to be the main challenges for our approach. In addition to this, there are also further issues, as the *Inglis-Teller-limit*[1] or the fact of the limited lifetime of the atoms, which is not expected to exceed $(50...100)\,\mu$s [59]. With a time of flight of the antihydrogen atoms in the order of milliseconds, the description as Rydberg-atoms breaks down during their flight through the deflectometer. Hence, our approach is not adequate for the electric field sensitivity analysis of the antihydrogen experiment. A more promising approach is left to the group of Prof. Dr. F. Merkt, the specialists on Rydberg-hydrogen in electric fields of the AE$\overline{\text{g}}$IS-collaboration. They also implement the accerlerating fields for the intitial beam formation.

---

[1]In this context, the Inglis-Teller-limit refers to the electric field strength E_{IT}, for which the adjacent n-states of the Rydberg atom approach degeneracy. In atomic units, it is given by $E_{\text{IT}} = \frac{1}{3n^5}$ [63].
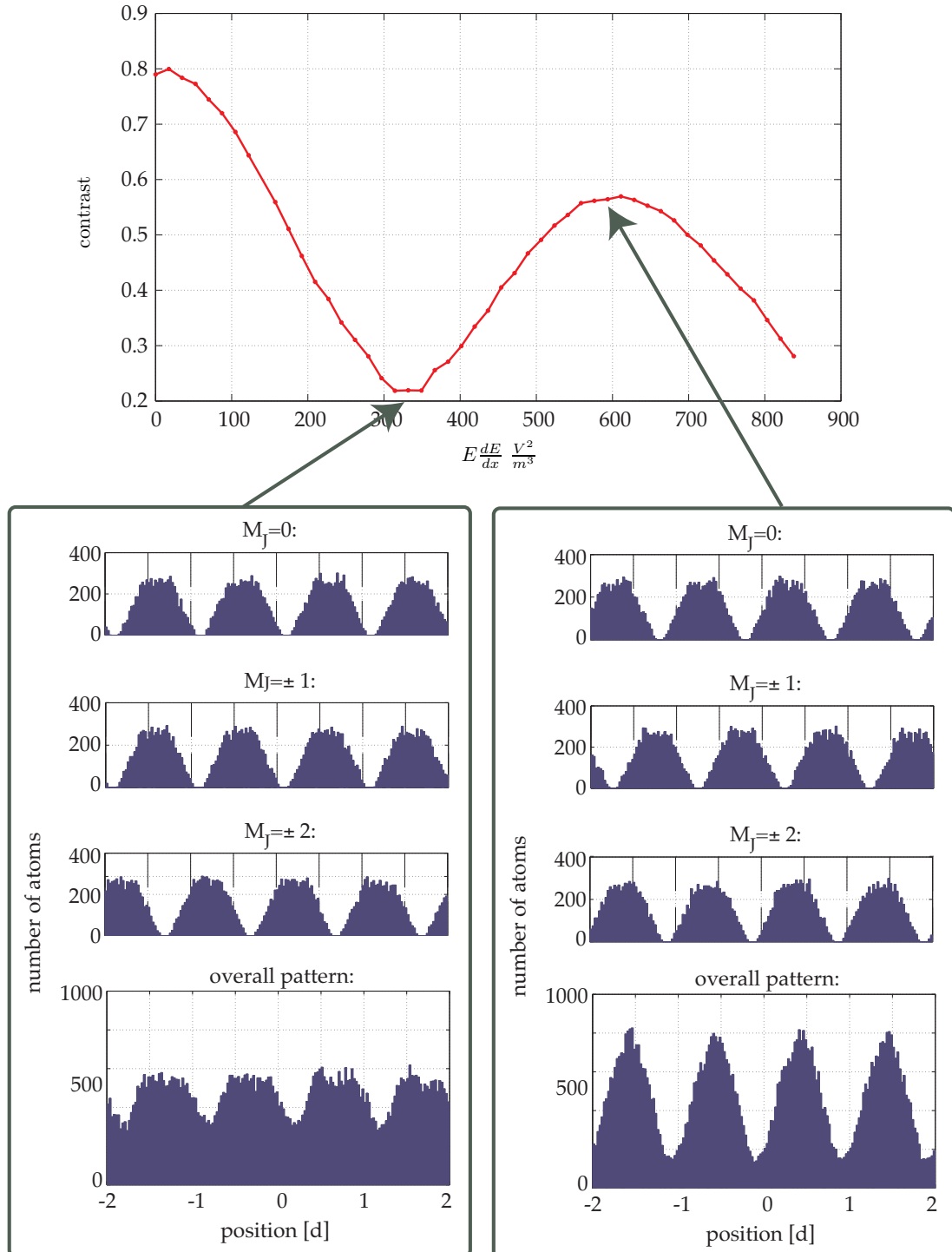
Figure 3.10: The change of contrast dependent on the external electric field $E\frac{dE}{dx}$ for a two grating setup in the argon experiment. The inlays show examplary the shifts of the different substates and how their addition leads to the total pattern given at the bottom. These are results of a Monte-Carlo simulation for the experimental setup in Heidelberg and with an input of 10^9 atoms per atomic substate.

Chapter 4

Construction of the Moiré-Deflectometer

4.1 Introduction

Considering the simple sketch of an ordinary Moiré-setup in figure 2.3, it seems to be straightforward to implement such a setup into the AE$\overline{\mathrm{g}}$IS-experiment at CERN. However, due to the experimental conditions of the ambitious experiment with antihydrogen, there are a lot of details to account for when designing and implementing an appropriate Moiré-setup. Hence, the following chapter provides the most important of these details as well as the resulting design.

This chapter starts with an outline of the requirements on the design of the gratings. In this context, the design of both grating structures are discussed – the major one that consists of the atoms' transmission gratings as well as the optical gratings for the Mach-Zehnder-interferometers. Subsequently, a brief explanation of the basic principle of Deep Reactive Ion Etching (DRIE), the processing method that is used for manufacturing the gratings, is given together with an outline of the problems that occured during the processing of the prototypes. In addition to this, tests of the first prototypes of the atoms' grating structures are presented. These tests apply the previously described Talbot-effect (see section 2.4.1).
Besides these details about the core of the deflectometer – the gratings – this chapter also covers the construction of an appropriate designed wafer mount, to which we refer

to in the following as 'riders'. The brief overview of the construction of these riders and their mounting within the experimental setup in Heidelberg is given. Subsequently, the results of the first vibration and stability analysis, which has been performed with a prototype of the mounting construction [64], are summarised.

4.2 The Design of the Gratings

In order to design appropriate transmission gratings for a Moiré-deflectometer of the AE$\overline{g}$IS-experiment at CERN, there are four major requirements:

Active Aperture: The active aperture of the gratings needs to be large enough to capture all of the produced antihydrogen atoms. First estimates of our collaborators [65] provide an expected beam divergence of approximately 50 mrad. Thus, for a Moiré-deflectomter with an overall length of $2L = 2$ m, we need gratings whose active aperture covers a beam diameter of ~ 20 cm. This requirement can be fulfilled by using 8 inch-silicon wafers as raw material. Silicon suggests itself, as there are a lot of different etching techniques [66, 67, 68, 69] known to imprint small structures on such wafers. Some of these techniques will be used to imprint the structure of the transmission gratings on the wafers.

Structure of the Atoms' Transmisson Gratings: The major structure of the transmission gratings needs to be chosen such that the necessary sensitivity[1] of the deflectometer for the gravitational measurement can be achieved. Besides this, the scale of the output pattern at the end of the deflectometer needs to be large enough that a future antimatter detector can resolve it spatially. These two requirements can be fullfilled with a grating period $d = 40 \, \mu$m [65].

The best open fraction[2] of these gratings can be found with Monte-Carlo simulations of the experiment. For identical gratings, figure 4.1 shows their results for different open fractions f_{open}.

The upper plot provides an overview for open fractions of up to 70 %. Although the contrast increases again when increasing f_{open} beyond $f_{\text{open}} = 50$ %, it does not exceed

---

[1]For more details on the requirements of the sensitivity refer to section 2.7.2.

[2]The open fraction f_{open} of a transmission grating is defined as the fraction of a slidwidth a to its period d, i. e. $f_{\text{open}} = \frac{a}{d}$.

the values that can already be reached with smaller $f_{\text{open}} < 50\,\%$. The lower plot of figure 4.1 shows a zoom into the region of these smaller open fractions. It demonstrates that a good trade-off between a low offset and a large contrast of $C = 0.8$ is found with $f_{\text{open}} = 30\,\%$, which is plotted with the red triangles. This result agrees with other investigations using a Moiré-deflectometer as gravimeter [22].

For the analysis of different open fractions, we used the three-grating Moiré-setup in
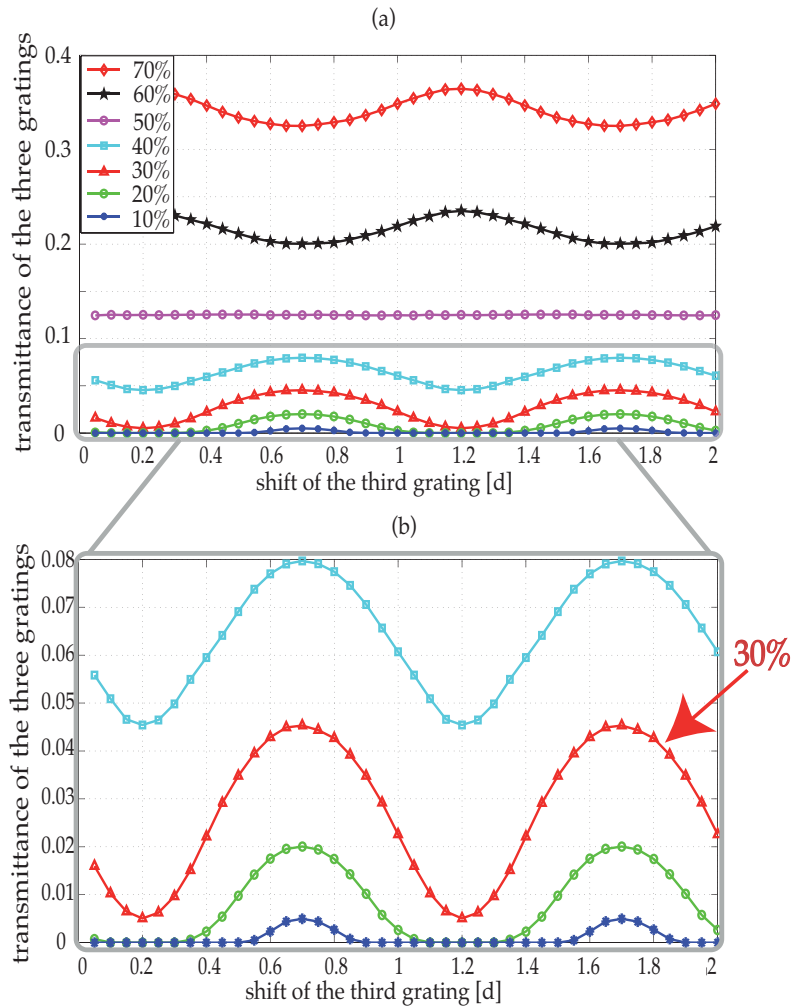
Figure 4.1: Output signal of a three-grating Moiré-setup. These results are retrieved from Monte-Carlo simulations (see Chapter 3 for more details) of the experiment with ^{40}Ar in Heidelberg. Simulation the antihydrogen-experiment will yield similar results.

Heidelberg, whose output is more sensitive on f_{open} than a two-grating version planned

at CERN. This way, we also account for the possibility that the necessary spatial resolution of the AE$\overline{\text{g}}$IS-dectector cannot be reached. In this case, the planed two-grating setup at CERN can still be replaced by the three-grating version including its spatial resolution achieved by a third grating. In addition to this option, it is important to note that the possibility to use the same gratings in a three grating setup, enables us to test the deflectometer for sensitivies far beyond the one that is required for the setup at CERN (see section 2.7.2). Due to the high particle flow that is essential for these sensitivities, usual detection methods via Multi-Channel-Plates or similar detectors with the necessary spatial resolution are useless due to their quick saturation.

Requirements for the Stability Analysis:
As shown in section 2.7.2, we need long integration times to reach the desired $g_{\min}$ of the deflectometer. Hence, not only the short-but also the long-term stability of the deflectometer is of major importance. To monitor both ranges of the stability during the gravitational measurements, we implement optical Mach-Zehnder-interferometers. Figures 4.2 and 4.3 show schematic sketches of these interferometers and their implementation. As figure 4.2 illustrates the interferometers can be used to control movements across the silicon wafers by comparing the outputs out$_{\text{right}}$ and out$_{\text{left}}$. Besides this, figure 4.3 illustrates in more detail how such interferometers provide information about spatial movements. Recording both outputs, O_1 and O_2, enables a stability characterisation of the setup that is independent of

Figure 4.2: General alignment of the optical Mach-Zehnder-interferometer

the laser input. This way, we can determine successful tools for vibration islotation. A summary of this vibration analysis is given in section 4.6 and further details can be found in [64].
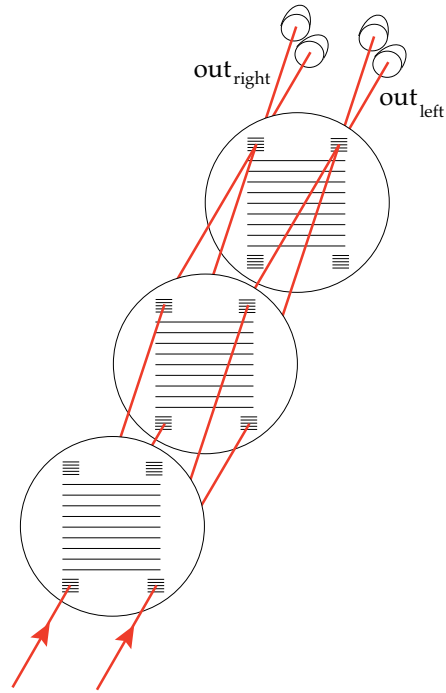
Note that optical Mach-Zehnder-interferometers enable the recording of the setup's

stability during the actual data acquisition of the entire gravimeter. This can be used in future setups for either the data processing after the actual measurement or for an active control of the gratings' position. Which of these options will be applicable depends on the time scales of the disturbing movements and vibrations of the final setup.
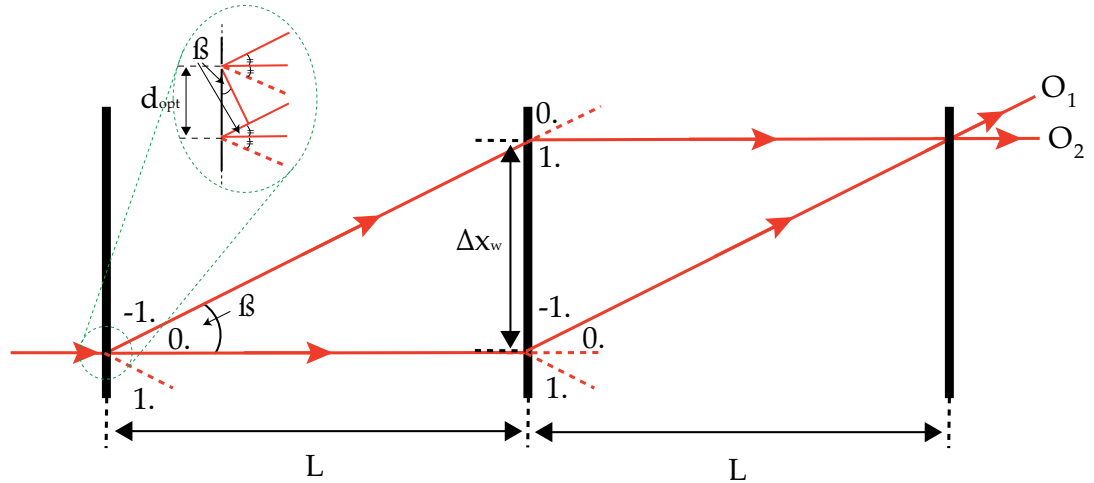

Figure 4.3: Side view of the alignment of a Mach-Zehnder-interferometer. The geometry of the entire setup yields equation 4.1a. The green dotted inlay denotes a zoom in; it illustrates the diffraction process that leads to equation 4.1b.

Requirements for the Additional Optical Gratings: For the experimental realisation of the optical Mach-Zehnder-interferometers and their transmission gratings out of silicon wafers, the choice of the laser's wavelength is of major importance. We restrict ourselves on the commercially available wavelengths of a common Helium-Neon-Laser ($\lambda = 632\,\text{nm}$) and a Distributed FeedBack (DFB) Laserdiode ($\lambda = 1550\,\text{nm}$). These two different wavelengths offer us the possibility to test the special characteristics of a silicon transmission grating for our applications. As silicon becomes transparent for far infrared light, i. e. for $\lambda > 1\,\mu\text{m}$ [70], the gratings rather act as phase- than as amplitude-gratings for these wavelengths. Depending on the structue of the gratings and the exact properties of the used wafers, the gratings may even act as a mixture of both – amplitude- as well as phase-gratings.

4. CONSTRUCTION OF THE MOIRÉ-DEFLECTOMETER

Detail	wavelength λ	distance L	grating period d_{opt}	angle β	open fraction
B	1550 nm	0.5 m	7.1 μm	12.969°	0.64
C	1550 nm	0.341 m	5 μm	19.395°	0.58
D	632.816 nm	1 m	5.7 μm	6.403°	0.55
E	1550 nm	0.75 m	10.6 μm	8.566°	0.77
F	632.816 nm	variable	7.9 μm	4.594°	0.66

Table 4.1: Parameters of the optical gratings for the first prototype of silicon wafers. The labeling as different details corresponds to the arrangement in figure 4.4. d_{opt} results from equations 4.1a and 4.1b, whereas β and f_{open} have been determined with GSolver [71, 72].

The limitation on these wavelengths together with the restrictions due to discrete distances L of the deflectometer lead to limited number of options for the periodicity d_{opt} of these optical gratings. With the alignment as given in figure 4.3 we find the condition to match the interferometer's geometry and the maxima of the grating's first order diffraction ($n = \pm 1$) as

$$\tan\beta = \frac{\triangle x_w}{L}, \qquad \text{and} \tag{4.1a}$$

$$\sin\beta = \frac{n \cdot \lambda}{d_{\mathrm{opt}}}, \tag{4.1b}$$

respectively. Using these two conditions we can evaluate an ensemble of grating periods d_{opt} for some distances L. The ones we have chosen for the first prototype are given in table 4.1. They provide us with a large variety for testing purposes of the deflectometer and the gratings processing methods.

Concerning the realisation of the optical gratings out of a silicon wafer, we further need to account for the thickness of the wafers, which is typically $\sim 100\,\mu$m. For such thick wafers as compared to the diffracted wavelength, the assumption of infinitissimally thin transmission gratings that leads to equation 4.1b breaks down. The propagation of the lightwave during the passage of the gratings needs to be taken into account, too. For this reason we apply the commercially available GSolver programme [71, 72] to determine appropriate open fractions of the gratings. Its algorithm is based on Rigorous Coupled Wave (RCW) Analysis [73]. Hence, using Floquet's theorem for handling the periodic structure, GSolver determines numerical solutions of Maxwell's equations. For this purpose, the programme handles the thick gratings as a series of several thin layers.

This procedure makes GSolver a very useful tool for testing the diffraction efficiencies for different grating periodicities d_{opt}, wavelengths λ, grating thicknesses and materials. The open fraction of the optical gratings of the first prototype are given in table 4.1. Using the free trial version of GSolver [71], we determined the corresponding open fractions by maximising the output O_1 and O_2 of an alignment as given in figure 4.3. In order to match the condition of equation 4.1a, the different optical gratings are arranged at the top and bottom of the first prototype of the silicon wafer.[1] The technical drawing of this prototype is given in figure 4.4. Besides the atoms' transmission grating, enlarged in detail A, and the inlays with the optical gratings (detail B-E), the vertical bars with an optical grating structure in detail F, enables the possibility to vary the distances L. In addition to this, note the vertical $5\,\text{mm}$-thick bars, that sustain the horizontal structure of the atoms' transmission grating.

4.3 The Fabrication of the Gratings

4.3.1 DRIE – Deep Reactive Ion Etching

Aiming for anisotropic etching of silicon, DRIE has been developed by F. Laermer and A. Schilp at the beginning of the 1990s [74]. This process is based on an alternating DRIE-process, which enables to control the direction and depth of the etching.

As a first step, a lithography mask is produced. This mask is positioned on the wafer such that covers the regions of the silicon that should not be etched (see figure 4.5(a)). Depending on the required precision of the structures typical masks are made out of aluminium foils or imprinted as a chrome structure on a glass plate.

For the actual etching process (see figure 4.5(b)), an inductively coupled plasma is positioned above the silicon wafer that is covered with the mask. For etching silicon wafers, a mixture of SF_6 and argon as carrier-gas is commonly used. Hence, this reactive gas leads to an isotropic chemical etching and by accelerating the ions of the plasma with applied electric fields, material can be sputtered-off the surface of the wafer. The direction of the sputtering is controllable by the direction of the electric fields.

In order to stop the isotropic etching effect, the next step is a passivation step (see figure 4.5(c)). Different gas mixtures (e. g. C_4F_8) are induced into the plasma region,

---

[1]Note that for the first testing purposes we used $6\,\text{inch}$-silicon wafers. This can be easily extended to the $8\,\text{inch}$-wafers for the setup at CERN.
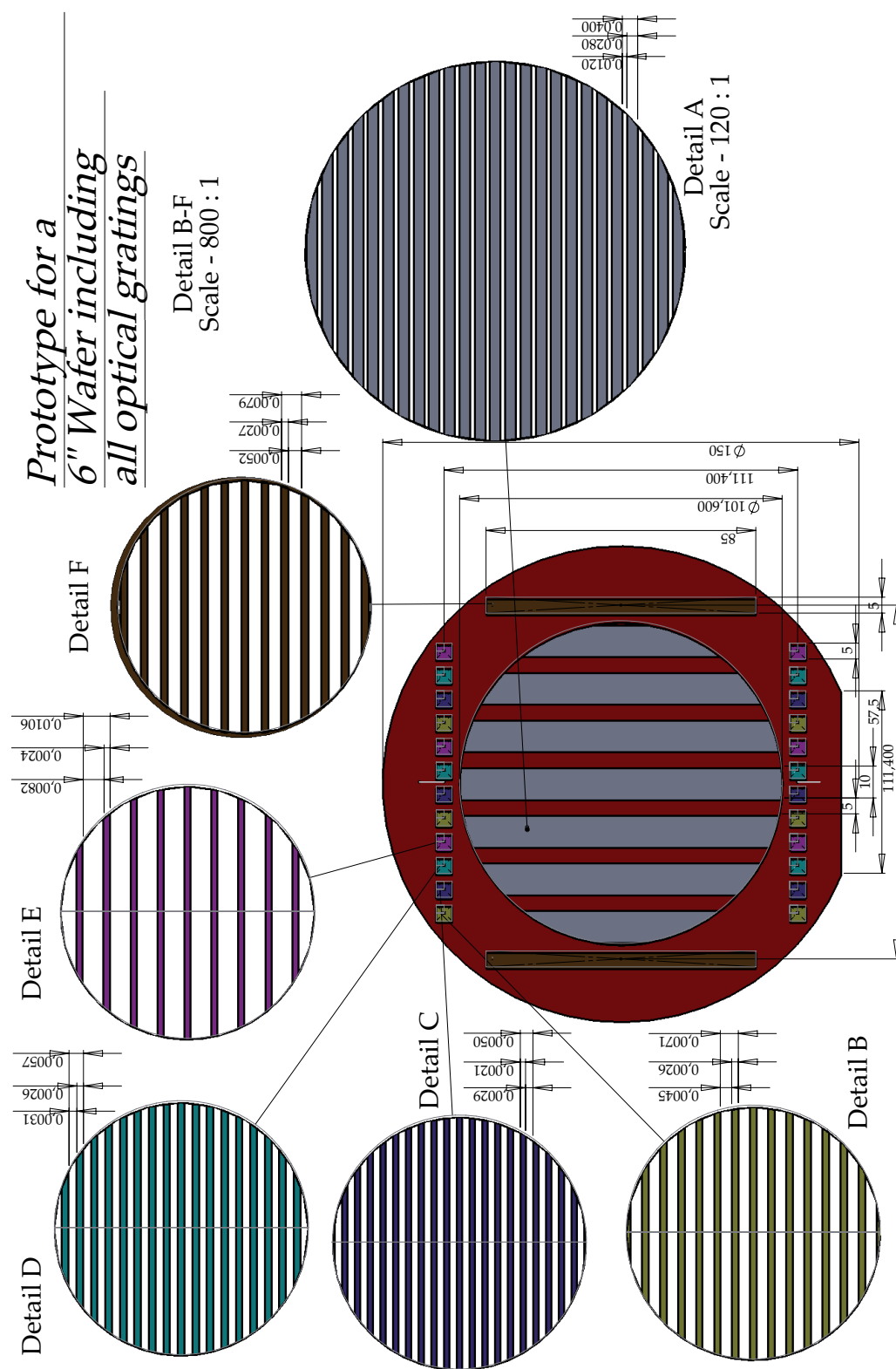
Figure 4.4: Technical drawing of the first prototype of a 6 inch-silicon wafer. The length scales are all given in units of mm.

(a) silicon covered with mask   (b) first etching step   (c) passivation step   (d) second etching step
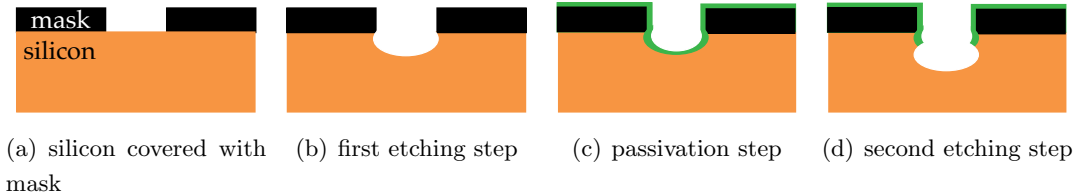
Figure 4.5: A typical Deep Reactive Ion Etching (DRIE)-process: as going from (a) to (d), these sketches show two etching steps (b) and (d), that are interrupted by a passivation step (c).

such that a particular polymer-membrane covers the entire wafer. This way, the side walls of the etched holes are protected from further chemical etching processes.

Switching back to the actual etching process (see figure 4.5(d)) with the plasma of the SF_6 and argon mixture, yields then an etching effect only in the direction, in which the accelerated ions sputter-off the passivation-membrane. The side walls remain covered and protected by the membrane.

These two processes of etching and passivation are now applied in an alternating way to the wafer. The exact etched structure can be controlled by various parameters of the etching process, as for example, the concentration of the gas mixtures, the applied voltages or the timings of the alternating process.

4.3.2 Attempts with SOI-Wafers

The final design of our first prototype given in figure 4.4 involves two catagories of structures, which are characterised by their different length scales. The first one, to which we refer to as the 'microscopic structure', includes the transmission gratings for the atoms ($d = 40\,\mu$m, $f_{open} = 30\%$) as well as the gratings for the optical Mach-Zehnder-interferometers (see table 4.1 for their details). The second structure is rather a 'macroscopic' one; it includes the support structures, i. e. the frame around the atoms' transmission gratings and the vertical bars sustaining the horizontal bars of these gratings.

Due to the large difference in length scales of the two categories of structures, the use of SOI(Silicon On Insulator)-wafers[1] has been suggested by our collaborators of

---

[1]SOI-wafers are special layered substrates. Their layered silicon-insulator-silicon structure enables a large variety of applications in microlectronics. They have been used industrially for the first time

si-layer, 100μm

siO2-layer, 2μm

si-layer, 400μm

microscopic structure

macroscopic structure

Figure 4.6: Sketch of a cross-section through a SOI-wafer. For our purposes, we use a $2\,\mu$m-thick insulator layer of silicon-oxygen, SiO_2. The 'microscopic structure' is etched into the $100\,\mu$m-thick upper silicon-layer, and the 'macroscopic structure' is etched into the $400\,\mu$m-thick bottom layer. This picture has been received from [75].

iX-factory [75]. Such a wafer consists of two silicon layers that are seperated by an insulator layer. A sketch of the cross-section through a SOI-wafer used for our purposes is given in figure 4.6. The insulating $2\,\mu$m-thick SiO_2-layer enables to process the wafer subsequently from two sides with two independent etching processes. Thus, the 'microscopic structure' can be etched before the wafer is flipped and the 'macroscopic structure' is etched into the backside of the wafer. Thereafter, the SiO_2-layer can be removed.

As first steps of this attempt with SOI-wafers, the optical masks have been manufac-

silicon

silicon oxygen

silicon

bar width = 27.18 μm

slit width = 12.59 μm
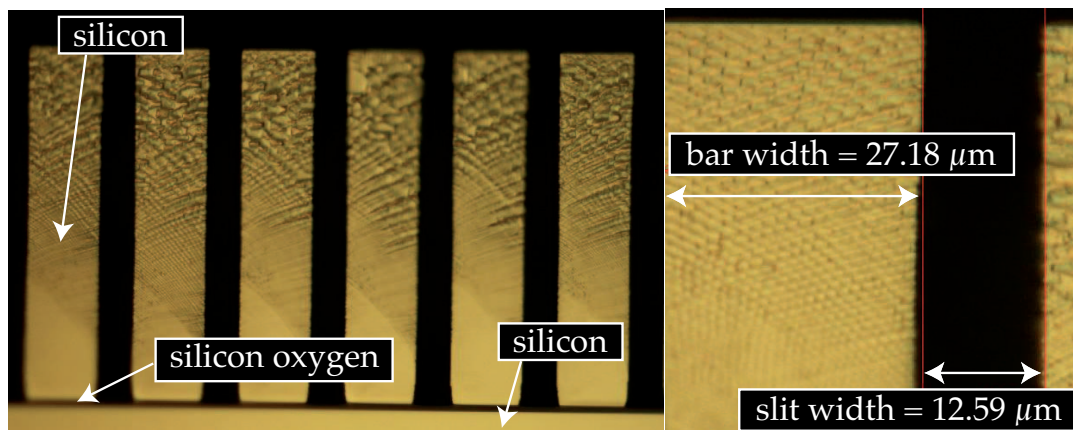
Figure 4.7: Picture of the cross-section through a SOI-wafer taken with a microscope. It shows the etching results of the atoms' transmission gratings with a desired period on $d = 40\,\mu$m and an open fraction of 30%. This picture has been taken from [75].

tured for both etching processes – one for the front side with the 'microscopic structure'

1998 [76, 77].

(a) Etching result for detail B

(b) Etching result for detail C

(c) Etching result for detail D

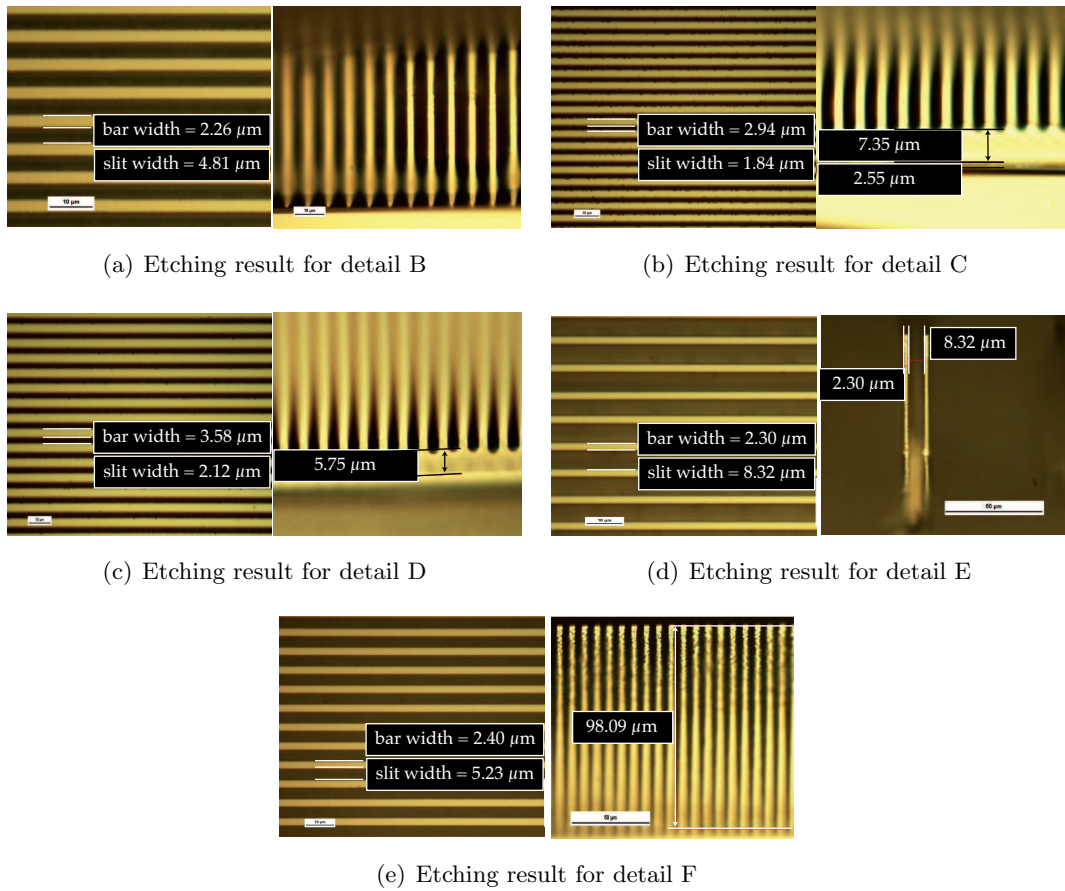(d) Etching result for detail E

(e) Etching result for detail F

Figure 4.8: Results of etching the optical transmission gratings for the different Mach-Zehnder configurations refering to figure 4.4 and table 4.1 The corresponding pictures on the left hand side show the view from above the structure, whereas the ones on the right hand side are cross-sections through the structures. Details C and D are not etched deep enough, as the etching process is saturated. These pictures have been taken from [75].

Detail	$d_{\mathrm{opt,theo}}$	measured bar width	measured slit width	$d_{\mathrm{opt,exp}}$
B	$7.1\,\mu$m	$2.26\,\mu$m	$4.81\,\mu$m	$7.07\,\mu$m
C	$5\,\mu$m	$2.94\,\mu$m	$1.84\,\mu$m	$4.78\,\mu$m
D	$5.7\,\mu$m	$3.58\,\mu$m	$2.12\,\mu$m	$5.70\,\mu$m
E	$10.6\,\mu$m	$2.30\,\mu$m	$8.32\,\mu$m	$10.62\,\mu$m
F	$7.9\,\mu$m	$2.40\,\mu$m	$5.23\,\mu$m	$7.63\,\mu$m

Table 4.2: First etching of the optical gratings in a SOI-wafer. Note the remaining silicon in detail C and D of $\sim 7\,\mu$m and $\sim 6\,\mu$m, respectively. Note the error of reading of $\pm 0.01\,\mu$m for all measured values.

and the one for the back side with the 'macroscopic structure'.

The outcome of the optimisation of the etching process is shown in figure 4.7. These pictures are taken with a microscope and show a cut through the etched atoms' transmission gratings. We find a period of $d = (39.77 \pm 0.01)\,\mu$m.

Unfortunately, using the same etching process for the optical gratings turns out to be very difficult. Realising the high aspect ratios[1] of all of these structures is difficult by itself. Using the same etching process for all grating structures over the entire area of the wafer is out of the realm of possibility for the DRIE-process. The results for the different optical gratings are shown in figure 4.8 and the measurements from the microscope are summarised in table 4.2. As the priority is set on the structure of the atoms' gratings, the optimisation of the etching process of the front side has been concluded, although the optical gratings of detail C and D (see figure 4.8(b) and 4.8(c), resppectively) could not be etched to the desired depth. Due to the saturation of the etching process[2], a silicon layer of $\sim 7\,\mu$m and $\sim 6\,\mu$m remains for these optical gratings, respectively.

Besides the described problems of etching all optical gratings to the full satisfaction, more crucial problems emerge during the etching process of the back side of the SOI-

---

[1]The aspect ratio is defined as the ratio of the slit width to the depth of the slit. In our applications the high aspect ratios require a sophisticad alternating etching process as it has been sketched in figure 4.5.

[2]Saturation of the etching process will occur if the rift in between the silicon bars are too narrow to maintain an adequate gas exchange.

wafers. The tensions, which are induced on the wafer during this etching process[1], are too strong for the $2\,\mu$m SiO$_2$-layer. It breaks up and either helium enters into the etching gas and the etching process is interrupted or the break of the SiO$_2$-layer leads to a break of the entire wafer. Even additional support bars in horizontal direction cannot increase the wafers stability.

Further attempts to etch the back side via wet etching techniques[2] were not successful. Wet etching techniques for the back side show uncontrollable additional etching of the front side and the instability of the wafer remains an unsolved problem. Nevertheless, during the attempt to find protection methods for the wafer, a new concept using simple one layer silicon wafers has been developed.

4.3.3 Attempts with Protected Si-Wafers

The $2\,\mu$m-thick SiO$_2$-layer is a severe weakness of the SOI-wafer. As it covers the entire area of the wafer, it also shares any locally induced tensions with the entire wafer, which leads to breakages of the wafer. Thus, another concept has been developed, where the DRIE-process is applied on a simple silicon wafer. Following this concept, the wafer's front side is etched as it is done for the SOI-wafers. Before etching its back side, it needs to be prepared to gain more stability. For this purpose, it is brought into contact with an additional unprocessed wafer. The latter provides the necessary stability to open the

Figure 4.9: Sketch of the results with simple Si-wafers. This picture has been received from [75].

wafer's back side. Unfortunately, as it is marked with the green shaded regions in figure 4.9, the etching process of the back side is faster at the edges of the area to be processed.[3] Thus, during this second etching process, the regions with higher etching

---

[1]For the used DRIE-process, the wafer needs to be cooled during the etching. This cooling is achieved via a helium flow from below the wafer, which induces strong tensions on the large area of the SiO$_2$-layer.

[2]The wet etching technique uses chemical solutions (e.g. potassium hydroxide (KOH) for a silicon substrate) to etch structures of typically $\gtrsim 1\,\mu$m [75].

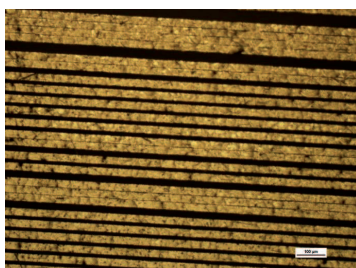[3]Note that the thick horizontal bar is only for stability reasons of these first attempts.

rates need to be covered step by step until the entire area is opened.

Besides this, the contact of the two wafers spares a thin silicon membrane that cov-
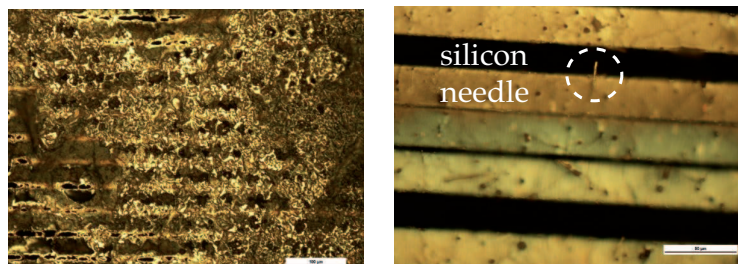
(a) the thin silicon membrane

(b) isolated silicon naddle

(c) sticking effect

Figure 4.10: Pictures that are taken with a microscope and reveal some of the problems with the Si-wafers. These pictures have been taken from [75].

ers the etched structure after removing the additional wafer again. A picture of this membrane is shown in figure 4.10(a). Further progress of this technique removed the membrane. Nevertheless, as a general issue, that does not decrease the functionality of the wafers in the Moiré-deflectometer, some isolated tiny silicon needles remain, as it can be seen in figure 4.10(b).

The worst problem, that occurs during the attempts with the protected Si-wafers, is the so-called *sticking effect*. This effect emerges on both the atoms' and the optical transmission gratings during the processing of the back side. As shown in figure 4.10(c), these effects change the gratings' periodicities locally, which will have a crucial effect on the gratings' application for our Moiré-deflectometer. In order to solve this problem, an additional support structure of vertical bars needs to be implemented to sustain and stabilize the horizontal ones. To determine the appropriate distance of these bars,

an optical testing mask has been designed. Figure 4.11 shows both optical masks; the stucture of the original chrome mask is yellow shaded and the additional testing mask is denoted with the green areas. As we aim to test different distances of the support bars over the entire wafer, the regions with different distances are distributed over the entire wafer.

The additional testing mask has been manufactured out of a aluminium foil, which is an economic alternative for testing purposes. Due to the small scale of the structures of the foil mask and the thickness of the glass layer of the chrome mask, it is not possible to put the foil mask on the top of the chrome mask. In this configuration, the structures are not mapped correctly on the wafer. As shown at the bottom of figure 4.11, this can be solved by placing the foil mask in between the chrome mask and the wafer. Unfortunately, this also leads to a snatchy mapping of the structures of the chrome mask and makes it impossible to etch the thin bars of the gratings for the Mach-Zehnder-interferometers. However, for the atom's transmission gratings, these tests have been successful. They yield additional vertical bars with a width of $2\,\mu$m and at a distance of $d_{\text{vert}} = 2\,$mm as solution against the sticking effect.

As final remark on the attempt with protected Si-wafers, note the different colour of the surface indicated in figure 4.12. Due to the mentioned different etching rates over the area of the wafer (see figure 4.9), the wafer needs to be covered step by step during the process. Depending on the time that these regions are not covered, the surface of the structure becomes modified. This modification, which looks like a 'burned' surface, becomes stronger the longer the regions are uncovered. As this effect is not removable with any chemicals it seems to be no residue of organic compounds or polymers. Consequently, we can act on the assumption that this is a purely optical effect, which does not alter the gratings performance within the deflectometer.

4.4 The First Transmission Gratings

In order to check the periodicities of the first prototypes of the transmission gratings, we make use of the optical Talbot-effect, of which a detailed derivation is given in section 2.4.1. As the main findings of that section, we remember the integer Talbot

Foil mask for testing purposes:

bar widths: 2 μm
testing the distances: d = 0.2 μm, 0.5 μm, 0.7 μm, 0.8 μm, 1 μm,
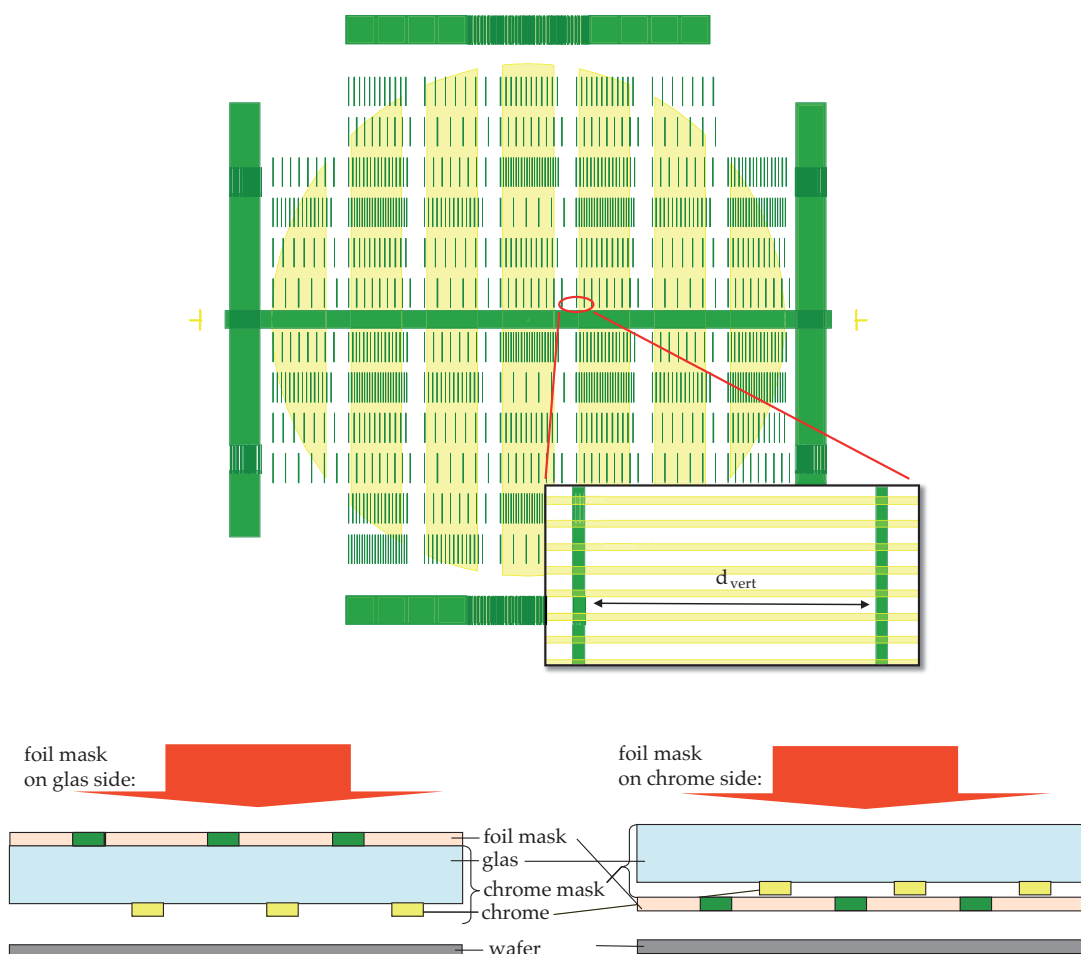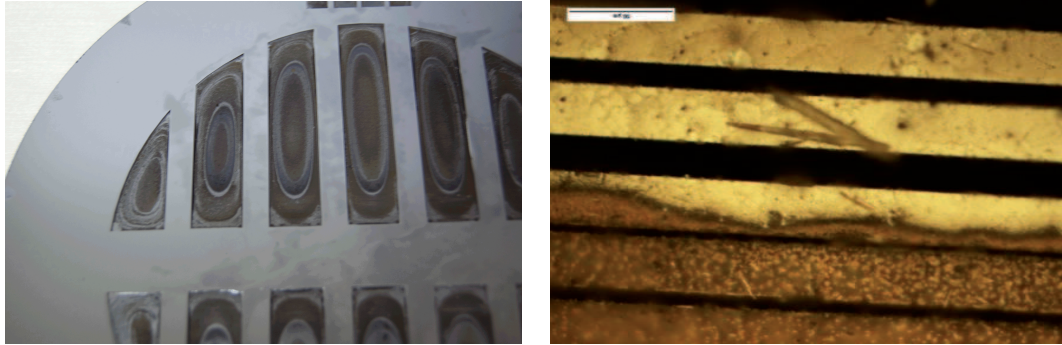1.5 μm, 1.7 μm, 2 μm, 2.5 μm,

Figure 4.11: Drawing of the last mask designs. The yellow areas denote the structrures of the original chrome mask whereas the green areas indicate the additional aluminium mask. This picture has been taken from [75].

effect being characterized by the re-image of a grating's transmission function at the

(a) Photo of the silicon wafer

(b) Microscope picture of the 'burned' surface

Figure 4.12: Pictures of a 'burned' silicon surface, where the etching process leads to an optical effect, that looks like burned material. These pictures have been taken from [75].

Talbot distance $z_T = \frac{2d^2}{\lambda}$ and its fractional correspondence at distances

$$z = \frac{n}{m} z_T, \quad \text{with} \quad \frac{n}{m} \leq 1, \text{ and } n, m \in \mathbb{N}, \tag{4.2}$$

where λ is the wavelength of the diffracted light and d denotes the period of the grating. For our testing purpose of the period d, we investigate the optical Talbot effect behind one of the gratings. Using a Helium-Neon Laser with $\lambda = 632.816$ nm, we measure the intensity distribution behind this grating by scanning vertically over it with a second one of the transmission gratings and measuring the intensity behind this second grating with a photodiode. Thus, we determine the contrast of the intensity distribution at a specific distance behind the first grating and repeat this measurement for different distances z behind the first grating. Figure 4.13 shows the data of these measurements for $z < 10z_T$. We observe maxima of the contrast at distances that correspond to any integer multiples of half the talbot distance.[1] All of the gaussian-fits to these maxima feature a quality of a R^2-value better than 0.89. Thus, referring to these fits,

---

[1]Note that although the image of the transmission function at $z = \frac{z_T}{2}$ is shifted vertically by $\frac{d}{2}$, it still has a maximum of contrast.

all distances between two adjacent peaks together yield a grating period d of[1]

$$d = (40.2 \pm 1.5)\,\mu\text{m}. \tag{4.3}$$

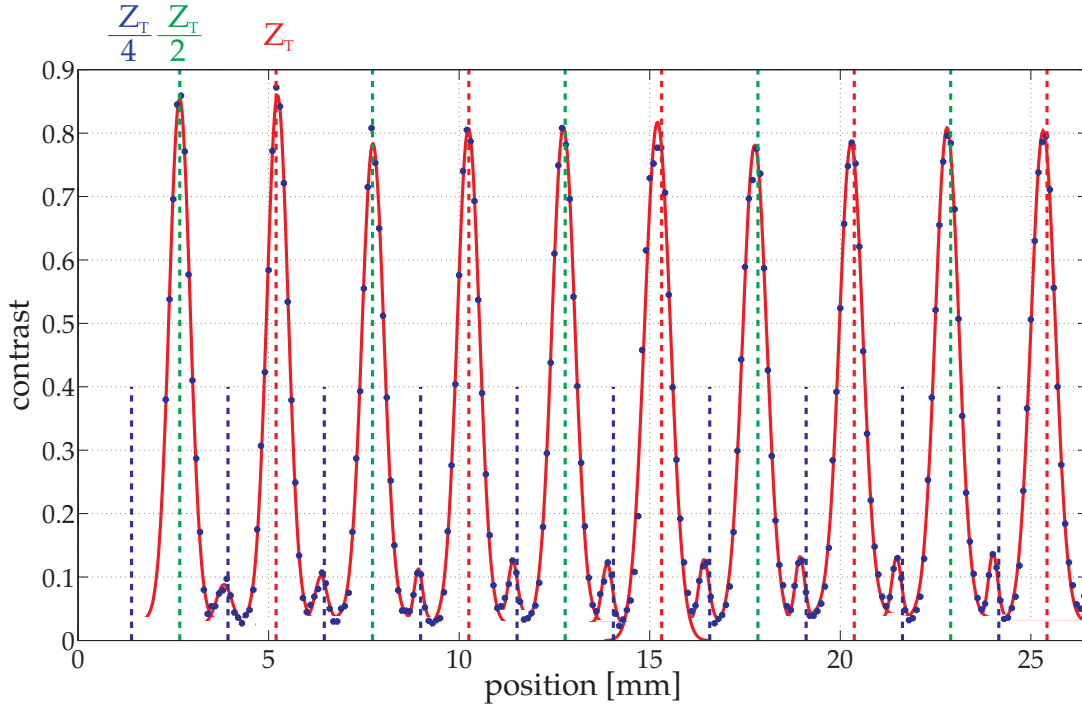The smaller maxima inbetween these large maxima refer to an amplitude distributions

Figure 4.13: Observation of the Talbot-effect behind one of the silicon transmission gratings with a Helium-Neon-Laser ($\lambda = 632.816\,\text{nm}$) and a second transmission grating as analysing tool.

at distances that correspond to odd multiples of $\frac{z_T}{4}$ (see equation 2.16). Hence, out of their distances, we find a grating period d of

$$d = (40.0 \pm 1.0)\,\mu\text{m}. \tag{4.4}$$

To sum up, our results for the grating's period agree within their errorbars and the measured mean value for d matches the demanded $40\,\mu\text{m}$ to utter satisfaction.

---

[1]As the z-positioning of the second grating has been done via a stepper motor (Encoder Mike with its controller 18011 from LOT Oriel) with a resolution of $0.1\,\mu\text{m}$, the major error in the z-axis occurs when initially mounting the translation stage of the stepper motor behind the grating. But since this determines only the absolute position on the z-axis and we examine the relative position of various multiples of the Talbot distances with respect to each other, we can neglect this error.

4.5   Mounting the Gratings

Apart from the transmission gratings, the experimental setup of the Moiré-deflectometer predominantly consists of their appropriately designed mounts. We designed special holders, to which we refer to as riders. Figure 4.14 shows one of them as an example. Made of aluminium[1], their large mass ($\sim 1\,$kg each) helps against undesired vibrations.

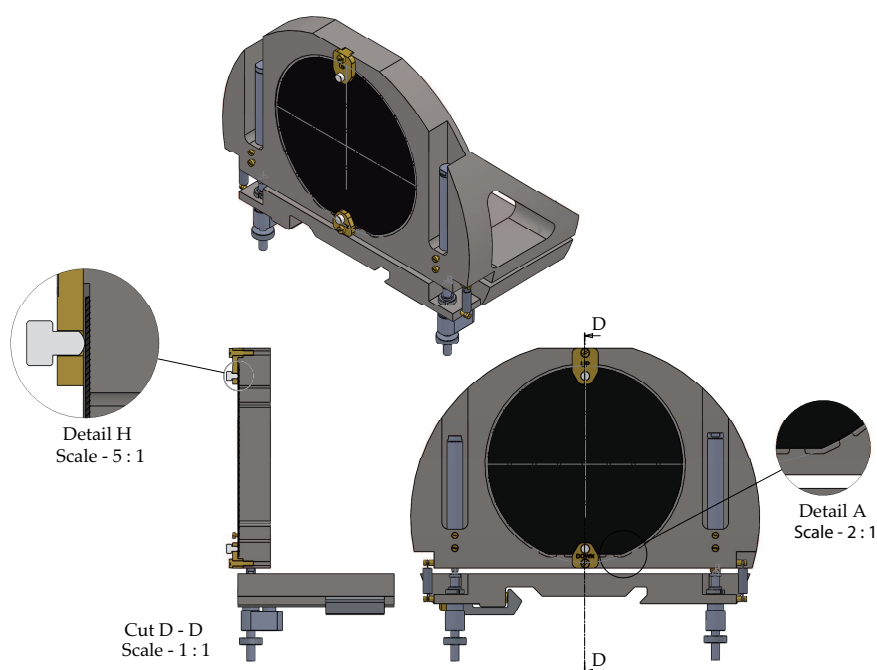As shown in the inlays of figure 4.14, the wafer is fixed against tilts and dumpings

Figure 4.14: Technical drawing of one of the riders that serve as mounts for the silicon wafers.

without excering too much tension on it. We further implemented piezo-controlled stepper motors – visible as the construction of the tubes on both sides of the wafer – to be able to adjust the gratings' alignment from outside the vacuum chamber.

Furthermore, the bottom of the riders is manufactured such that we can change the distance L for different experiments. In the first setup, a 2.5 m-long aluminium rail

---

[1] Concerning the material of the riders for the setup at CERN, we probably need to replace aluminium with a material, whose thermal expansion coefficient is closer to the one of silicon. This way, tensions due to the cryogentic environment can be minimised.

from Thorlabs (XT95 rail) is implemented. Figure 4.15 show a technical drawing of the Moiré-setup.
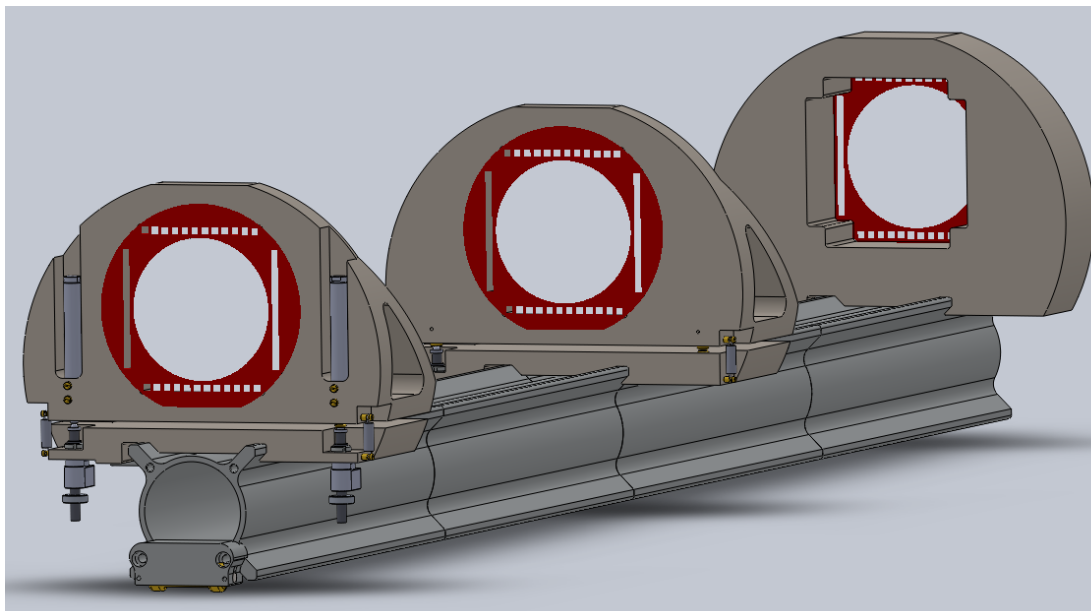

Figure 4.15: Technical drawing of the gratings (red shaded) mounted on the riders on their rail. The length of the rail is not to be scaled.

4.6 Stability of the Setup

As already described for the design of the gratings in section 4.2, we intend to monitor unwanted mechanical movements and vibrations of the Moiré-deflectometer with additional optical Mach-Zehnder-interferometers. By imprinting the gratings for these interferometers directly on the wafers, we can also use them to monitor any movements and tilts of the wafers themselves during data acquisition.

In order to quantify such movements and hence, also the stability of the system, we consider the so-called *Allan-variance* of the output signals of those interferometers. Following some parts of [64], we provide in this section a short introduction to this specific measure of stability and summarise the first stability measurements. This gives a quantitative insight into the major improvements regarding the vibration isolation. Technical details of these measurements can be found in [64].

4.6.1 Allan Variance as Measure of Stability

In order to quantify the stability of a setup, it is convenient to examine its data on (temporal) correlations. For this purpose, we make use of the so-called *N-sample variance* [78, 79, 80]. For a data set consisting of N discrete data points y_i and a temporal sampling period T, this specific variance is defined as

$$\sigma^2(N, T, \tau) = \frac{1}{N-1} \sum_{i=1}^{N} \left(\overline{y}_i - \frac{1}{N} \sum_{k=1}^{N} \overline{y}_k \right)^2, \tag{4.5}$$

where the time average $\overline{y}_i$ is calculated by

$$\overline{y}_i = \frac{1}{\tau} \int_{t_i}^{t_i + \tau} y(t) dt. \tag{4.6}$$

The timing of these considerations is determined by its period T, the data recording time τ and measurement's dead-time given by $T - \tau$.

Assuming no dead-time, i. e. $T = \tau$, and with $N = 2$, equation 4.5 reduces to

$$\sigma_y^2(\tau) = \left\langle \sum_{i=1}^{2} \left(\overline{y}_i - \frac{1}{2} \sum_{k=1}^{2} \overline{y}_k \right)^2 \right\rangle = \frac{1}{2} \left\langle (\overline{y}_2 - \overline{y}_1)^2 \right\rangle, \tag{4.7}$$

where $\langle \cdot \rangle$ represents the evaluation of the expectation value. This *two-sample variance* is also known as *Allan Variance* named after a proposition of David W. Allan [78]. The definition of this particular variance demonstrates a distinct difference to the usual variance: Instead of refering each value y_i to the mean value of all data, all y_i are considered with respect to the mean value of a small subset. With the length of these subsets τ we can determine the time scales of the examined correlations.

Plotting the Allan Variance $\sigma_y^2(\tau)$ for different τ on a double logarithmic scale provides the so-called *Allan Plots*. This illustration of the dependence of $\sigma_y^2(\tau)$ on the temporal sampling τ supplies a very useful tool for stability analysis. Thus, considering for example the Allan Plots of typical systematic effects, we find for a linear drift of the data, which is simply given by $y(t) = c \cdot t$, an Allan Variance of

$$\sigma_y^2(\tau) = \frac{1}{2} \left\langle (c \cdot \tau)^2 \right\rangle = c^2 \tau^2. \tag{4.8}$$

In contrast to this increasing line in the Allan Plot, gaussian noise on the data leads to a total different Allan Variance. It is governed by

$$\sigma_y^2(\tau) \sim \frac{1}{\tau}. \tag{4.9}$$

Hence, examining the Allan Plots can serve as a useful tool to identify the source of instability.

4.6.2 The Allan Variance of our Setup

Determination of the Allan Variance: In order to evaluate the Allan Variance of our setup, we take a measurement with the smallest possible sampling time τ_0. From there on, we could calculate the Allan Variance for integer multiples of τ_0. However, the summation in equation 4.7 can quickly become very time-consuming. For an appropriate estimation, we consider the calculation of the expectation values that involves the evaluation of the corresponding mean values $\overline{y}_i$. As these mean values become more precise the more data is taken into account, it is actually preferable to use overlapping time intervals rather than disjunct ones. For the two time sampling methods illustrated in figure 4.16(a), the corresponding Allan Plots of a test signal with gaussian noise is given in figure 4.16(b). This clearly demonstrates the improvement of the Allan Plots with overlapping time intervals as indicated with the green lines.
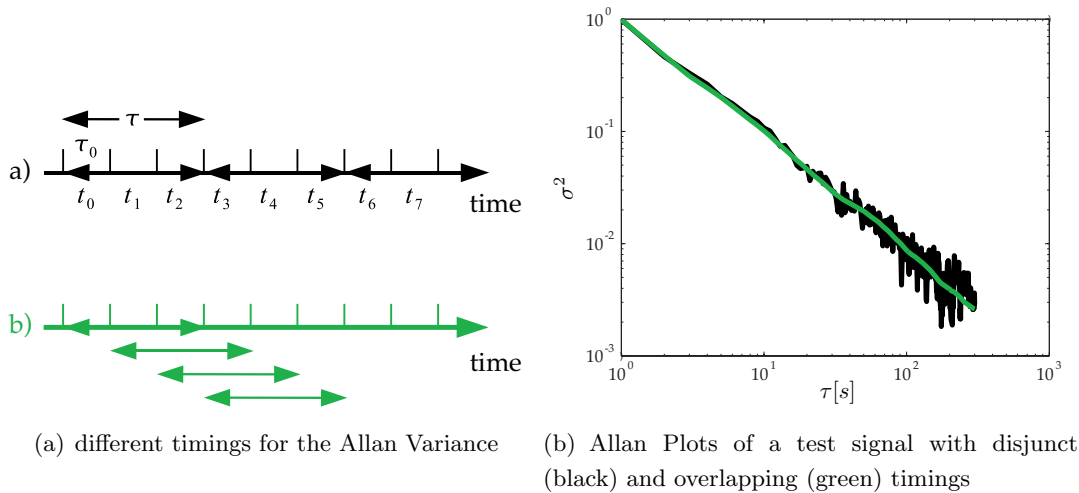

(a) different timings for the Allan Variance

(b) Allan Plots of a test signal with disjunct (black) and overlapping (green) timings

Figure 4.16: Comparing the Allan Variance for different timings of a test signal with gaussian noise. These pictures have been taken from [64].

First Stability Measurements: Using the Allan Variance as analyzing tool, we found a couple of isolation techniques that improved the deflectometers short and long term stability. Some of these techniques are e.g. flooding the table of the setup,
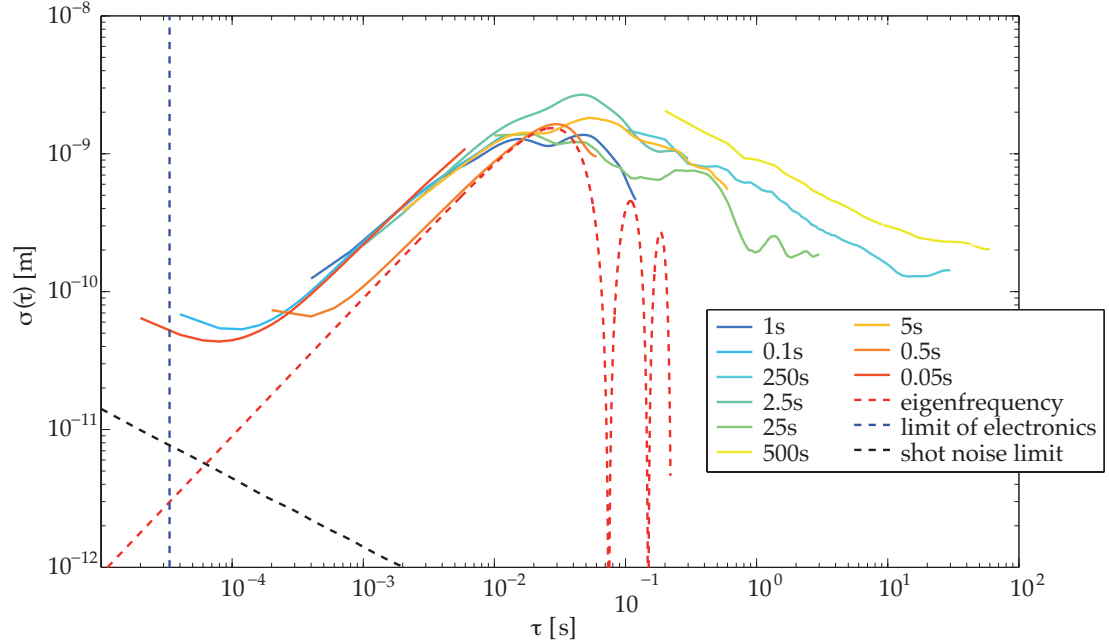

Figure 4.17: Allan Deviation of the first stability tests of the setup. For different total measurement times (see legend) the data approaches the limit of the setup's eigenfrequency and provides the best resolution at an integration time of $100\,\mu$s. This picture has been taken from [64].

hanging the rail of the deflectometer into a pendulum, evacuating the environment and stabilising its temperature. More details can be found in [64].

Particularly interesting for our application is the Allan devation $\sigma(\tau)$. The Allan Plot of this deviation not only provides us useful information about the sources of noise and drifts, it also reveals the dependence of the possible spatial resolution on the sampling time τ. Figure 4.17 shows such an Allan Plot for different total measurement times for our first setups. Note that for the plots shown in figure 4.17, all isolation techniques had been implemented, which reduced the offset of $\sigma(\tau)$ by two orders of magnitude. For the long term stability, we considering the behaviour for larger τ and observe that for all measurement times, the Allan deviation approaches the red dashed line for $1\,\text{ms} \lesssim \tau \lesssim 1\,\text{s}$. With this line, the Allan deviation of the setup's eigenfrequency of

13.4 Hz has been plotted and thus, can be clearly identified as the lower limit in this region [64, 79].

For the determination of the systems best achievable resolution, we need to examine the Allan deviation for smaller τ revealing the setup's short term stability. For this purpose, the two lower limits, the shot noise limit and the cut-off frequency of the measurement's electronics are included with the black and blue dashed lines, respectively. Concerning our measurements, we find an optimum of integration time of $100\,\mu$s, which shows an achievable resolution of about 50 pm. Although for these measurements, we decreased the noise already by two orders of magnitude by our isolation techniques, we still have not reached the shot noise limit yet. Thus, there is still room for improvements.

Chapter 5

Testing the Moiré-Deflectometer as Absolute Gravimeter

5.1   Introduction

The developement of the Moiré-deflectometer for the AE$\overline{\text{g}}$IS-experiment has been proceeded to a stage, where first gravitational measurements are possible.

This last chapter covers the two major parts of the test setup in Heidelberg: the source of metastable argon atoms and the detection technique via a Faraday cup. For the former, different types of sources are described. Hence, effusive sources in form of a DC-discharge source as well as the currently implemented inductively coupled plasma source are presented together with the necessary theoretical background of a possible future upgrade to supersonic sources. Subsequently, the technique of detection via a Faraday cup is outlined. Finally, we present in this last chapter the results of the first gravitational measurement with the Moiré-deflectometer in Heidelberg and discuss possible future improvements.

5.2   The Source

For testing purposes of the Moiré-deflectometer, the most critical property of the source is its longitudinal velocity distribution. As different longitudinal velocities lead to a different shift of the pattern at the end of the deflectometer, a considerable loss of contrast can be expected when integrating over an entire velocity distribution. Hence, the following two subsections provide an overview of different possible sources with

respect to their longitudinal velocity distribution, before the currently usable sources are described in the subsequent section.

5.2.1 Effusive Sources

Most intuitively one might think of a source of atoms in a vacuum chamber as a simple feedthrough, through which the desired atomic species can enter into the chamber. In order to control such an inlet of atoms, we need to control quantities as e.g. the pressure in the chamber, the temperature and the density of the atoms. Hence, it is convenient to fill the gas first into a container (the *reservoir*), from which the atoms can escape in a controlled way through an aperture into the vacuum.

As known from the general Maxwell-Boltzmann distribution, the velocity distribution of an atomic ensemble at temperature T is given by

$$f(\mathbf{v}) = \left(\frac{m}{2\pi k_B T}\right)^{\frac{3}{2}} e^{-\frac{m(v_x^2 + v_y^2 + v_z^2)}{2k_B T}}. \tag{5.1}$$

where the atom's mass m and its velocity $\mathbf{v} = (v_x, v_y, v_z)$ in cartesian coordinates is included. This description yields the distribution of the atom's speed $v = \sqrt{v_x^2 + v_y^2 + v_z^2}$ as

$$f(v) = \frac{4}{\sqrt{\pi}} \kappa^{-3} v^2 e^{-\frac{v^2}{\kappa^2}}, \tag{5.2}$$

where $\kappa = \sqrt{\frac{2k_B T}{m}}$ denotes the most probable velocity. Note for both of these probability distributions that they are only valid as long as there is no preferred direction of the atom's movement and *Brownian Motion* dominates the dynamics of the atoms.

Considering the distribution behind the aperture, through which the atoms escape from the reservoir into the vacuum, only atoms with velocity components $v_z \neq 0$ contribute, i.e. a 'directional flow' is formed shortly behind the aperture. Assuming that neither the spatial nor the velocity distribution inside the reservoir changes due to the escaping atoms and that these atoms do not change their velocities as they pass the aperture (the so-called *thin-wall-condition*) the velocity distribution can be expressed in spherical coordinates by

$$f(v, \theta) \propto \kappa^{-3} v^3 e^{-\frac{v^2}{\kappa^2}} \cos\theta, \tag{5.3}$$

with θ providing the direction with respect to the beam axis and the speed v of the atoms. Note the additional speed v as compared to equation 5.2. This contributes the fact that any fast moving atoms pass the aperture more often than slower ones. Hence, it is more probable for them to leave the reservoir and the number the atoms that leave the reservoir through the aperture is proportional to their speed v [81]. Measuring the velocity distribution far behind the source, i. e. $\theta \longrightarrow 0$, yields the longitudinal velocity distribution of such an effusive source as

$$f(v) \propto \kappa^{-3} v^3 e^{-\frac{v^2}{\kappa^2}}. \tag{5.4}$$

The assumption made above that the atoms that leave the reservoir do not change their velocity distribution is significant for the validity of the distribution. It demands a negligible collision rate of the atoms during their passage through the aperture. Thus, not only does the source need to be thin-walled, the atomic mean free path λ_{res} in the reservoir also needs to be very large as compared to the diameter D of the aperture, i. e. $\lambda_{\text{res}} \gg D$. The resulting effusive atom source is often realised with small pressure gradients between the reservoir and the vacuum chamber.

5.2.2 Supersonic Sources

Besides the described effusive source, another type of atomic source is widely used: the supersonic source [81, 82, 83]. This type features an interesting longitudinal velocity distribution, which results from the dynamics of the atoms during and right after their passage through the aperture.

One way to realise such a type of source is to increase the pressure gradient between the reservoir and the expansion. At a gradient, where the atomic collision rate during the passage through the aperture is high enough to maintain a continuum flow, a supersonic expansion can become observable.

Assuming this process of expansion to be adiabatic, the system's dynamics can be described via the conservation of the enthalpy H. For an ideal gas the enthalpy is defined as

$$H = C_p T = \frac{5}{2} k_B T \tag{5.5}$$

with T being the temperature of the gas. During the passage through the aperture and the following expansion[1], the high collision rate leads to a continious conversion of the

---

[1]Note that this supersonic expansion of atomic beams is often referred to as *free jet expansion*.

5. TESTING THE MOIRÉ-DEFLECTOMETER AS ABSOLUTE GRAVIMETER

stagnation enthalpy H_0 of the atoms into kinetic energy of the directional flow. This adiabatic process can be described by

$$H_0 = H_{e,\text{rest}} + \frac{1}{2}mu^2, \tag{5.6}$$

where the rest enthalpy of the atoms is denoted as $H_{e,\text{rest}}$ and the directional flow in beam direction is determined by its speed u. For an ideal gas the stagnation enthalpy becomes then[1]

$$H_0 = \underbrace{\frac{5}{2}k_B T_0}_{\text{enthalpy of the reservoir}} = \underbrace{\frac{5}{2}k_B T}_{\text{rest enthalpy in thermal energy}} + \underbrace{\frac{1}{2}mu^2}_{\text{kinetic energy of directed flow}}, \tag{5.7}$$

which can be rewritten using equation 5.5 as

$$C_p T_0 = C_p T + \frac{1}{2}mu^2. \tag{5.8}$$

With the speed of sound $c = \sqrt{\gamma \frac{k_B T}{m}}$ and $\gamma = \frac{5}{3}$ for an ideal gas, a measure for the degree of conversion of enthalpy into kinetic energy is defined by the Mach number

$$M_a \equiv \frac{u}{c}. \tag{5.9}$$

Using this measure, we can rewrite equation 5.7 as temperature ratio

$$\frac{T}{T_0} = \left(1 + \frac{1}{2}(\gamma - 1)M_a^2\right)^{-1} \tag{5.10}$$

As long as a high collision rate is maintained, the conversion of enthalpy into the directed flow continues. Note for this conversion process that not only does the directed flow u increase, the local speed of sound c decreases simultanously. Hence, M_a increases with increasing distance from the source. However, as the temperature and simultaneously the density goes down with increasing distance, the decreasing collision rate slows down the growth of M_a. At a critical distance, which is called the *Quitting Surface* [82], the conversion stops entirely, such that the longitudinal velocity should remain constant. This has been shown by kinetic models [81] as well as Monte Carlo

---

[1]Concerning the term $\frac{5}{2}k_B T$, note that this consists out of the thermal energy $\frac{3}{2}k_B T$ of the atom, which can be assumed to be randomly distributed in the atom's reference frame, and the thermal energy $k_B T$ of the gas, which yields the gas' espansion [84].

Simulations [81].[1]

For many applications – as for testing purposes of the Moiré Deflectometer – it is reasonable to use the axial symmetry of the beam and describe the velocity distributions via a transversal v_t and a longitudinal v_z velocity component. Assuming a seperability of the two distributions, we find for the described directional flow of a supersonic source a velocity distribution in transversal direction given by [82]

$$f(v_t) \propto C_t e^{-\frac{m}{2k_B T_t} v_t^2},$$
(5.11)

a gaussian distribution governed by the transversal temperature T_t and the normalisation constant C_t. In contrast to this transversal component, the corresponding longitudinal distributions is strongly influenced by the directional flow. It is given by

$$f(v_z) \propto C_z v_z^3 e^{\left(-\frac{v_z - u}{\kappa_z}\right)^2} = C_z v_z^3 e^{\left(-\frac{v_z - cM_a}{\kappa_z}\right)^2},$$
(5.12)

where the normalisation constant is denoted by C_z. Particularly interesting becomes the comparison of the supersonic longitudinal distribution to the one of an effusive ones (equation 5.4): the longitudinal velocity distributions of supersonic beams are narrower and shifted to higher mean values. This is also illustrated in figure 5.1, where typical distributions are plotted for different Mach numbers M_a and an effusive source.

As mentioned above, the longitudinal velocity distribution is the most critical property of a source for the Moiré-deflectometer. The broader this distribution, the more does the pattern at the end of the deflectomter smear out. Hence, it seems to be preferable to use rather a supersonic source. The gain of contrast becomes apparent in figure 5.2, which shows results of our Monte-Carlo simulations of the setup in Heidelberg. Note that with an effusive source we can only expect a contrast of $C = 0.3$ (see figure 5.9(b)). The gain of contrast for the here simulated two-grating setup when increasing the measure of supersonic flow M_a is striking and suggests an upgrade of the currently used effusive source to a supersonic one in future experiments[2].

---

[1]Note that any collisional processes with the background gas have been neglected here. They lead to the formation of shock waves that provide further limits to the supersonic expansion. For more details on supersonic sources refer to [81, 82, 83, 84, 85].

[2]Note that the two-grating setup has been chosen here for illustrative reasons only. Scanning the third grating over the pattern will decrease the contrast even further.
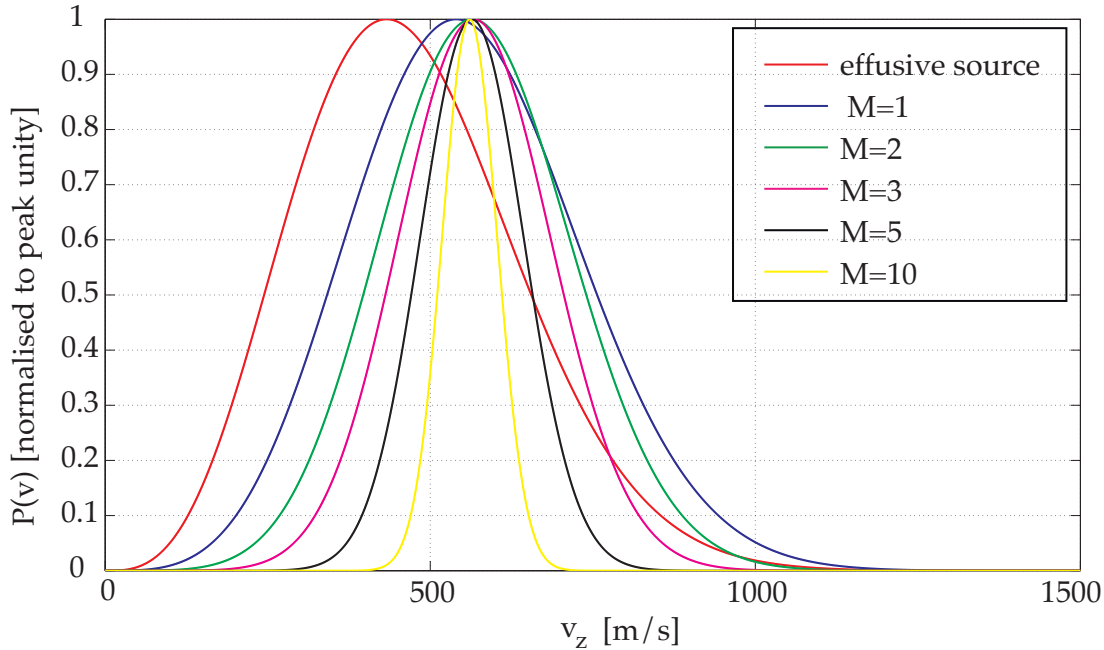
Figure 5.1: Typical longitudinal velocity distributions of different supersonic beams and an effusive beam.

5.2.3   The Current Ar*-Source

The current atomic source has been built out of the remainings of former experiments of our group in Heidelberg [53, 86]. They used a source of metastable argon that is based on a direct current (DC) glow discharge. As schematically shown in figure 5.3(a), electrons are ejected from the cathode, which is formed as thin naddles, and subsequently, accelerated towards the first anode, a grounded disk. An appropriate pressure within the argon reservoir yields a glow discharge that produces metastable argon atoms in the $1s_3$- and $1s_5$-state (see figure 3.1). To enhance the number of metastable atoms, the interaction region between the argon atoms and the emitted electrons is increased via a second anode, that attracts the electrons. This possibility of increasing the fraction of metastable atoms is one of the advantages of this type of source. Another very interesting advantage for cold atom experiments, is the pre-cooling option of the argon gas via a cooling tank that surrounds the reservoir. However, the designed DC-source supplies only $\sim 1 \cdot 10^{12} \frac{\text{atoms}}{\text{s} \cdot \text{sr}}$. In order to reach a high sensitivity of the Moiré-deflectometer, we need to increase the atomic flow. For this purpose, we
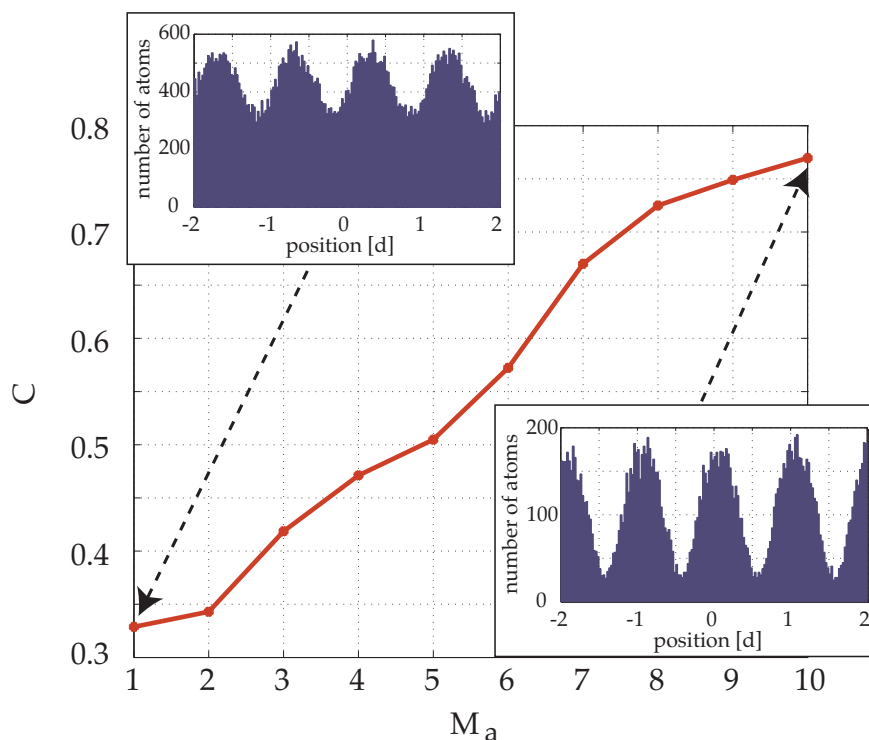
Figure 5.2: The gain of contrast C of a two-grating Moiré-setup in Heidelberg when increasing the Mach number M_a of a supersonic source ($L = 1\,\mathrm{m}$).

upgraded the setup and implemented an inductively coupled plasma source[1], which is able to provide up to $\sim 3 \cdot 10^{14} \frac{\mathrm{atoms}}{\mathrm{s \cdot sr}}$ [56, 88].

For such an inductively coupled plasma source, we use a glass tube as the atomic reservoir similar to the one that surrounds the cathode in the DC glow discharge source. As sketched in figure 5.3(b), a radio frequency of a helical coil around the glass tube can couple energy into the reservoir and discharge a plasma inside the tube. For this discharge to occur the density of the argon atoms as well as an efficient coupling between the coil and the argon reservoir is essential. This coupling can be optimised by the geometry of the coil, the radio frequency[2] and the reservoir pressure. Increasing the production rate of metastable atoms can be achieved with higher RF-power [88]. Hence, we can optimise the flow of metastable atoms by matching the impedance of

---

[1]Further details on inductively coupled plasma sources of argon can be found in [87].
[2]In order to use common RF-components, we have chosen $144\,\mathrm{MHz}$ for our input signal of $\sim 35\,\mathrm{W}$.

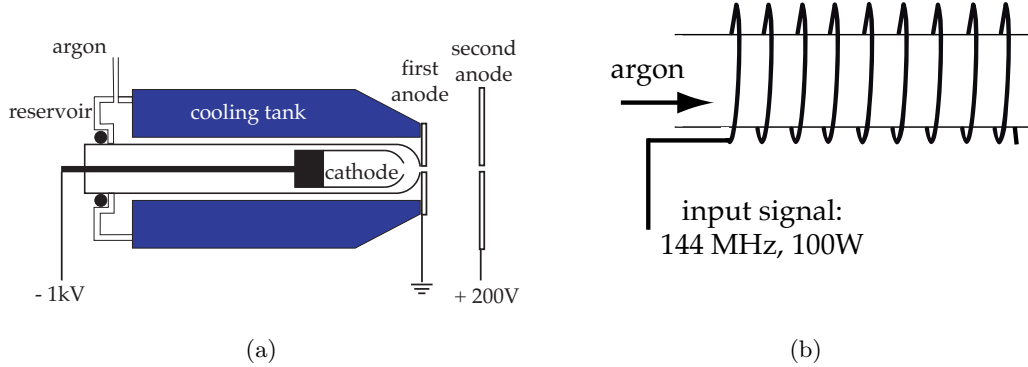(a)   (b)

Figure 5.3: Schemes of the two Ar*-sources: (a) the old one based on DC glow discharge
and (b) the new one based on an inductively coupled plasma.

the RF-input to the coil. Fine adjustments of this impedance matching can be done
via commercially available impedance matching devices[1]. A photo of this source in
operation is given in figure 5.4.

As denoted above, the velocity distributions
of the source are particularly interesting for the
tests of our deflectometer. Figure 5.5 and 5.8(b)
show the corresponding transversal and longitu-
dinal distribution of the Ar*-atoms in the $1s_5$-
state 30 cm behind the currently used source.
These profiles have been measured via light-
induced fluorescence of the atoms – a method
based on the photon emission of atoms that are
exposed to a resonant laser beam. The closed

Figure 5.4: Photo of the plasma
source

transition, that is used for this method, is the $1s_5 \rightarrow 2p_9$ ($J = 2 \rightarrow J = 3$), which
corresponds to a wavelength for the laser beam of $\lambda = 811.754$ nm (see figure 3.1).
For this fluoresence method we need to scan the laser's frequency over the atomic res-
onance. Thus, the atoms' transversal velocity distribution can be directly observed by
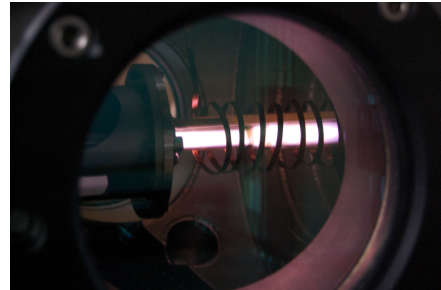monitoring the intensity of the photons that are emitted by the excited argon atoms.

---

[1]For the chosen frequency of 144 MHz we use a MFJ Dual Band Tuner (Model 921) in between
the input signal and the coil. This allows us to optimise the performance of the source during the
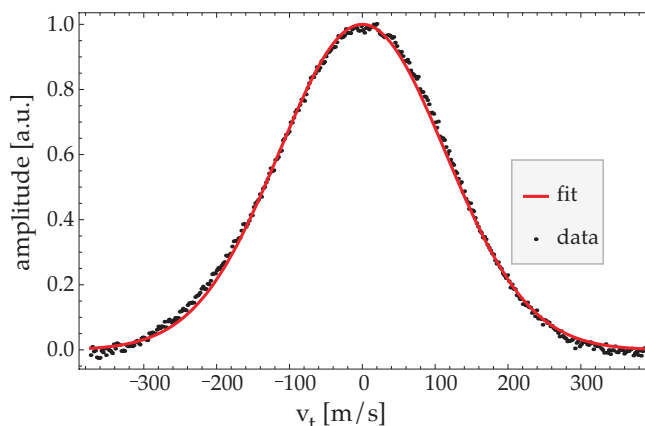experiments.

Figure 5.5: The transversal velocity distribution out of the fluorescence signal of orthogonally crossing laser- and atom beams.

Essential for this measurement is a careful alignment of the laser beam orthogonal to the atomic beam. This way, the captured fluoresence signal of their crossing region is not sensitive on the longitudinal velocity component v_z of the atoms and an appropriate fitting (denoted with the red solid line) of the fluorescence data of figure 5.5 provides us the transversal mean velocity [56]

$$\overline{v}_t = 269 \, \frac{\mathrm{m}}{\mathrm{s}}. \tag{5.13}$$

For the longitudinal velocity distribution, we need to include the z-component into our measurement. By aligning a second laser beam with an angle α in between the two laser beams (see figure 5.6), we receive a fluorescence signal that shows a large peak representing the signal from the orthogonal aligned beam and a second broader peak that shows the signal from the angled beam, which includes the longitudinal velocity component. This data can be extracted. It is plotted in figure
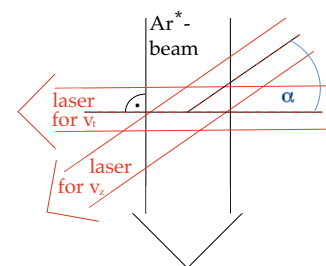

Figure 5.6

5.8(b) and its fit provides useful values as the longitudinal mean velocity, for example. For a correct determination of this fit and thus, the atomic longitudinal mean velocity, we need to account for an effect that occurs due to the capture region of the measurement. This becomes clear by remembering that the common Maxwell-Boltzmann
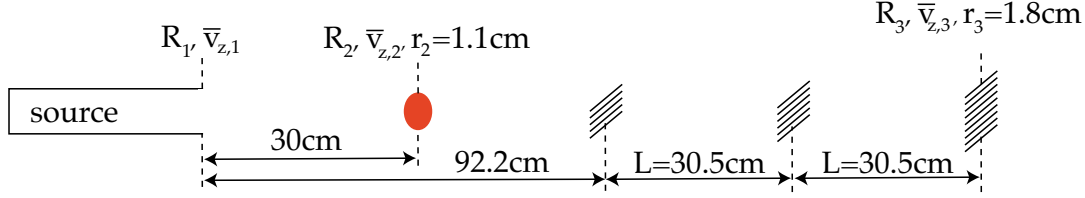
Figure 5.7: Sketch of the setup for the velocity measurements and the first Moiré-setup.

velocity distribution refers to a gas without preferred direction. Hence, it is, strictly speaking, only valid within or maybe just directly behind the source, at point R_1 in figure 5.7. As the fluorescence measurement of figure 5.8(b) is taken at point R_2, 30 cm behind the source, we need to consider the restriction of this geometry. In general, a limited radius r of the capture area of the measurement at the distance R from the source leads to

$$\frac{|v_t|}{|v_z|} \geq \frac{r}{R}, \qquad \Rightarrow \qquad -\frac{r}{R}|v_z| \geq v_t \geq \frac{r}{R}|v_z|, \tag{5.14}$$

which limits the measurable velocity components v_t and v_z in transversal and longitudinal direction, respectively. For the transversal component, this condition yields a limitation of the integration of the velocity distribution. Thus, the transversal velocity measures are determined by

$$\int_{-\frac{r}{R}|v_z|}^{\frac{r}{R}|v_z|} f(v_t)dv_t. \tag{5.15}$$

Solving this integration with the error-function $\text{erf}(x)$[1], we note its interpretation with $\text{erf}\left(\frac{n}{\sigma\sqrt{2}}\right)$ being the percentage of the atoms within the nth-σ environment. This way, we can determine the factor, by which the measured longitudinal velocities are conditioned. The correct distribution that accounts for the limited capture region of a measurement at distance R from the source is then given by

$$f_{\text{corr}}(v_z) = f(v_z) \cdot \text{erf}\left(\frac{\frac{r}{R}v_z}{\sigma\sqrt{2}}\right), \tag{5.16}$$

with $\sigma = v_t$. The data of figure 5.8(b) corresponds to a measurement capturing an area with radius $r_2 = 1.1$ cm at distance $R_2 = 30$ cm. Applying equation 5.16 to this data, we can evaluate the distributions at position R_1 and R_3 and with $r_3 = 1.8$ cm

---

[1]The error-function is defined as $\text{erf}((x) = \frac{2}{\sqrt{\pi}} \int_0^x e^{-t^2} dt$ and it is known that for a normal distribution $\text{erf}(\frac{n}{\sqrt{2}})$ provides all values within n standard deviations σ [89, 90].

(a) $f(v_z)$ calculated at R_1 (b) $f(v_z)$ measured at R_2 (c) $f(v_z)$ calculated for R_3
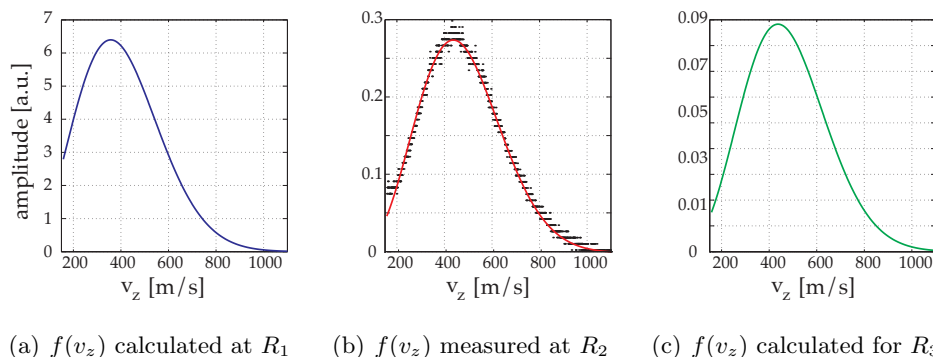
Figure 5.8: The longitudinal velocity distribution measured at (b) R_2 via fluorescence and calculated at (a) R_1 and (c) R_3. The corresponding mean velocities are (a) 419 $\frac{\text{m}}{\text{s}}$, (b) 476 $\frac{\text{m}}{\text{s}}$ and (c) 479 $\frac{\text{m}}{\text{s}}$. Note the different scales of the $f(v_z)$-axis.

(see figure 5.7). The corresponding mean velocities become $\overline{v}_{z,1} = 419\,\frac{\text{m}}{\text{s}}$, $\overline{v}_{z,2} = 476\,\frac{\text{m}}{\text{s}}$ and $\overline{v}_{z,3} = 479\,\frac{\text{m}}{\text{s}}$. Thus, the mean longitudinal velocity within the deflectometer can be approximated by the mean of $\overline{v}_{z,2}$ and $\overline{v}_{z,3}$; we find

$$\overline{v}_z = 477.5\,\frac{\text{m}}{\text{s}}. \tag{5.17}$$

In order to examine the effect of our effusive source on the output of the current deflectometer setup with $L = 0.305\,\text{m}$, our Monte-Carlo simulations yield a contrast of our three-grating setup of ~ 0.8 . Comparing this result for the same number of particles but for the planned $L = 1\,\text{m}$, which is shown in figure 5.9, the loss of contrast for the future setup becomes clearly visible. We can only expect a contrast of ~ 0.1. Due to this huge difference between the contrasts, one might think that the short distances L between the gratings is of andvantage. Nevertheless, the figure of merit for the Moiré-deflectometer is still the minimal resolvable acceleration g_{min} (see section 2.7.2) which scales as

$$g_{\text{min}} \propto \frac{1}{CL^2}. \tag{5.18}$$

Hence, although the contrast is much worse for $L = 1\,\text{m}$, the gain for this setup is still given by

$$\frac{g_{\text{min}}\big|_{L=1\,\text{m}}}{g_{\text{min}}\big|_{L=0.305\,\text{m}}} \approx 1.3. \tag{5.19}$$

5. TESTING THE MOIRÉ-DEFLECTOMETER AS ABSOLUTE GRAVIMETER
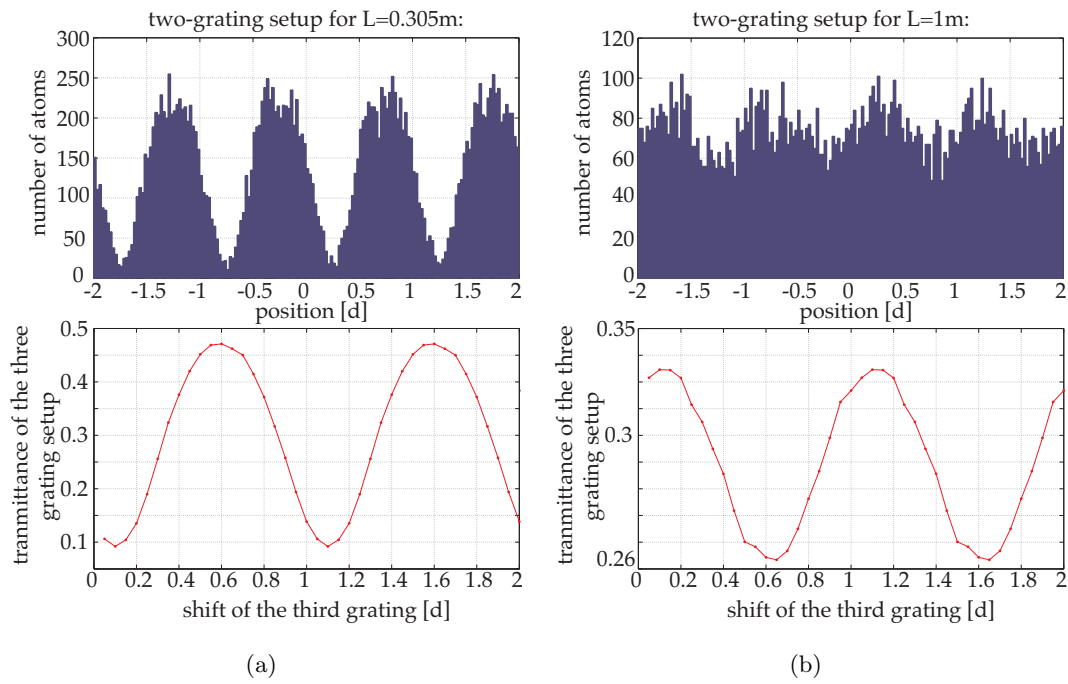

(a)   (b)

Figure 5.9: Results of the Monte-Carlo simulations for the setup in Heidelberg, including the longitudinal velocity distribution of the currently implemented source for (a) $L = 0.305$ m corresponding to the current measurements and (b) $L = 1$ m, planned in future setups. The upper plots show the pattern of a two grating setup and lower plot the output signal when scanning the third grating. They provide a contrast of (a) $C = 0.9$, (b) $C = 0.3$ for the two-grating setup and (a) $C = 0.8$, (b) $C = 0.1$ for the three-grating setup.

5.3 The Detection via a Faraday Cup

Measuring the atomic flow via a Faraday cup is based on the release of an electron out of a metallic surface, when a metastable atom is approaching or hitting onto this surface. Characterised by the work function of the metal ϕ and the ionisation energy of the atom E_{Ion}, there are two physical concepts that can cause such an electron emission [91, 92, 93].

Resonant Ionisation and Auger-neutralisation The sketch in figure 5.10(a) shows the situation of a metastable argon atom that approaches the metallic surface. Assuming a free state in the metal that is further also resonant with the state of the excited argon electron, we find the possibility that the two wavefunctions of the excited electron and the electrons in the metal overlap for a sufficiently long time for tunneling to occur. Hence, as indicated with (1), the argon's excited electron tunnels into the metal and as denoted with (2), the ionised argon atom becomes neutralised by an electron of the metal's surface that tunnels in turn into the ground state of the argon atom. The energy release of this process is transferred (at least partially) to kinetic energy of an electron in the metal, which can then leave the surface.
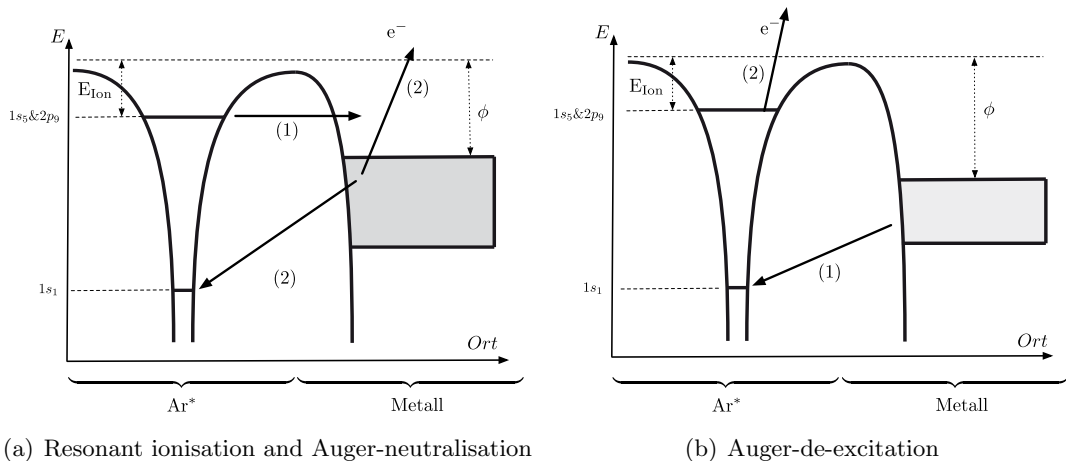

(a) Resonant ionisation and Auger-neutralisation   (b) Auger-de-excitation

Figure 5.10: The two concepts that lead to a the electron emission of the Faraday cup. The graphs are taken from [56].

5. TESTING THE MOIRÉ-DEFLECTOMETER AS ABSOLUTE GRAVIMETER

Auger-de-excitation Figure 5.10(b) provides a sketch of the situation of an approaching metastable argon atom when no resonant state in the metal is available[1] or the ionisation energy E_{Ion} is simply too large for the described Auger-neutralisation to occur. In this case, a release of an electron out of the metal's surface is still observable. For this purpose, the argon atom needs to approach very close to the surface such that one of the metal's electrons can tunnel into one of the unoccupied states of the argon atom. This tunneling is indicated in figure 5.10(b) with (1) and leads to an energy transfer to the valence electron of the argon atom. Hence, this electron is released as denoted by (2). For both concepts, the energy of the release electron is of the order of $E_{\text{Ar}^*} - \phi$ and it can be expected that the argon atom is de-excited after its first hit on the metallic surface [94, 95].

For our detection purposes, the efficiency ρ_{eff} of the electron-emission depends the chosen metal, its temperature as well as on the atomic species. Particularly efficient is a surface of polished stainless steel with a efficiency of $(4 - 22)\%$ [92].

The setup of the detection with the Faraday cup that we used is shown in figure 5.11

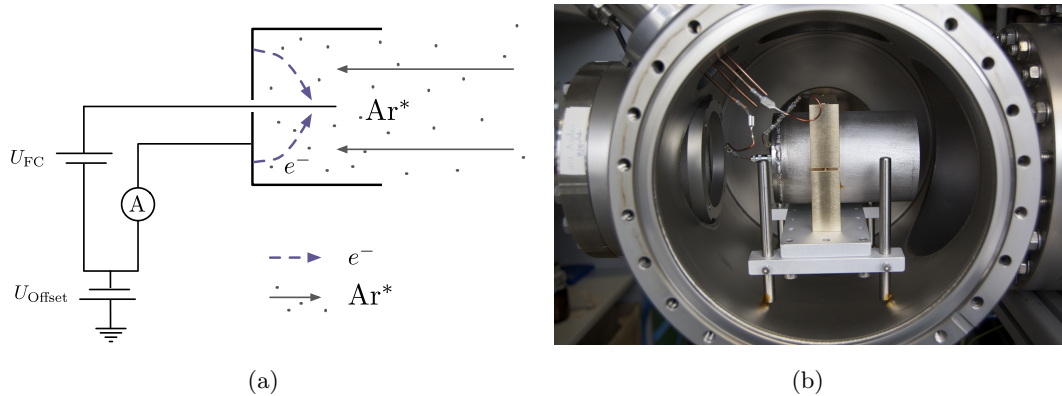(a)   (b)

Figure 5.11: The Faraday cup: 5.11(a) sketch of its concept and 5.11(b) photo of it in the open vacuum chamber. These pictures are taken from [56].

together with a photo of it. As soon as electrons become emitted of the inner surface of the cup, a current I_{FC} can be measured by the ampère-meter A. This current can

---

[1]Note that any small contaminations of the metal's surface can lead to a shielding of the metal's inner structure. Such a shielding can avoid any interaction between the argon's and the metal's electrons. Consequently, no tunneling between resonant states can occur.

be expressed in atomic flow $\frac{dN}{dt}$ by

$$I_{\text{FC}} = e\rho_{\text{eff}}\frac{dN}{dt},\tag{5.20}$$

where the elmentary charge e is included. A detailed characterization of our Faraday cup can be found in [56].

5.4 The First Gravitational Measurements

For the first runs with the Moiré-deflectometer, we use a grating setup as it is sketched in figure 5.7. Note that due to the fragility of the current wafers, we use small cutouts of the grating structure. Their periodicities have already been tested via the Talbot-effect of light (see section 4.4).

Apart from the metastable argon atoms[1], our plasma source additionally emits a lot of photons originating from the atoms' decay processes in the plasma. These photons provide us a pattern that is not shifted by gravity. Hence, their pattern serves as ideal reference signal for the absolute fringe shift caused by of the gravitational acceleration g. Assuming no disturbing magnetic or electric fields (see chapter 3), we can retrieve the absolute shift of the pattern of the argon atoms that is induced by gravitation by comparing their pattern to the pattern of the photons.

In order to extract the atoms' signal from the total one, we pulse a laser into the atomic beam. With this laser of wavelength $\lambda = 801.699\,\text{nm}$, we quench the metastable atoms to the ground state[2]. Note that the Faraday cup is 'blind' for atoms in the ground state and with the laserlight on, the Faraday cup only measures the signal of the photons. Hence, we can take an 'alternating measurement', switching between one with the $1s_5$-atoms and the one without them.

By monitoring the signal of the Faraday cup behind a three-grating setup, we observe then a shift $\triangle\phi_g$ between the two signals. This shift can be used in

$$\frac{\triangle x_g}{d} = \frac{\triangle\phi_g}{2\pi},\tag{5.21}$$

---

[1] Note that the emitted argon atoms populate (or decay quickly to) both metastable states – the $1s_3$- and $1s_5$-state. Nevertheless, the number of atoms in the $1s_5$-state, that we use, dominates the output of the source [96, 97, 98, 99]. The additionally emitted charged particles as ions and electrons are neglected here. With their uncontrolled velocity distributions and possible deflecting electric fields, they are accounted for as additional loss of contrast.

[2] See figure B.1 of Appendix B.

where d represents the grating period and $\triangle x_g$ the spatial vertical shift due to gravitation that is observable within one period. Thus, for a deflectometer without disturbing forces, we can determine an absolute value of g using

$$\triangle x_g = -gT^2, \qquad \Rightarrow |g| = \left| \frac{\triangle x_g}{T^2} \right| = \left| \frac{\triangle x_g}{L^2} \overline{v}_z^2 \right| \qquad (5.22)$$

The following paragraphs outline the factors that can limit this measurement method substantially.

Determination of the Time of Flight T

Concerning the time of flight T of the atoms, the most critical value is the longitudinal mean velocity $\overline{v}_z$. As shown in section 5.2 we need to account for a whole distribution. The resulting loss of contrast of the output pattern of the deflectometer can be minimized by a supersonic source (see figure 5.2), which might be implemented in the future.

Determination of the Absolute Shift $\triangle x$

For the measurement of the two signals of the metastable argon atoms and the photons, we measure the pattern at the end of the deflectometer with a continiously running source.

The absolute shift is retrieved by scanning the output pattern of the deflectometer alternating with and without the $1s_5$-atoms. Comparing the data of the two resulting signals of the same scanning slopes, we find the signal given in figure 5.12. The upper plot shows the signal of the photons. Here, the data of the Faraday cup current is denoted with blue points including their statistical errors. Each of them is averaged over 50 scanning ramps. The fit of this signal, a sin-function with a linear offset is plotted with the red line and can be compared with the fit of the atoms' signal provided in the bottom plot of figure 5.12. This signal has a much smaller signal-to-noise-ratio, such that the error bars are clearly visible. Calculating the phase shift between these two fits leads to a an absolute value of

$$g = (9.5 \pm 1.9) \, \frac{\text{m}}{\text{s}}. \qquad (5.23)$$

The following paragraphs provide the calculation and discussion of the error of this measurement with regard to improvements for future runs.
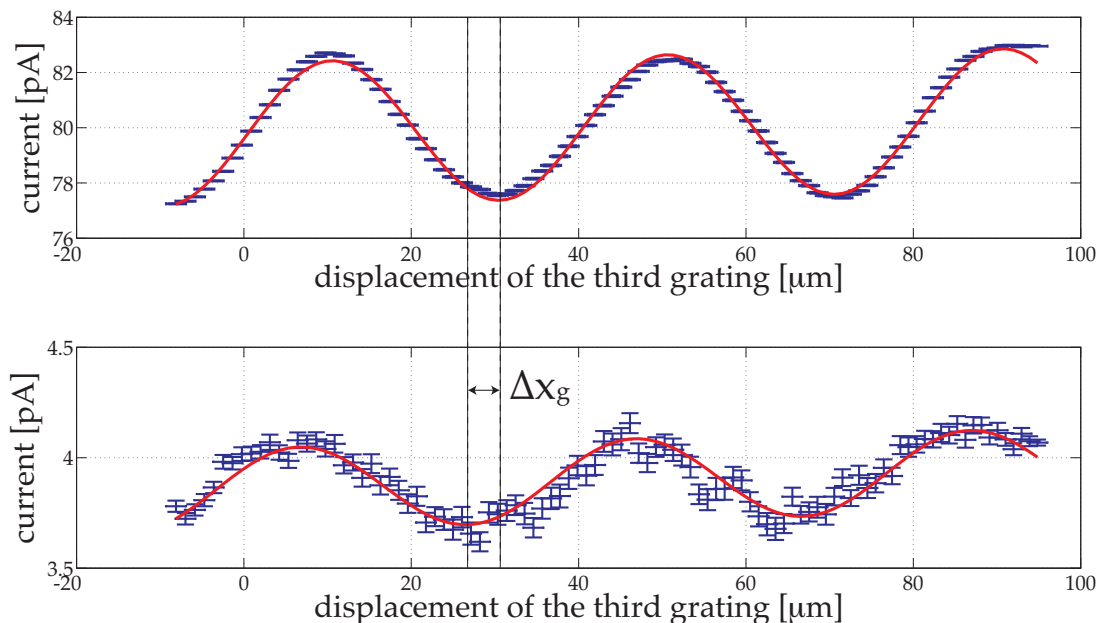

Figure 5.12: First runs of the three-grating setup using the argon source in Heidelberg. The upper plot shows the signal that the photons and the lower plot corresponds to the same data, where only the signal of the atoms is plotted.

Discussion of the Error on g

The error on the absolute g-measurement via equation 5.22 is given by

$$\frac{\triangle g}{g} = \sqrt{\left(\frac{\triangle(\triangle x_g)}{\triangle x_g}\right)^2 + 4\left(\frac{\triangle \overline{v}_z}{\overline{v}_z}\right)^2 + 4\left(\frac{\triangle L}{L}\right)^2}. \tag{5.24}$$

The individual relative errors, that conribute here, are discussed in the following.

The distance L between two gratings $(L = (30.5 \pm 0.1)\,\text{cm})$**:** Currently, the error $\triangle L$ on the distance L is not a limiting factor. Nevertheless, note that increasing this distance will help to decrease the relative error $\frac{\triangle L}{L}$, which is planned in the next runs. Besides this, the decrease of the number of atoms that reach the end of the deflectometer due to the divergence of the beam could be avoided by implementing the collimator

that has been originally in the chamber for former argon experiments.

Currently, we have a relative error of $\frac{\triangle L}{L} = 3.28 \cdot 10^{-3}$, which is almost neglectable with respect to the other error contributions.

The longitudinal mean velocity $\overline{v}_z$ $\left(\overline{v}_z = (478 \pm 47.8)\,\frac{\text{m}}{\text{s}}\right)$**:**   The longitudinal mean velocity is retrieved from a measurement in front of the deflectometer. We find a relative error of $\frac{\triangle \overline{v}_z}{\overline{v}_z} = 0.1$. The correction for longer distances R and small capture regions of the measurements has not yet been verified with experimental data. To avoid a large systematic error, a velocity measurement along the region of the deflectometer would be appropriate.

A temporarily changing velocity distribution can be possible, as from time to time, we observed different modes of operation of our plasma source. The brightness of the plasma changed during the experiments. We found that some of these different modes are directly linked to a changed particle flow. For other mode changes, a change in temperature and thus also in velocity might be possible but has not been measured so far.

An ideal solution of this problem, is already work in progress: We plan an implementation of an optical detection of the atoms' fluorescence light right before and after the deflectometer. This way, the number of atoms together with their velocities can be monitored simultanously and the measurement becomes independent of the source performance by an adequate post-processing of the data.

The vertical shift $\triangle x_g$ $(\triangle x_g = (3.83 \pm 0.30)\,\mu\text{m})$**:**   The error of this vertical shift is governed by the contrast of the pattern. The steeper the slopes of the pattern, the more precise the determination of the phase shift. Following our simulation results in figure 5.9(a), a contrast of up to 0.8 should be observable. However, we measure a contrast of ~ 0.05. Taking the confidence bounds of the fit into account, we find a relative error of $\frac{\triangle(\triangle x_g)}{\triangle x_g} = 0.08$.

Major error sources that lead to such a decrease of contrast are:

- Noise and vibrations, as no isolation techniques have been implemented in this first setup.

- Unknown fraction of charged particles and atoms which are not in the $1s_5$-state with unknown velocity distributions are detected by the Faraday cup.

- Unknown disturbing magnetic and electric fields yielding an unknown loss of contrast.

- For future runs, it is important to note that the scanning of the third grating is done via piezo-controlled stepper motors, that scan with a velocity of $v_{\mathrm{grat}} = 40 \frac{\mu\mathrm{m}}{\mathrm{s}}$. The bandwidth BW of the Faraday cup behind this scanning grating is given by $BW = 5.7\,\mathrm{Hz}$ [56] which provides us a rise time of [100]

$$t_R = \frac{0.35}{BW} \approx 60\,\mathrm{ms}. \qquad (5.25)$$

  Hence, the detection system consisting out of the scanning grating and the rather inert ampère-meter that measures the current of the Faraday cup integrates over a vertical range of

$$x_r = v_{\mathrm{grat}} t_R \approx 2.4\,\mu\mathrm{m}. \qquad (5.26)$$

  This integration might limit the contrast in future runs. In our first runs, a dependence on the scanning velocity v_{grat} has not been observed.

Improving these error sources opens promising prospects towards a high-precision gravimeter for the setup in Heidelberg and towards the successful gravitational measurement of antimatter at CERN.

Chapter 6

Conclusion and Outlook

6.1 Conclusion

In the present thesis, a Moiré-deflectometer has been studied with regard to its application as gravimeter for the antihydrogen experiment of the AE$\overline{g}$IS-project.

For a complete theoretical background of the deflectometer, we distinguished between two major regimes – one governed by wave-propagation and wave-interference and the other one entirely describable by classical ray optics or Newtonian Mechanics. Both these regimes were presented in the context of optical and matterwaves. With this theoretical basis, we optimised the classical Moiré-deflectometer for its application within the AE$\overline{g}$IS-experiment. In order to do this, we discussed its minimal resolvable acceleration $g_{\min}$ with regard to the antihydrogen experiment at CERN, and also considering an appropriate testing setup with metastable argon atoms in Heidelberg. In the latter application, we found that the setup can even approach the precision required to resolve the tidal effect.

In addition, we presented a sensitivity analysis on external magnetic an electric fields and found critical field values for both experimental setups with argon and with antihydrogen. For the magnetic field, we also discussed the application of a constant offset field to reduce the dependence on a disturbing field gradient.

The experimental part of this work covered the design and construction and first gravitational measurements of a Moiré-deflectometer for the AE$\overline{g}$IS-project. In this context, we developed appropriately large-area transmission gratings – the major parts

of the setup – and demonstrated our improvements to the stability of the setup. Building a test-setup with an argon source and a Faraday-cup-detection allowed for an absolute gravitational measurement with our first prototype of the deflectometer. These measurements yielded an absolute value of $g = (9.5 \pm 1.9)\,\frac{\text{m}}{\text{s}^2}$, which clearly demonstrated the functionality and in particular, the potential use of the Moiré-deflectometer as gravimeter for the AE$\overline{\text{g}}$IS-experiment.

One of the main goals of the project has been achieved through the successful measurement of gravitation with the modified design of a classical Moiré-deflectometer. A deeper understanding of both, the setup in general and possible disturbing effects such as external fields or vibrations has been gained. This will now allow for a focused work on improving the apparatus and the final implementing it into the AE$\overline{\text{g}}$IS-experiment at CERN.

6.2 Outlook

Starting with an outlook for the testing experiments in Heidelberg, there are several experimental improvements that can be implemented in the near future. Firstly, mounting Hall-sensors along the deflectometer, will provide us a control of the external magnetic field, which might lead together with the here presented sensitivity analysis to the design and construction of an appropriate magnetic shielding. The presented discussion of the BRGS-method suggests to use a surrounding solenoid for the argon-experiment.

Secondly, after manufacturing three wafers of the grating design that has been developed within the framework of this thesis, the current Moiré-deflectometer can be upgraded to a first prototype with large-area gratings. These gratings also facilitate the implementation of the optical Mach-Zehnder-interferometers to control the setup's stability during data acquisition. In this context, the previously found vibration isolation techniques can also be implemented into the current setup and hence, substantially decrease any noise- and vibration effects.

Furthermore, the large error of the gravitational measurement that originates from the determination of the longitudinal mean velocity, needs to be decreased. As pre-

sented in this thesis, this might be done by an upgrade of the currently implemented source to a supersonic source.

Another even more promising method is to use a velocity-selective detection technique instead of the Faraday cup. Using the light-induced-fluoresence method, similar to the one that has already been used for the source characterisation, we can retrieve the flow of atoms and, simultaneously, their velocity distributions. In this way, the uncertainty of the considered velocity is much smaller and the error on g can be decreased substantially.

Furthermore, this detection method exclusively measures the metastable atoms in the $1s_5$-state and is not sensitive on any other particles originating from the plasma source. Additionally, the fluorenscence detection method allows us to monitor the fluoresence signal of the atoms right before their flight through the deflectometer. Hence, we receive an ideal reference signal, which may become particularly useful when going to larger integration times. For these time scales, the uncontrollable changing of the modes of the plasma source, which we observe from time to time, could be mapped out by normalising the velocity selective measurements at the end of the deflectometer with the fluoresence signal right in front of this gravimeter.

Regarding this large variety of improvements, many of which have already been initiated, we set up a classical Moiré-deflectometer as gravimeter that can potentially resolve the acceleration of the tidal force with $10^{-7}g$.

For the AE$\overline{\text{g}}$IS-setup at CERN, great prospects have been opened with the first measurements in Heidelberg. Not only have we shown the functionality of our design of the Moiré-deflectometer. With the demonstration of a three-grating setup, we have also provided a possible alternative detection method for the antihydrogen experiment using three gratings instead of two. Although the three-grating setup reduces the detected antihydrogen atoms by a factor of one third, this option might solve issues with the spatial resolution of the position-sensitive detector that is currently planned for AE$\overline{\text{g}}$IS.

Considering the overall AE$\overline{\text{g}}$IS-experiment, the design, construction, measurements and discussion of the Moiré-deflectometer, which were presented in this thesis, provide useful

information about the prototype of the gravimeter for the first direct gravitational measurement of antimatter.

Appendix A

Mathematical Description of Thin Material Transmission Gratings

A.1 The Gratings

... in Position Space

For a mathematical expression of a transmission function of a thin material transmission grating it is convenient to exploit its periodicity. Thus, convolving the analytic expression of one period with an appropriate train of δ-functions yields the desired analytic expression of the whole grating's transmission. Figure 2.5 shows a zoom into the center region of such an infinitesimal thin grating. To describe the transmission of one period d, the so-called *top-hat-function* $\Pi(x)$, sketched in figure A.1, is used. This function is defined by[39]

$$A\Pi\left(\frac{x}{a}\right) = \begin{cases} A, & if\,|x| < \frac{a}{2} \\ 0, & \text{otherwise} \end{cases} \tag{A.1}$$

Using this function as it is shown in figure 2.5 requires an additional shift of its absolute position in space. Hence, one period is expressed analytically by

$$f_p(x) = \prod\left(\frac{x + \frac{a}{2}}{a}\right), \tag{A.2}$$
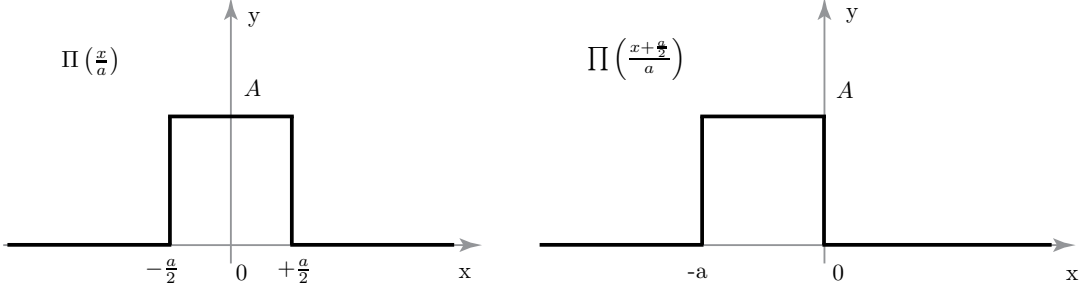
Figure A.1: Usage of a top-hat function.

where the width of one hole is given by a and the maximal transmittance through it is normalised to one, i. e. $A = 1$.

In order to implement the periodicity of the grating with N slits a finite train of δ-functions $\sum_{\text{finite}} \delta\left(x - ld\right)$ of periodicity d only needs to be shifted by $\frac{a}{2}$ as it is done for the top-hat-function before. Thus, the total transmission function of a material grating is given by

$$
f_{\text{grat}}(x) = \underbrace{\sum_{l=\frac{N-1}{2}}^{\frac{N-1}{2}} \delta\left(\left(x + \frac{a}{2}\right) - ld\right)}_{=h(x)} \circledast \underbrace{\prod\left(\frac{x + \frac{a}{2}}{a}\right)}_{=f_p(x)}, \tag{A.3}
$$

where $\circledast$ denotes the convoltion of the two functions $f_p(x)$ and $h(x)$, which is defined as

$$
(f_p \circledast h)(x) = \int_{-\infty}^{\infty} f(\tau)h(x - \tau)d\tau. \tag{A.4}
$$

... in Fourier Space

The Fourier transform of the grating's transmission function can now be found by using the definitions of $h(x)$ and $f_p(x)$ of equation (A.3) and some of the transformation properties given in subsection A.2. Starting with $h(x)$ the properties given in equations (A.9) and A.13 yield

$$
H(u) = e^{\pi iau}\frac{\sin\left(\pi N du\right)}{\sin\left(\pi du\right)}. \tag{A.5}
$$

132

Furthermore, for $f_p(x)$ the properties of equations (A.9) and (A.12) lead to

$$F_p(u) = e^{\pi iau} \cdot a \cdot \text{sinc}\,(au)\,. \tag{A.6}$$

Using the convolution theorem of equation A.14 finally provides the Fourier representation of the transmission function

$$F_{\text{grat}}(u) = e^{2\pi iau} \cdot a \cdot \text{sinc}\,(au)\, \frac{\sin\,(\pi N du)}{\sin\,(\pi du)} \tag{A.7}$$

A.2 The Fourier Transform and Some Useful Properties

The Fourier Transform of a general function $f(x)$ is defined as

$$F(u) = \int_{-\infty}^{\infty} f(x)e^{-2\pi ixu}dx. \tag{A.8}$$

There are some important properties of the Fourier pair $f(x) \overset{FT}{\longleftrightarrow} F(u)$ for the derivation of the grating's transmission function:

1. Shifting property:

$$f(x - x_0) \overset{FT}{\longleftrightarrow} e^{-2\pi ix_0 u}F(u) \tag{A.9}$$

2. Derivatives:

$$-2\pi it f(x) \overset{FT}{\longleftrightarrow} \frac{dF(u)}{du} \qquad \text{and} \tag{A.10}$$

$$\frac{df(x)}{dx} \overset{FT}{\longleftrightarrow} 2\pi iuF(u). \tag{A.11}$$

3. Top-hat-function:

$$f(x) = \prod \left(\frac{x + \frac{a}{2}}{a} \right) \overset{FT}{\longleftrightarrow} F(u) = Aa \cdot \text{sinc}\,(au) \tag{A.12}$$

4. Finite train of $(2n + 1)$ δ-functions:

$$f_n(x) = \sum_{l=-n}^{n} \delta\,(x - ld) \overset{FT}{\longleftrightarrow} F_n(u) = \frac{\sin\left(2\pi\left(n + \frac{1}{2}\right)du\right)}{\sin\,(\pi du)} \tag{A.13}$$

Note the periodicity of $F_n(u)$ with period $\frac{1}{d}$ and its major peaks at any integer multiples of this period with a height of $2n + 1$.

5. *Convolution theorem*

$$g(x) = (f \circledast h)\,(x) \overset{FT}{\longleftrightarrow} G(u) = F(u)H(u) \tag{A.14}$$

The proofs of these properties can be found in the Appendix of [101] and in[39].

A. MATHEMATICAL DESCRIPTION OF THIN MATERIAL TRANSMISSION GRATINGS

Appendix B

Atomic Data

B.1 General and Atomic Constants

Table B.1: Some useful general constants taken from [102].

speed of light c	$299792458 \frac{\text{m}}{\text{s}}$
gravitational constant G	$6.67384(80) \cdot 10^{-11} \, \text{m}^3 \text{kg}^{-1} \text{s}^{-2}$
atomic mass unit amu	$1.660538782(83) \cdot 10^{-27} \, \text{kg}$
electron mass m_e	$9.10938215(45) \cdot 10^{-31} \, \text{kg}$
proton mass m_p	$1.672621777(74) \cdot 10^{-27} \, \text{kg}$
Planck constant h	$6.62606896(33) \cdot 10^{-34} \text{Js}$
Planck constant $\hbar = \frac{h}{2\pi}$	$1.054571726(47) \cdot 10^{-34} \text{Js}$
Boltzmann constant k_B	$1.3806504(24) \cdot 10^{-23} \text{JK}^{-1}$
magnetic permeability μ_0	$12.566370614 \cdot 10^{-7} \text{NA}^{-2}$
electric permittivity $\varepsilon_0 = \frac{1}{\mu_0 c^2}$	$8.854187817 \cdot 10^{-12} \frac{\text{F}}{\text{m}}$
Bohr radius $a_0 = \frac{4\pi\varepsilon_0 \hbar^2}{m_e e^2}$	$0.52917721092(17) \cdot 10^{-10} \, \text{m}$
Bohr magneton $\mu_B = \frac{e\hbar}{2m_e}$	$927.400915(23) \cdot 10^{-26} \frac{\text{J}}{\text{T}}$
fine structure constant $\alpha = \frac{e^2}{4\pi\varepsilon_0 \hbar c}$	$\frac{1}{137.035999074(44)}$
Rydberg constant $R_\infty = \frac{m_e e^4}{8\varepsilon_0^2 h^3 c}$	$10973731.568539(55) \frac{1}{\text{m}}$

B.2 Atomic Properties of Argon

Table B.2: Some useful atomic properties of ^{40}Ar [102].

relative abundance	0.996
mass m	39.96 amu
nuclear spin I	0
relevant transition	$1s_5 - 2p_9$
Landé factor g_J of the $1s_5(J = 2)$-state	1.506
wavelength λ	811.754 nm
linewidth γ	$2\pi \cdot 5.85$ MHz
lifetime τ	27.09 ns
saturation intensity I_0	$1.44\frac{\text{mW}}{\text{cm}^2}$
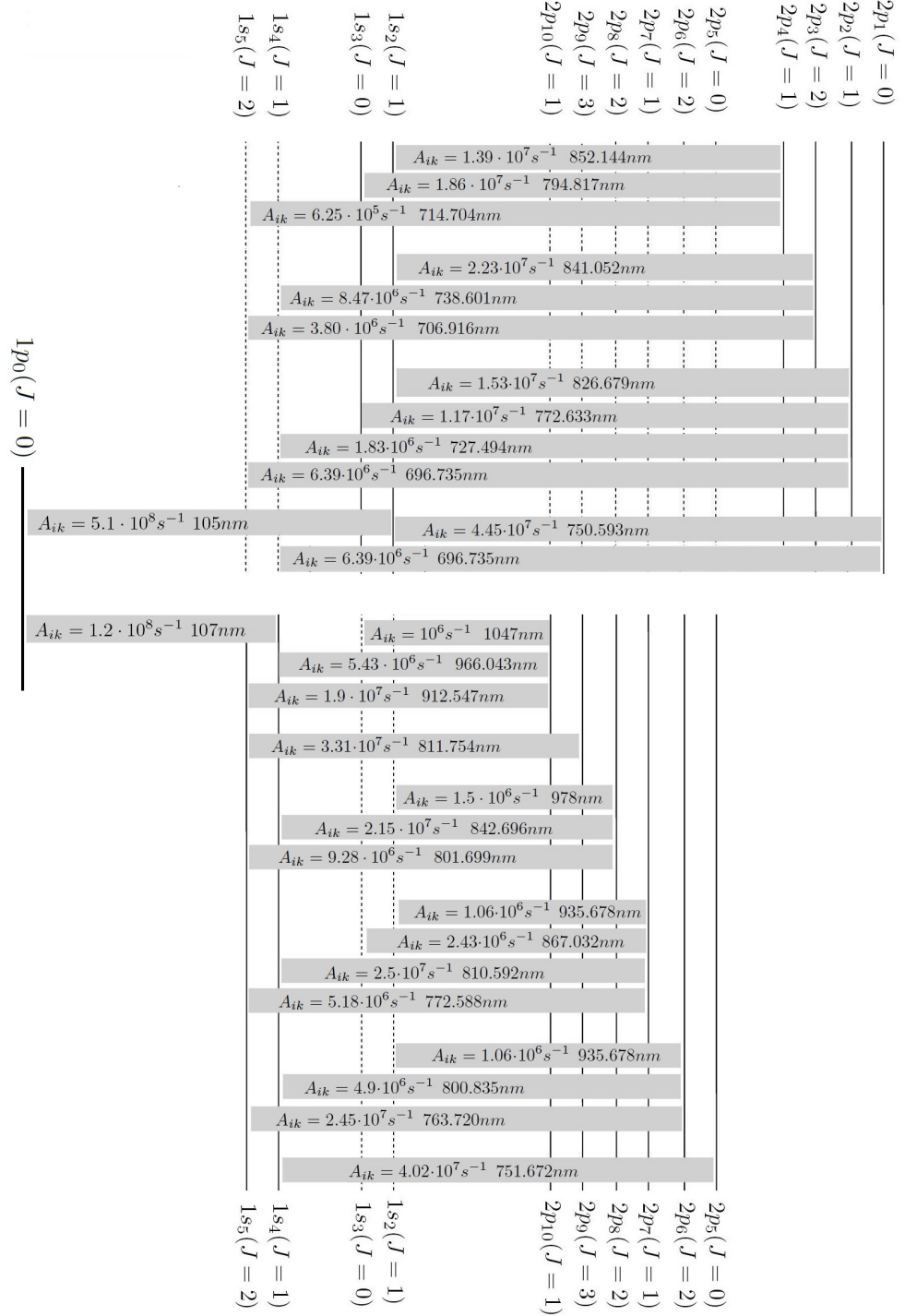
Figure B.1: Atomic Transisions of argon and their properties provided by the Einstein A-coefficient. Data was taken from [102].

Bibliography

[1] P.A.M. Dirac. Quantised singularities in the electromagnetic field. *Proceedings of the Royal Society of London. Series A, Containing Papers of a Mathematical and Physical Character*, 133(821):60–72, 1931. 13

[2] Carl D. Anderson. The positive electron. *Phys. Rev.*, 43:491–494, Mar 1933. 13

[3] Owen Chamberlain, Emilio Segrè, Clyde Wiegand, and Thomas Ypsilantis. Observation of antiprotons. *Phys. Rev.*, 100:947–950, Nov 1955. 13

[4] J. Eades and F. J. Hartmann. Forty years of antiprotons. *Rev. Mod. Phys.*, 71:373–419, Jan 1999. 13

[5] G. Baur, G. Boero, A. Brauksiepe, A. Buzzo, W. Eyrich, R. Geyer, D. Grzonka, J. Hauffe, K. Kilian, M. LoVetere, et al. Production of antihydrogen. *Physics letters B*, 368(3):251–258, 1996. 13

[6] G. Blanford, D. C. Christian, K. Gollwitzer, M. Mandelkern, C. T. Munger, J. Schultz, and G. Zioulas. Observation of atomic antihydrogen. *Phys. Rev. Lett.*, 80:3037–3040, Apr 1998. 13

[7] M. Amoretti, C. Amsler, G. Bonomi, A. Bouchta, P. Bowe, C. Carraro, CL Cesar, M. Charlton, MJT Collier, M. Doser, et al. Production and detection of cold antihydrogen atoms. *Nature*, 419(6906):456–459, 2002. 13, 21

[8] G. Gabrielse, NS Bowden, P. Oxley, A. Speck, CH Storry, JN Tan, M. Wessels, D. Grzonka, W. Oelert, G. Schepers, et al. Driven production of cold antihydrogen and the first measured distribution of antihydrogen states. *Physical review letters*, 89(23):233401, 2002. 13

[9] GB Andresen, MD Ashkezari, M. Baquero-Ruiz, W. Bertsche, P.D. Bowe, E. But-ler, CL Cesar, S. Chapman, M. Charlton, A. Deller, et al. Trapped antihydrogen. *Nature*, 468(7324):673–676, 2010. 13

[10] A Kellerbauer, M Amoretti, A. S Belov, G Bonomi, I Boscolo, R. S Brusa, M Büchner, V. M Byakov, L Cabaret, C Canali, C Carraro, F Castelli, S Cialdi, M de Combarieu, D Comparat, G Consolati, N Djourelov, M Doser, G Drobychev, A Dupasquier, G Ferrari, P Forget, L Formaro, A Gervasini, M. G Giammarchi, S. N Gninenko, G Gribakin, S. D Hogan, M Jacquey, V Lagomarsino, G Manuzio, S Mariazzi, V. A Matveev, J. O Meier, F Merkt, P Nedelec, Markus K Oberthaler, P Pari, M Prevedelli, F Quasso, A Rotondi, D Sillou, S. V Stepanov, H. H Stroke, G Testera, G. M Tino, G Trénec, A Vairo, J Vigué, H Walters, U Warring, S Za-vatarelli, and D. S Zvezhinskij. Proposal for the aegis experiment at the cern antiproton decelerator. 2007. 13, 19, 22

[11] M. Rajner and T. Olszak. Calibration of spring gravimeter using absolute gravity measurements. results of parallel observations using lcr-et and fg5 gravimeters during 2007-2010 in jozefoslaw observatory. *EGU General Assembly 2010, held 2-7 May, 2010 in Vienna, Austria, p. 5919*, 12:5919, 2010. 14

[12] M.W. Gay. Relative gravity measurements using precision pendulum equipment. *Geophysics*, 5(2):176, 1940. 14

[13] U. Bleyer, RW John, and D.E. Liebscher. On a new method of determining the gravitational constant. *Gerlands Beitraege zur Geophysik*, 86:148–152, 1977. 14

[14] Feng Yong-yuan, Zhang Guang-yuan, Li De-xi, Qiu Xiao-mei, Zhou Jing-hua, Gao Jing-Lung, Huang Da-lun, Huang Cheng-qing, and Guo You-Guang. A transportable absolute gravimeter for determining the acceleration due to the earth's gravity. *Metrologia*, 18(3):139–143, 1982. 14, 25

[15] C. Rothleitner and O. Francis. On the influence of the rotation of a corner cube reflector in absolute gravimetry. *Metrologia*, 47:567, 2010. 14, 25

[16] G. Peter, F.J. Klopping, G.S. Sasagawa, J.E. Faller, and T. NIEBAUER. Short-and long-term stability of the jilag-4 absolute gravimeter. *Journal of geophysical research*, 98:4619–4626, 1993. 14, 25

[17] G.S. Sasagawa, F. Klopping, T.M. Niebauer, J.E. Faller, and R.L. Hilt. Intra-comparison tests of the fg5 absolute gravity meters. *Geophysical research letters*, 22(4):461–464, 1995. 14, 25

[18] A. Peters, K.Y. Chung, and S. Chu. High-precision gravity measurements using atom interferometry. *Metrologia*, 38:25, 2001. 14, 25, 44, 47, 51

[19] Achim Peters. *PhD-Thesis*. 14, 25

[20] M. Kasevich and S. Chu. Measurement of the gravitational acceleration of an atom with a light-pulse atom interferometer. *Applied Physics B: Lasers and Optics*, 54:321–332, 1992. 14, 25, 51

[21] W. Phillips, S. Rolston, P. Lett, T. McIlrath, N. Vansteenkiste, and C. West-brook. Laser manipulation and cooling of (anti)hydrogen. *Hyperfine Interactions*, 76:265–272, 1993. 14

[22] M.K. Oberthaler, S. Bernet, E.M. Rasel, J. Schmiedmayer, and A. Zeilinger. Inertial sensing with classical atomic beams. *Physical Review A*, 54(4):3165, 1996. 14, 23, 38, 46, 85

[23] M.M. Nieto and T. Goldman. The arguments against. *Physics Reports*, 205(5):221–281, 1991. 18, 19

[24] DC Peaslee. Nonexistence of gravity shields. *Science (New York, NY)*, 124(3235):1292, 1956. 18

[25] R.P. Feynman. Lectures on gravitation, 1962-63. Lectures Notes by F.B. Morinigo and W.G. Wagner (Caltech, Pasadena). 18

[26] K. Jagannathan and LPS Singh. Attraction/repulsion between like charges and the spin of the classical mediating field. *Physical Review D*, 33(8):2475, 1986. 18

[27] Tony Tothman and Stephen Boughn. Can gravitons be detected? *arXiv.org*, page 5078, May 2000. 18

[28] P. Morrison. Approximate nature of physical symmetries. *American Journal of Physics*, 26:358, 1958. 19

BIBLIOGRAPHY

[29] M. Fischler, J. Lykken, and T. Roberts. Direct observation limits on antimatter gravitation. *Arxiv preprint arXiv:0808.3929*, 2008. 19

[30] RG Greaves and CM Surko. Antimatter plasmas and antihydrogen. *Physics of Plasmas*, 4(5):1528–1543, 1997. 20

[31] A. Kellerbauer, M. Amoretti, AS Belov, G. Bonomi, I. Boscolo, RS Brusa, M. Büchner, VM Byakov, L. Cabaret, C. Canali, et al. Proposed antimatter gravity measurement with an antihydrogen beam. *Nuclear Instruments and Methods in Physics Research Section B: Beam Interactions with Materials and Atoms*, 266(3), 2008. 21

[32] L. Timmen, RH Röder, and M. Schnüll. Absolute gravity determination with jilag-3improved data evaluation and instrumental technics. *Journal of Geodesy*, 67(2):71–80, 1993. 25

[33] HM Guo, HW Liu, YL Wang, HJ Gao, HX Shang, ZW Liu, HM Xie, and FL Dai. Nanometre moiré fringes in scanning tunnelling microscopy of surface lattices. *Nanotechnology*, 15:991, 2004. 28

[34] M.L. Kimber. *Development of a Virtually Calibrated Projection Moiré Interferometry Technique Capable of Inaccessible Surface Measurements*. Brigham Young University. Dept. of Mechanical Engineering, 2004. 28

[35] Z Wu, G Montay, and J Lu. High sensitivity moiré interferometry and incremental hole-drilling method for residual stress measurement. *Comptes Rendus De L Academie Des Sciences Serie Ii Fascicule B-Mecanique*, 329(8):585–593, 2001. 28

[36] I. Glatt and O. Kafri. Moiré deflectometry–ray tracing interferometry. *Optics and lasers in engineering*, 8(3-4):277–320, 1988. 28

[37] B. Han, D. Post, and P. Ifju. Moiré interferometry for engineering mechanics: current practices and future developments. *The Journal of Strain Analysis for Engineering Design*, 36(1):101, 2001. 28

[38] J.M. Cowley. *Diffraction physics*. North Holland, 1995. 29

[39] Sze M. Tan. *Linear System*. Tan, Sze M. 29, 131, 133

[40] B. Brezger, M. Arndt, and A. Zeilinger. Concepts for near-field interferometers with large molecules. *Journal of Optics B: Quantum and Semiclassical Optics*, 5:S82, 2003. 30, 35, 36

[41] Henry Fox Talbot. *http://en.wikipedia.org/wiki/HenryFoxTalbot*. 32

[42] P. Cloetens, JP Guigay, C. De Martino, J. Baruchel, and M. Schlenker. Fractional talbot imaging of phase gratings with hard x rays. *Optics letters*, 22(14):1059–1061, 1997. 32

[43] M.S. Chapman, C.R. Ekstrom, T.D. Hammond, J. Schmiedmayer, B.E. Tannian, S. Wehinger, and D.E. Pritchard. Near-field imaging of atom diffraction gratings: The atomic talbot effect. *Physical Review A*, 51(1):14–17, 1995. 35

[44] JF Clauser and MW Reinsch. New theoretical and experimental results in fresnel optics with applications to matter-wave and x-ray interferometry. *Applied Physics B: Lasers and Optics*, 54(5):380–395, 1992. 35

[45] D.W. Keith, C.R. Ekstrom, Q.A. Turchette, and D.E. Pritchard. An interferometer for atoms. *Physical review letters*, 66(21):2693–2696, 1991. 35

[46] J. Schmiedmayer, CR Ekstrom, MS Chapman, TD Hammond, and DE Pritchard. Fundamentals of quantum optics iii. *Proceedings, Kühtai, Austria, edited by F. Ehlotzky, Lecture Notes in Physics*, 420, 1993. 35

[47] M.S. Chapman, C.R. Ekstrom, T.D. Hammond, R.A. Rubenstein, J. Schmiedmayer, S. Wehinger, and D.E. Pritchard. Optics and Interferometry with Na_2 Molecules. *Physical review letters*, 74(24):4783–4786, 1995. 35

[48] P.R. Berman. *Atom interferometry*. Academic Pr, 1997. 35

[49] D Meschede and Helmut Vogel. *Gerthsen physik; 21. Aufl*. Springer, Berlin, 2002. 44, 45

[50] J.V. Narlikar. *The lighter side of gravity*. Cambridge Univ Pr, 1996. 44

[51] C.J. Foot. *Atomic physics*, volume 7. Oxford University Press, USA, 2005. 57, 66, 68, 76

BIBLIOGRAPHY

[52] C Alwardt. Vorbereitungen zum aufbau einer magneto-optischen atomfalle zur atom trap trace analysis von kryptonisotopen. *znf.uni-hamburg.de.* 58

[53] Ralf Stützle. Nicht zerfließende Wellenpakete in imaginären Potentialen. *PhD-Thesis*, 2006. 58, 59, 112

[54] Ingolf V. Hertel and Claus-Peter Schulz. *Atome, Molekle und optische Physik 1.* Springer, 2008. 58, 60, 68

[55] Franz Schwabl. *Quantenmechanik 1.* Springer, 2007. 60, 68, 76

[56] Hanno Filter. Methoden zur Flussbestimmung von metastabilen Argonatomen. *Diploma-Thesis*, 2011. 61, 113, 115, 119, 120, 121, 125

[57] Wolfgang Demtröder. *Experimentalphysik 3.* Springer, 2005. 67

[58] H. Kopfermann. *Kernmomente.* Atom Interferometry, 1956. 67

[59] private communication with with Rydbergexperts within the frame of Center of Quantumdynamics, Heidelberg. *http://www.physi.uni-heidelberg.de/Forschung/QD/oldhp/research/Rydberg/.* 70, 80

[60] N. Derby and S. Olbert. Cylindrical magnets and ideal solenoids. *American Journal of Physics*, 78:229, 2010. 71, 72, 73

[61] John Ross. *Molecular Beams.* Interscience Publisher, 1966. 76

[62] E. Pollack, E.J. Robinson, and B. Bederson. Determination of the polarizability tensors of the magnetic substates of 3p2 metastable argon. *Phys. Rev*, 134:A1210–A1215, 1964. 77, 78

[63] T.F. Gallagher. *Rydberg atoms*, volume 3. Cambridge Univ Pr, 2005. 79, 80

[64] PHM Bräunig. High-Stability Deflectometer for Antimatter Gravity Measurements. *Diploma-Thesis*, 2010. 84, 86, 102, 104, 105, 106

[65] private communication with collaborators of AEḡIS. *http://aegis.web.cern.ch/aegis/collaboration.html.* 84

[66] C.K. Chung. Geometrical pattern effect on silicon deep etching by an inductively coupled plasma system. *Journal of Micromechanics and Microengineering*, 14:656, 2004. 84

[67] K. Buchholz, A. Tinazli, A. Kleefen, D. Dorfner, D. Pedone, U. Rant, R. Tampé, G. Abstreiter, and M. Tornow. Silicon-on-insulator based nanopore cavity arrays for lipid membrane investigation. *Nanotechnology*, 19:445305, 2008. 84

[68] G.S. Oehrlein and Y.H. Lee. Reactive ion etching related si surface residues and subsurface damage: Their relationship to fundamental etching mechanisms. *Journal of Vacuum Science & Technology A: Vacuum, Surfaces, and Films*, 5(4):1585–1594, 1987. 84

[69] R Wolf and R Helbig. Reactive ion etching of 6H-SiC in SF6/O-2 and CF4/O-2 with N-2 additive for device fabrication. *Journal of the Electrochemical Society*, 143(3):1037–1042, 1996. 84

[70] David R Lide. Crc handbook of chemistry and physics. US Patent Office, June 1999. 87

[71] free trial version. *http://www.gsolver.com/*. 88, 89

[72] David Fluckinger. GSolver V5.2 User's Manual, 2010. 88

[73] MG Moharam and TK Gaylord. Rigorous coupled-wave analysis of planar-grating diffraction. *JOSA*, 71(7):811–818, 1981. 88

[74] Reaktive Ionenätzen. 89

[75] private communication with iX-factory. *http://ix-factory.de/*. 92, 93, 95, 96, 98, 99

[76] J.P. Colinge. *Silicon-on-insulator technology: materials to VLSI*. Kluwer Academic Pub, 2004. 92

[77] J Laconte, Denis Flandre, J P Raskin, and Jean-Pierre Raskin. Soi device and method for its fabrication. (11459316):292, Jul 2006. 92

BIBLIOGRAPHY

[78] D.W. Allan. Statistics of atomic frequency standards. *Proceedings of the IEEE*, 54(2):221–230, 1966. 103

[79] F. Riehle. *Frequency standards*. Wiley-Vch, 2004. 103, 106

[80] C. Audoin and B. Guinot. The measurement of time: time, frequency, and the atomic clock, 2001. 103

[81] F.B. Dunning and R.G. Hulet. *Atomic, molecular, and optical physics: Atoms and molecules*, volume 29. Academic Pr, 1996. 109, 110, 111

[82] Hans Pauly. *Atom, Molecule, and Cluster Beams I: Basic Theory, Production and Detection of Thermal Energy Beams*. Springer series on atomic, optical, and plasma physics. Springer, Berlin, 2000. 109, 110, 111

[83] J A Swansson, K G H Baldwin, M D Hoogerland, A G Truscott, and S J Buckman. A high flux, liquid-helium cooled source of metastable rare gas atoms. *Applied Physics B-Photophysics and Laser Chemistry*, 79(4), Jul 2004. 109, 111

[84] B Viaris de Lesegno, J C Karam, M Boustimi, F Perales, C Mainos, J Reinhardt, J Baudon, V Bocvarski, D Grancharova, F Pereira Dos Santos, T Durt, H Haberland, and J Robert. Stern Gerlach interferometry with metastable argon atoms: an immaterial mask modulating the profile of a supersonic beam. *The European Physical Journal D - Atomic, Molecular and Optical Physics*, 23(1):25–34, Apr 2003. 110, 111

[85] M. Baker. Metastable atom lithography. 2008. 111

[86] Martin Störzer. Realisierung eines langsamen, intensiven Strahls metastabiler Argonatome. *Diploma-Thesis*, 2003. 112

[87] Joachim Welte. Atom trap trace analysis of ^{39}Ar. *PhD-Thesis*, 2011. 113

[88] Florian Ritterbusch. Realization of a collimated beam of metastable atoms for ATTA of Argon 39. *Diploma-Thesis*, 2009. 113

[89] error -function. *http://en.wikipedia.org/wiki/Errorfunction*. 116

[90] Weisstein, Eric W. "Gaussian Function." From MathWorld–A Wolfram Web Resource. *http://mathworld.wolfram.com/GaussianFunction.html*. 116

[91] W. Allison, FB Dunning, and ACH Smith. Secondary electron ejection from metal surfaces by metastable atoms. iii. energy and angular distributions of the ejected electrons. *Journal of Physics B: Atomic and Molecular Physics*, 5:1175, 1972. 119

[92] S. Schohl, D. Klar, T. Kraft, HAJ Meijer, M.W. Ruf, U. Schmitz, SJ Smith, and H. Hotop. Absolute detection of metastable rare gas atoms by a cw laser photoionization method. *Zeitschrift für Physik D Atoms, Molecules and Clusters*, 21(1):25–39, 1991. 119, 120

[93] M. Hartl. Ein planarer de broglie-wellenleiter. *PhD-Thesis*, 2000. 119

[94] FB Dunning, ACH Smith, and RF Stebbings. Secondary electron ejection from metal surfaces by metastable atoms. i. measurement of secondary emission coefficients using a crossed beam method. *Journal of Physics B: Atomic and Molecular Physics*, 4:1683, 1971. 120

[95] FB Dunning and ACH Smith. Secondary electron ejection from metal surfaces by metastable atoms. ii. measurements of secondary emission coefficients using a gas cell method. *Journal of Physics B: Atomic and Molecular Physics*, 4:1696, 1971. 120

[96] H. Hirata, M. Tadokoro, N. Nakano, Z.L. Petrovic, and T. Makabe. Two-dimensional images of radiative and metastable excited state radial profiles for an inductively coupled plasma in argon. *Plasma Science, IEEE Transactions on*, 27(1):50–51, 1999. 121

[97] G.A. Hebner and P.A. Miller. Behavior of excited argon atoms in inductively driven plasmas. *Journal of Applied Physics*, 87:8304, 2000. 121

[98] GA Hebner. Spatially resolved, excited state densities and neutral and ion temperatures in inductively coupled argon plasmas. *Journal of applied physics*, 80(5):2624–2636, 1996. 121

BIBLIOGRAPHY

[99] D. Leonhardt, CR Eddy Jr, VA Shamamian, RF Fernsler, and JE Butler. Argon metastables in a high density processing plasma. *Journal of applied physics*, 83:2971, 1998. 121

[100] Keithley. 6th edition keithley's low level measurements handbook, 2004. 125

[101] F. Haupert. Diffraction of a bose-einstein condensate and the path to an atom laser. *MSc-Thesis*, 2007. 133

[102] NIST. NIST Atomic Spectra Database. Technical report, NIST, 2010. 135, 136, 137

Acknowledgements

First of all, I would like to thank my supervisor Markus Oberthaler for providing me with the opportunity to contribute to the exciting AE$\overline{g}$IS-experiment. It has been his trust in my work, without which this thesis would not have been possible. In particular, his catching enthusiasm and our fruitful discussions have always been a great help and source of motivation througout my time with the 'matterwavers'. Besides this, I highly appreciate his outstanding support in hard times.

I further thank Michael Doser, not only for being the second referee of this thesis, he also kept me up-to-date on the news and happenings at CERN throughout my project. The discussions with him during the collaboration meetings were very valuable for my work in Heidelberg. These collaboration meetings in particular have always been a great source of inspiration and motivation. Thus, special thanks go to the entire collaboration not only for their fantastic work, but also for their enthusiastic meetings.

In addition to this, I want to thank the *International Max-Planck-Research school - QD* in Heidelberg for supporting my project financially and also for the opportunities as their first student representative. It has been a privilege and sustainable gainful time for me.

Many thanks go to Dr. Agnes Speck. During the most challenging time of my PhD-project, her office has been an indispensable drop-in centre for me. Besides the financial support, her reflective way of thinking has been an exceptional standby.

> *Nicht da ist man daheim,*
> *wo man seinen Wohnsitz hat,*
> *sondern wo man verstanden wird.*
>
> Christian Morgenstern (1871-1914)

BIBLIOGRAPHY

Declaration

I hereby confirm that I wrote this thesis on my own and that I did not use other sources or means than stated.

Heidelberg, the

(signature)